

8-1-2022

Towards High-Efficient Broadband Omnidirectional Light-Trapping: Discrepancy-Assisted 2D/3D Deterministic Quasi-Random Nanostructure Design, Optimization, and Fabrication

Yihong Zhao

Follow this and additional works at: <https://digitalscholarship.unlv.edu/thesesdissertations>



Part of the [Mechanical Engineering Commons](#)

Repository Citation

Zhao, Yihong, "Towards High-Efficient Broadband Omnidirectional Light-Trapping: Discrepancy-Assisted 2D/3D Deterministic Quasi-Random Nanostructure Design, Optimization, and Fabrication" (2022). *UNLV Theses, Dissertations, Professional Papers, and Capstones*. 4546.
<http://dx.doi.org/10.34917/33690325>

This Dissertation is protected by copyright and/or related rights. It has been brought to you by Digital Scholarship@UNLV with permission from the rights-holder(s). You are free to use this Dissertation in any way that is permitted by the copyright and related rights legislation that applies to your use. For other uses you need to obtain permission from the rights-holder(s) directly, unless additional rights are indicated by a Creative Commons license in the record and/or on the work itself.

This Dissertation has been accepted for inclusion in UNLV Theses, Dissertations, Professional Papers, and Capstones by an authorized administrator of Digital Scholarship@UNLV. For more information, please contact digitalscholarship@unlv.edu.

TOWARDS HIGH-EFFICIENT BROADBAND OMNIDIRECTIONAL LIGHT-TRAPPING:
DISCREPANCY-ASSISTED 2D/3D DETERMINISTIC QUASI-RANDOM
NANOSTRUCTURE DESIGN, OPTIMIZATION, AND FABRICATION

By

Yihong Zhao

Bachelor of Material Science & Engineering
Zhengzhou University
2013

Master of Material Engineering
Boston University
2015

A dissertation submitted in partial fulfillment
of the requirements for the

Doctor of Philosophy – Mechanical Engineering

Department of Mechanical Engineering
Howard R. Hughes College of Engineering
The Graduate College

University of Nevada, Las Vegas
August 2022



Dissertation Approval

The Graduate College
The University of Nevada, Las Vegas

July 15, 2022

This dissertation prepared by

Yihong Zhao

entitled

Towards High-Efficient Broadband Omnidirectional Light-Trapping:
Discrepancy-Assisted 2D/3D Deterministic Quasi-Random Nanostructure Design,
Optimization, and Fabrication

is approved in partial fulfillment of the requirements for the degree of

Doctor of Philosophy – Mechanical Engineering
Department of Mechanical Engineering

Hui Zhao, Ph.D.
Examination Committee Chair

Alyssa Crittenden, Ph.D.
*Vice Provost for Graduate Education &
Dean of the Graduate College*

Shengjie Zhai, Ph.D.
Examination Committee Member

Kwang Kim, Ph.D.
Examination Committee Member

Shubhra Bansal, Ph.D.
Examination Committee Member

Yingtao Jiang, Ph.D.
Graduate College Faculty Representative

ABSTRACT

Recently, nano-scaled surface decoration has brought significant advancement and exciting new possibilities to light management. Numerous nanostructure patterns have been explored, wherein the quasi-random nanostructures (QRNs) present a promising path in manipulating light to increase the photon flux over the broadband spectra for optical (e.g., photovoltaic) devices. However, due to the infinite number of QRNs, it is difficult to directly design and fabricate the exact QRN pattern as desired to achieve the optimized light-trapping capability. To overcome this obstacle, we 1) digitize the traditional continuous QRNs into meshes and then map the meshes to binary matrices, which can be deterministically programmable; and 2) introduce the “star discrepancy” to evaluate the QRNs’ degree of the randomness, which can guide the design and further optimization of QRNs to improve the light-trapping capabilities.

In this dissertation, two-dimensional (2D) QRNs are generated by filling the matrices with deterministic one-dimensional (1D) binary sequences (i.e., Fibonacci, Rudin-Shapiro, Thue-Morse) in a spiral way or direct binary plots (i.e., Halton (2,3)). Additionally, different heights can be assigned quasi-randomly to the 2D quasi-random pattern to generate a three-dimensional (3D) QRN. Compared to the bare solar cells, the efficiency improvement of the solar cell device with our 2D Fibonacci quasi-random nanostructures arranged in an Archimedean spiral is up to 8.31%. Meanwhile, the reflectance on the surface is tremendously reduced by 11.62% at 800 nm. The results show that either the spiral arrangement of nanostructure or QRNs play the key role in the light-trapping scheme. Besides this, we found that in almost the entire visible light spectrum, a higher degree of the surface randomness (i.e., star discrepancy) indicates a higher antireflection capability. A novel “star discrepancy” calculation is consequently employed in this dissertation to assess the degree of surface randomness (2D) or spatial randomness (3D). Based on the star

discrepancy calculation, the optical and electrical performance of the different 2D quasi-random nanostructures can be assessed and optimized without conducting any experiments. Thus, by changing the star discrepancy (i.e., the degree of surface randomness for 2D nanostructure) of RS QRNs, the RS QRNs can be optimized. The two optimized QRNs with drastically increased star discrepancy gradually reduce the surface reflection by up to 25% decrement in the strong reflectance region (~ 500 nm). Moreover, we found that the 3D QRN design outperforms the 2D QRN design for a nanostructured semiconductor layer of a solar cell by taking the randomized heights into consideration. These different types of 3D QRNs possess a higher degree of spatial randomness by assigning the randomized heights to the nanostructures, which leads to a highest J_{sc} enhancement of up to 22% compared to slab cell. Furthermore, the 3D QRNs resulted in an omnidirectional and broadband reduction in optical reflectivity. Hence, the integration of the QRN design and star discrepancy evaluation can be employed to various applications, ranging from external anti-reflective coatings to internal broadband light-trapping structures for the semiconductor layers inside optoelectronic devices. We expect that this systematic methodology could be readily applicable to other nanostructures across all length scales, whose performance largely depends on the surface randomness (2D) or even spatial structural distribution (3D).

ACKNOWLEDGEMENTS

I would like to acknowledge and express my sincere gratitude to my research advisor, Dr. Hui Zhao, for his consistent guidance, encouragement, and immense knowledge throughout my Ph.D. studies and research. His support and enthusiasm carried me through all the stages of research and writing of this dissertation. His profound and comprehensive knowledge has always impressed and motivated me. He encouraged me to never be afraid of challenging authoritative theories or conventional wisdom. His passion and advising style has greatly benefited my Ph.D. life. These are essential components for my success in my projects.

Besides my advisor, I would like to thank Dr. Shengjie Zhai, who literally served as my co-advisor and supported me during my Ph.D. studies. Working with him is usually a lot of pleasure because of his charm. It reminds me of so many late nights we discussed about my projects, and none of us felt tired. Those disputes in the academic field keep me motivated to share feedback, to brainstorm, to promote some ideas. In addition, I am very appreciative of Dr. Shengjie Zhai's assistance in my daily life.

Thanks to Dr. Ming Zhu for his valuable advice and help with the computational method, technical writing, and data analysis.

Specifically, I want to express my gratitude to Dr. Yingtao Jiang, Dr. Shubhra Bansal, and Dr. Kwang Kim for being my committee members. Without your suggestions, I will not be able to finish this dissertation.

Many thanks and appreciation also go to my colleagues in developing the project and those people who are willing to help me out with their genius ideas.

I also appreciate the scholarship and fellowships from UNLV, GPSA, and the Department of Mechanical Engineering.

Finally, and most importantly, I am genuinely grateful to my mom, Naixian Li, and dad, Feng Zhao, for their unwavering love, understanding, and never-ending support. It has been their patience and emotional support which encouraged me to overcome all obstacles.

TABLE OF CONTENTS

ABSTRACT	iii
ACKNOWLEDGEMENTS	v
LIST OF TABLES	xii
LIST OF FIGURES	xiii
LIST OF NOMENCLATURE	xviii
1 CHAPTER ONE: INTRODUCTION	1
1.1 Solar Energy.....	1
1.2 Photovoltaic Effect.....	3
1.3 Theoretical Shockley-Queisser Efficiency Limits	5
1.4 Light-trapping Properties	8
1.5 Nanostructure-based Technology.....	13
1.6 Objective of the Dissertation.....	15
1.7 Organization of the Dissertation	16
2 CHAPTER TWO: FUNDENMENTALS OF SOLAR CELLS AND OPTICAL CHARACTERISTICS	18
2.1 Working Principles of a Semiconductor	18
2.2 Characterization of the Solar Devices (Overview)	19
2.3 I-V Curve, Short Circuit Current and Open Circuit Voltage	21
2.4 Fill Factor, Maximum Power, and Power Conversion Efficiency	24
2.5 Quantum Efficiency	26

2.6	Reflection	28
2.7	Optical Losses and Anti-reflectivity	31
3	CHAPTER THREE: NUMERICAL METHOD FOR SOLAR CELLS.....	33
3.1	Overview of Finite-Difference Time Domain (FDTD).....	33
3.2	Solver Physics	33
3.3	Light Source	35
3.4	Boundary Conditions (BC).....	36
3.5	Reflectance and Transmittance Flux Spectra	37
4	CHAPTER FOUR: A BIOINSPIRED HYBRID LIGHT-TRAPPING STRUCTURE AND ITS FABRICATION FOR THIN-FILM SOLAR CELLS.....	39
4.1	Introduction	39
4.2	Method	41
4.2.1	1D Fibonacci binary sequence design.....	41
4.2.2	Converting 1D binary sequences to virtualized 2D nanostructure patterns.....	43
4.2.3	Transferring designed 2D QRN pattern using an optical driver	44
4.2.4	HLTSC mold fabrication using optical disc technology.....	45
4.3	Results and Discussion.....	48
4.4	Conclusions	52
5	CHAPTER FIVE: 2D DISCREPANCY-ASSISTED DETERMINISTIC QUASI- RANDOM NANOSTRUCTURE DESIGN AND OPTIMIZATION.....	53

5.1	Introduction	53
5.2	Method	57
5.2.1	Binary quasi-random sequences generation.....	57
5.2.2	Different 2D QRP design.....	59
5.3	Theory	61
5.3.1	Discrepancy-assisted QRP design reaching desired surface randomness.....	61
5.3.2	The relationship between the discrepancy and optical performance for QRPs	65
5.4	Results and Discussion.....	67
5.4.1	The relationship between the discrepancy and optical performance for QRPs	67
5.4.2	The comparison of fabricated QRNs and simulated QRNs and its schematic fabrication process	70
5.4.3	Effect of the different surface randomness for photocurrent generation	71
5.4.4	Broad practicability and adaptability of our QRNs for all generation solar cells...	75
5.4.5	Optimization of QRNs based on star discrepancy-assisted patching method.....	76
5.4.6	Mechanical stability for flexibility and bendability of the thin-film solar cells	79
5.5	Conclusion.....	82
6	CHAPTER SIX: ENHANCED BROADBAND OMNIDIRECTIONAL ABSORBER UTILIZING 2D/3D DETERMINISTIC QRNS FOR THIN-FILM SOLAR CELLS.....	84
6.1	Introduction	84
6.2	3D Nanostructured Cell Design and Method	87

6.2.1	3D nanostructure design overview based on its spatial distribution.....	87
6.2.2	Surface morphology (<i>x-y</i> plane) design using programable binary data	87
6.2.3	Randomized heights design of QRNs with quasi-random distribution along the <i>z</i> - direction	88
6.2.4	Converting 2D nanostructure pattern to 3D nanostructure patterns by assigning randomized height scale.....	89
6.3	Theory	91
6.3.1	Spatial distribution evaluation based on discrepancy calculation.....	91
6.3.2	Relationship of the degrees of 2D surface randomness and the degrees of 3D spatial distribution	92
6.4	Discussion and Conclusions.....	93
6.4.1	The reflectance and absorption analysis based on numerical results.....	93
6.4.2	Simulated I-V characteristic	96
6.4.3	Angular wavelength-dependent for Si-based solar cell with 2D/3D QRNs	97
6.5	Conclusions	99
7	CHAPTER SEVEN: CONCLUSIONS AND FUTURE WORK.....	100
7.1	Conclusions	100
7.2	Future Work	103
7.2.1	Achieving a higher degree of the spatial randomness for QRNs.....	103
8	REFERENCES.....	106

9 CURRICULUM VITAE..... 118

LIST OF TABLES

<i>Table 1 The specification of different optical storage disc formats.....</i>	<i>44</i>
<i>Table 2 The star discrepancy calculation of the different quasi-random patterns based on the area R^2....</i>	<i>62</i>
<i>Table 3 Solar cell performance. I_{sc}, V_{oc} and corresponding enhancement of a-Si:H thin-film solar devices.....</i>	<i>70</i>
<i>Table 4 Eight specific height scales related to the sub-intervals (3 bits)</i>	<i>85</i>

LIST OF FIGURES

Fig. 1.1-1 (a) The world primary energy consumption; (b) the wavelength-dependent spectral irradiance.....	2
Fig. 1.2-1 Various generations of PV: 1st wafer-based; 2nd conventional thin-film; 3rd emerging thin-film.	4
Fig. 1.3-1 The Shockley-Queisser limit for the maximum efficiency generated by a solar cell (output) and the inevitable loss (the rest part).	6
Fig. 1.4-1 Schematic illustration of the optical effect for light-trapping schemes, (a) a semiconductor without any light-trapping scheme; (b) a semiconductor with a back reflector; (c) a semiconductor with a nanostructured ARC and a back reflector; (d) a semiconductor with a nanostructured ARC and a nanostructured back reflector.	10
Fig. 1.4-2 The reflectivity of the Si-based solar cell with/without an ARC with the optimal thickness and ITO glasses.....	12
Fig. 1.5-1 The examples of multidimensional nanostructures listed as: (1) 0D; (2) 1D; (3) 2D; (4) 3D.....	14
Fig. 2.1-1 Energy band in materials, (a) insulator; (b) semiconductor; (c) conductor.	19
Fig. 2.2-1 Working principle of a solar cell with a p-n junction.	20
Fig. 2.3-1 The effect of light on the current-voltage characteristics of a p-n junction, (a) the electrical characteristics without illumination (working as a large diode); (b) the shifted I-V curve with low incoming light intensity; (c) a standard I-V curve with normal illumination.....	22
Fig. 2.4-1 A standard I-V curve of a solar cell (red line) with identified I_{sc} and V_{oc} , and its output power.....	26
Fig. 2.5-1 The external quantum efficiency with wavelength of a crystalline silicon solar cell.	28

Fig. 2.6-1 Light propagating at a single plane interacts with the interface.....	29
Fig. 3.2-1 The Yee Cell: a plot of the discretized field: E_x , E_y , H_z , H_x , H_y , E_z	35
Fig. 4.2-1 (a) A spiral curve in a sunflower; (b) the schematic of a binary Fibonacci sequence mapped into writable disc; (c) the SEM image of the Fib QRN inside an optical disc; (d) the Fourier Transform based on the SEM image of the Fib QRN.....	42
Fig. 4.2-2 (a) Layer structure of an optical disc; (b) schematics of the optical disc structure with different lasers for different optical discs (CD, DVD, HD DVD, and Blu-ray).....	44
Fig. 4.2-3 Schematics of thin-film solar devices fabrication with HLTSC and its final device configuration.....	48
Fig. 4.3-1 Simulated reflectance of the thin-film solar cell with/without HLTSC and ASA Only as comparison; (b) Spatial frequency related Power spectral density of the 2D Fibo QRNs.	50
Fig. 4.3-2 (a) The I-V curves of a thin-film solar cell with HLTSC, ASA Only and without any coatings; (b) the angular dependence of a normalized photocurrent with HLTSC, ASA Only and without any coatings.	51
Fig. 5.1-1 (a) the schematic of a writable disc and its recording layer; (b) a generated edge blurred QRP design based on binary RS sequence with MATLAB; (c) a simulated QRN image on Lumerical FDTD software; (d) the SEM image of the fabricated QRNs derived from the optical recording layer; (e) illustration of a 2D QRP generated by binary RS sequence.	56
Fig. 5.2-1 Two-dimensional Halton sequences generated from combination of primes from dimension 2 to dimension 13; the red part is formed by 1D standard Halton sequence, and the green part is formed by optimized sequence.....	60
Fig. 5.3-1 (a) simulated quasi-random structures with low discrepancy value (more uniform); b) simulated pseudo-random structures with high discrepancy value (more random).	64

Fig. 5.3-2 (a) The relationship between star discrepancy and pattern scale on different QRPs (i.e., RS, TM, Fibo, Halton (2,3)); (b) The tendency of the star discrepancy with increased unit square based on the pseudo-random pattern; (c) The tendency of the star discrepancy with increased unit square based on 1D Halton (2,3) sequence. 66

Fig. 5.4-1 The reflectance of a thin-film solar cell (Si-based) with different QRN coatings by Lumerical FDTD simulations. 68

Fig. 5.4-2 Fast Fourier transform from 30 unit* 30 unit to 300 unit* 300-unit (a) Fibonacci; (b) Thue-Morse; (c) Rudin-Shapiro; (d) Halton (2,3) with 0.5 filling ratio. 69

Fig. 5.4-3 (a)-(d) Different quasi-random patterns and their Fourier Transform Analysis; (a) Fibonacci sequence; (b) Thue-Morse sequence; (c) Rudin-Shapiro sequence; (d) Halton (2,3) sequence. (e)-(h) Comparison of spectral power density functions for representing quasi-random structures. 70

Fig. 5.4-4 (a) Schematics of thin-film CIGS fabrication and final device configuration; (b)-(e) SEM and simulated image of the Fibo quasi-random nanostructures and their Fourier Transform Analysis; (f)-(i) SEM and simulated image of the RS quasi-random nanostructures and their Fourier Transform Analysis. 72

Fig. 5.4-5 (a) Schematic illustration of light behavior for solar device with/without nanostructured coating; (b) the relationship between height position and material refractive index; (c) the I-V curve of a thin-film solar cell (a-Si:H) with the different nanostructured coatings (RS, TM, Fibo) and without (solid black line) any coatings; (d) the angular dependence of a normalized photocurrent with/without the nanostructured coatings. 73

Fig. 5.4-6 (a) the I-V curve of a thin-film solar cell (CIGS) with the different nanostructured coatings and without (solid black line) any coatings; (b) the I-V curve of a photodiode device with

the and without (solid black line) any coatings. (c) the omnidirectional distributions of a CIGS thin-film solar cell with different nanostructured coatings; (d) the omnidirectional distribution of a photodiode device with different nanostructured coatings. 76

Fig. 5.4-7 Optimization of QRNs’ star discrepancy and reflectance for broadband light trapping.

(a) Optimization history of RS QRNs’ star discrepancy with 50 iteration times. (b) Simulated reflectance spectrum of the QRNs’ structures, before and after optimization over the wavelength range from 400 nm to 900 nm..... 79

Fig. 5.4-8 (a) The PCE improvement of the different bending angles applied on the thin-film solar devices with our nanostructured coatings; (b) the schematic of the experiment process and its bending angle calculation; (c) the I-V curve with different bending times; (d) the illustration of the flexibility of the thin-film solar cell..... 81

Fig. 6.2-1 An illustration of a 3D QRN design assigned by randomized heights, and 8 heights are quasi-randomly distributed. 90

Fig. 6.3-1 The comparison of 2D and 3D QRNs based on their star discrepancy..... 93

Fig. 6.4-1 (a) The reflectance of a thin-film solar cell (Si-based) with different 2D and 3D quasi-random nanostructured active layers (without any back reflectors). (b)-(g) the filed electric field intensity for different 2D and 3D quasi-random nanostructured Si-based active layer: (b) 3D RS; (c) 3D TM; (d) 3D Fibo; (e) 2D RS; (f) 2D TM; (g) 2D Fibo..... 95

Fig. 6.4-2 The I-V curve of the Si-based solar cell with the different 2D/3D quasi-random nanostructured active layers..... 96

Fig. 6.4-3 The 3D plot of the reflection, AOI, and different types of QRNs with x - y , x - z , and y - z bars of the data plotted inside the cube. 98

Fig. 7.2-1 (a) – (b) Three different diffraction phenomena; (a) third-order diffraction for CD molds, first-order diffraction for DVD molds, and zero-order for Blu-ray molds, respectively. (c) a schematic illustration for stacking method and its FFA result. 105

LIST OF NOMENCLATURE

Abbreviation

2D	Two-dimension
3D	Three-dimension
AM	Air mass
AOI	Angle of incidence
ARC	Anti-reflective coating
ASA	Archimedean Spiral Only
BCs	Boundary conditions
BFAST	Broadband Fixed Angle Source
CdTe	Cadmium telluride
CIGS	Copper indium gallium selenide
c-Si	Crystalline silicon
EQE	External quantum efficiency
FDTD	Finite-Difference Time Domain
FT	Fourier Transform
FTA	Fourier Transform Analysis
FF	Fill factor

Fibo	Fibonacci
GaAs	Gallium arsenide
HALE	High-altitude long-endurance
HLTSC	Hybrid Light-trapping Structure/Coating
IQE	Internal quantum efficiency
OPV	Organic photovoltaic
PCE	Power conversion efficiency
QD	Quantum dot
QE	Quantum efficiency
QRNs	Quasi-random nanostructures
QRP	Quasi-random pattern
PDMS	Polydimethylsiloxane
PML	Perfectly matched layer
PV	Photovoltaic
RS	Rudin-Shapiro
Si	Silicon
SDF	Spectral Density Function
T	Transmission

TE Transverse electric

TM Transverse magnetic

TM Thue-Morse

General terms

D Displacement field

d Thickness of material [m]

D_N Discrepancy value

D_N^* Star discrepancy

E Electrical field

E_i Incidence/light source

E_g Photon energy

E_{ph} Energy of one photon

E_r Reflected wave

E_t Transmitted wave

E_{total} Total power of photons

H Magnetic field

h Plank's constant [$J \cdot Hz^{-1}$]

h_{max} Bent cell's maximum height [cm]

I_{sc}	Short-circuit current [A/mA]
I_L	Light generated current [A]
J_{sc}	Short-circuit current [A/m ²]
k_0	Wave vector
L	Optical path length
L_s	Shortened distance in step function [cm]
$L_{solar\ cell}$	Solar cell length [cm]
n	Refractive index of material
λ	Wavelength of light [nm]
P_{in}	Input power [w]
P_{out}	Output power [w]
P_{max}	Maximum power [w]
R	Track radii [cm]
r_p	Reflection coefficient
V	Writing speed velocity [m/s]
V_{bi}	Build-in electric potential [v]
V_d	Voltage of a diode [v]
V_{oc}	Open-circuit voltage [v]

V_t	Thermal voltage [$^{\circ}\text{C}$]
θ	Refracted angle [$^{\circ}$]
θ_i	Incident angle [$^{\circ}$]
θ_r	Reflected angle [$^{\circ}$]
θ_{stack}	Stacked angle between two QRP [$^{\circ}$]
θ_t	Refracted angle [$^{\circ}$]
α	Wavelength-dependent absorption coefficient

Constants

c	Speed of light [3×10^8 m/s]
k	Boltzmann constant [1.38×10^{-23} J/K]
q	Magnitude of the electronic charge [1.6×10^{-19} C]
μ_0	Vacuum permeability [$1.25663706212(19) \times 10^{-6}$ H/m]

1 CHAPTER ONE: INTRODUCTION

1.1 Solar Energy

To date, the annual global energy needs have increased to around 500 million terajoules, and they are projected to continue to grow in the foreseeable future¹. Among these, 83% of energy comes from fossil fuels, such as gas, oil, and coal; thus, the greenhouse gas emissions (i.e., CO₂) are artificially produced and continue to contribute to climate change (e.g., global temperature, sea levels, and weather patterns). Additionally, it is anticipated that the ratio between the energy demand and the supply of exhaustible energy will gradually decrease after 2030 due to the limited resource storage, while renewable energy is expected to overtake the exhaustible energy by 2050, as illustrated in **Fig 1.1-1 (a)**². As an alternative to conventional and polluting fossil fuels, solar energy is a kind of renewable energy generated directly by the sun, creating tremendous heat and electromagnetic radiation. Such renewable energy resources can contribute to a carbon-free economy in the future. Furthermore, solar energy is seen as the primary alternative with the ability to meet a greater portion of the future energy demand compared with other renewable energy sources. It is due to the large amount of energy that the Earth receives from the sun ($\sim 2 \times 10^{17} \text{ Js}^{-1}$), which can power the planet almost 7000 times³.

When the sunlight travels through the atmosphere, the airborne particles, water molecules, and other gases existing in the air will scatter and absorb the sunlight at specific wavelengths of the sunlight, leading to the solar irradiance change at the Earth's surface. Based on the different irradiation situations during the various time zones of a day or the seasons passing of a year, the air mass coefficient (abbreviated AM) is commonly used to characterize the solar irradiance spectrum. The average solar intensity outside the Earth's atmosphere is $1367 \text{ W} \cdot \text{m}^{-2}$, known as the

“solar constant”, which gives us AM 0 as extraterrestrial radiation⁴. Based on the industry standards and terrestrial radiation, most solar devices are usually tested under AM 1.5 G (i.e., 1000 W·m⁻² for light intensity). **Fig. 1.1-1 (b)** depicts the spectral irradiance at AM 0 and AM 1.5 G vs. the ultraviolet, visible, and infrared wavelength ranges⁵. Depending on the theory of energy distribution, a photon has no mass but has an amount of energy related to a wavelength, denoted by λ , and equivalent energy, denoted by E_g ⁶:

$$E_g = \frac{hc}{\lambda} \quad (1)$$

where h is Plank’s constant, and c is the speed of light.

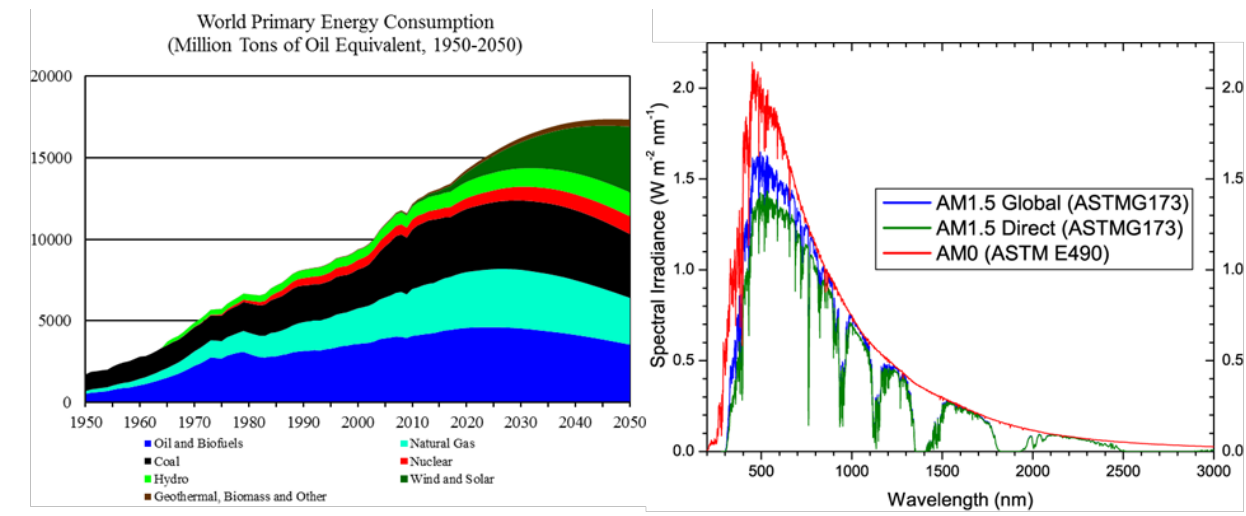


Fig. 1.1-1 (a) The world primary energy consumption; (b) the wavelength-dependent spectral irradiance.

1.2 Photovoltaic Effect

French physicist Edmond Becquerel initially described the photovoltaic (PV) phenomenon in 1839, and it was subsequently developed by Chapin *et al.* using silicon (Si) crystals for working solid-state solar cell devices in 1954^{7,8}. The realization of the PV technology provides a way for us to utilize solar energy by directly converting the sunlight to the electricity instead of utilizing solar thermal electricity generation technique. The basis of the PV effect is that when a semiconductor is exposed to the sunlight, the electron-hole pairs will be generated by absorbing the photons from the sun. The electric current is observed during the electrons' and holes' movement⁹. Since then, scientists have made massive efforts to investigate and develop optoelectronic technologies based on the PV effect. Solar cells are considered as a basic embodiment of photovoltaic systems, which can directly produce direct current output under standard illumination conditions. Since the solar cells were commercially available in 1956, they have been improved toward reducing their fabrication and installation costs for these systems to be deployed on a greater scale¹⁰. Currently, the current PV technologies have been classified into two categories, wafer-based PV (also known as 1st generation PV) and thin-film PV. Later, the thin-film PV is developed into two groups: conventional thin-film (2nd generation PV) and emerging thin-film (3rd generation PV)¹¹⁻¹³. **Fig. 1.2-1** shows an overview of the PV technology and its different types of the PVs. Among the wafer-based PVs, the traditional crystalline silicon cells (c-Si) and gallium arsenide cells (GaAs) dominate the current PV market (~90%)¹⁴. The thin-film cells outperform the wafer-based PVs on absorptance of the active layer, which is almost 10~100 times more efficient than silicon-based (Si-based) and enables the cells to keep the “optical thickness” constant when reducing the physical thickness. However, the market share for thin-film cells is low (cadmium telluride, CdTe, ~5% and copper indium gallium selenide, CIGS, ~2%) due

to the toxic raw materials and expensive fabrication process^{15,16}. The emerging thin-film PVs are referred to as using the current technologies that have the potential to overcome the Shockley-Queisser limit based on their novel materials for the semiconductors. Such thin-film PVs include organic photovoltaic (OPV), quantum dot (QD) PV, and perovskite PV¹⁷. Most of them are specifically used for high-tech applications, such as the aerospace and the military, owing to their high production costs.

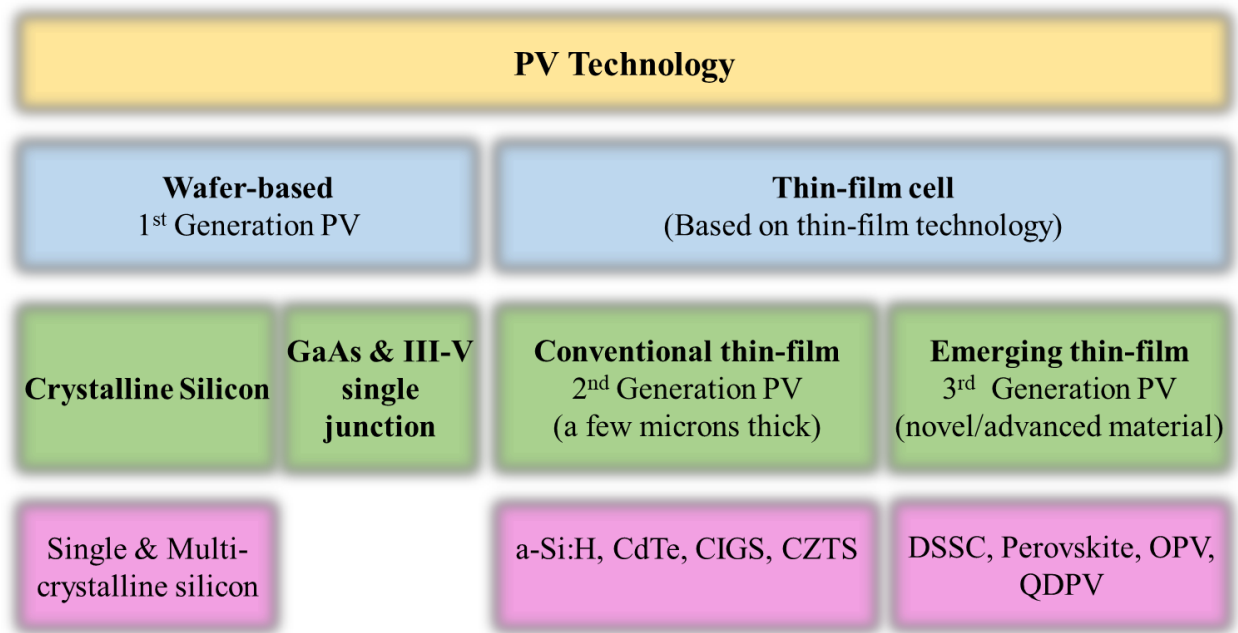


Fig. 1.2-1 Various generations of PV: 1st wafer-based; 2nd conventional thin-film; 3rd emerging thin-film.

In addition to the aforementioned three generation solar cells, III-V multijunction solar cells currently hold the undeniable world record for high-efficiency photovoltaics (~42%)¹⁸. The high

efficiency of III-V multijunction solar cells is largely due to the tunable bandgap, which has the III-V materials epitaxially grown on the lattice-matched substrate with a low crystal defect density. For example, the line Ge-GaAs-GaInP-AlAs can almost cover the whole visible light spectrum at the lattice parameter ≈ 5.65 ¹⁹. Thus, by reasonably controlling the multiple (i.e., binary, ternary, or quaternary) stoichiometry system, more than one p-n junction can be grown on the substrate in a series of layers, like a tandem. Each p-n junction in the device could be capable of efficiently absorbing a particular portion of the visible light spectrum. These high-efficiency solar cells are suffering from the high cost and toxic raw materials, and thus makes this kind of solar cell only suitable in a few specialized fields.

1.3 Theoretical Shockley-Queisser Efficiency Limits

The first researchers to estimate the highest theoretical solar cell efficiency using "Shockley Semiconductor" (i.e., single-junction solar cell) were William Shockley and Hans-Joachim Queisser in 1961, and their paper is widely regarded as one of the most important contributions to the field of photovoltaics²⁰. As a result, the Shockley-Queisser limit, based on the principle of detailed balance, can be defined as the theoretical efficiency upper limit of a solar cell, which is the maximum amount of electrical energy converted from an incident photon by a solar cell. According to the calculations, the greatest solar power conversion efficiency (PCE) for a single-junction solar cell with a band gap of 1.4 eV using the AM 1.5 G solar spectrum is 33.7%, see Fig. 1.3-1²¹. Three main factors limiting the conversion efficiency are introduced as follows:

Spectrum Losses: The different bandgaps of the raw materials will give the boundaries on the photons' utilization in a solar spectrum. For example, the widely used material GaAs has a bandgap ~ 1.4 eV. All photons with the energy less than this amount will not have enough energy to excite the electrons from the valence band. Consequently, further losses are generated as heat due to the

excess energy that the cell does not capture. This trade-off process should be taken into consideration when we make a selection on bandgap²². Thus, either a larger band gap will limit the number of the generated electron-hole pairs, or a smaller band gap will help the semiconductor generate more electron-hole pairs but the lower internal energy. Ignoring all other practical factors, these losses can be achieved at around the 33% of the incident light.

Recombination: Although an electron-hole pair generated by absorbing the photons can contribute to the current, the reverse process also exists by combining the electrons and holes. This process will restrict the open-circuit voltage (V_{oc}) and reduce the PV's theoretical efficiency by ~10% as the thermal losses²³.

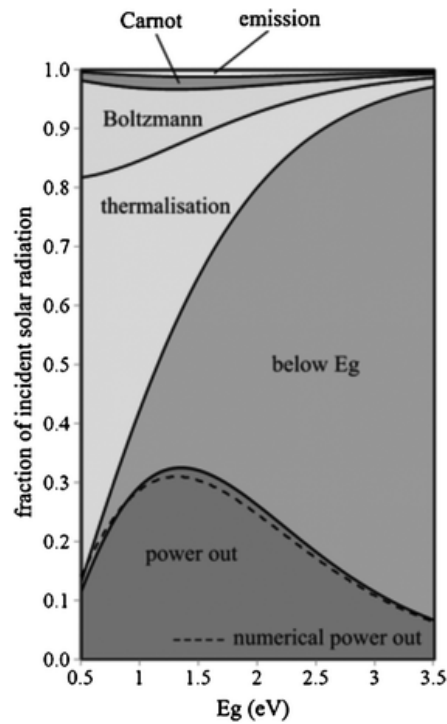


Fig. 1.3-1 The Shockley-Queisser limit for the maximum efficiency generated by a solar cell (output) and the inevitable loss (the rest part).

- **Blackbody radiation:** Any material emits electromagnetic radiation through the black-body radiation effect at room temperature. Therefore, any ineffective process, as mentioned before, will increase the temperature of the cells, leading to outgoing radiation and heat loss through the conduction and convection heat transfer processes²⁴. In our case, a very small part of the black-body radiation effect is caused by those photons having greater energy than the band gap, wherein the recombination process generates a part of these photons. In a cell at room temperature, the black-body radiation effect contributes to ~7% energy loss of the total input energy on the cell.

To be noticed, the Shockley-Queisser limit only applies to those solar devices having a single p-n junction. The solar cells with multiple junctions or novel materials (e.g., perovskite, dye-sensitized, and organic solar cells) can outperform this limit. For a multi-junction solar cell, the corresponding limit can be achieved at ~68.7% under the normal incidence²⁵. For the third-generation photovoltaic cells, the current study shows the maximal efficiency would reach up to ~70% by modifying the spectrum of the semiconductor's absorptance externally or isolating entropic losses²⁶. However, the modern commercial solar cells only produce a lower efficiency than the theoretical limit. The losses are largely due to some practical concerns, such as the reflection off the front of the cell or the light blockage from the electrodes on the cell surfaces. Thus, the practical issues mainly cause the insufficient light intensity falling on the solar surfaces. Therefore, beyond the material development of the solar system, there is another way to rationally manipulate light, such as an efficient light-trapping scheme.

1.4 Light-trapping Properties

Considering the three generation solar cells and the theoretical limits as mentioned earlier, there is no doubt that the current commercial solar cells are suffering from their poor efficiency. On the one hand, around 90% of the market share is the first generation solar cells. Despite being one of the most abundant materials on earth, silicon only achieves up to 10% PCE for commercial thin-film solar cells and 18% PCE for commercial bulk solar cells due to its indirect band gap nature²⁷. On the other hand, the thin-film solar cells (i.e., second generation solar cells) control around 10% of the market share. One major advantage of thin-film solar cells is the cost, which is approximately 30% less than bulk cells, owing to the thinner semiconductor layer. However, less sunlight will be absorbed if the semiconductor layer's physical thickness is decreased. Therefore, an optimum solar cell structure will typically have a "light-trapping" property, in which the optical path length is several times the actual device thickness, wherein the optical path length of a device refers to the distance that an unabsorbed photon may travel within the device before it escapes out of the device. It is possible to increase the photon flux per unit volume using light-trapping techniques, allowing for a reduction in the quantity of the solar cell material. The optical thickness of the solar cells is proposed to be increased by lengthening light path, compensating for the reduced volume. As the PV development moves toward thin and ultra-thin solar cells, the need for advanced light trapping structures becomes more critical. Apparently, the light trapping principles to optimize a single junction cell's efficiency are:

- Minimizing the surface optical loss,
- Prolonging the optical path length,
- Increasing the photon collection by a semiconductor,
- Coupling and guiding the incidence.

Several approaches are proposed to meet the above requirements: 1) an anti-reflective coating (ARC); 2) a back reflector; 3) the nanostructured layers including ARC, back reflector, and semiconductor layer. **Fig. 1.4-1** shows the schematic illustration of the optical effect for the traditional light-trapping structure/layer design as aforementioned.

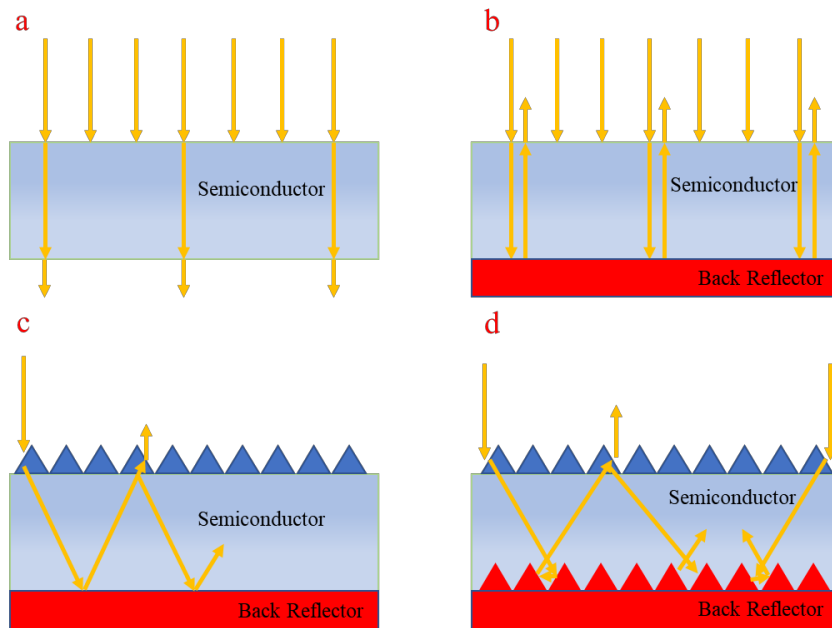


Fig. 1.4-1 Schematic illustration of the optical effects for light-trapping schemes, (a) a semiconductor without any light-trapping scheme; (b) a semiconductor with a back reflector; (c) a semiconductor with a nanostructured ARC and a back reflector; (d) a semiconductor with a nanostructured ARC and a nanostructured back reflector.

For the ARCs, they utilize a thin transparent layer above the semiconductor material such that interference effects lead to reduced reflectivity. The thickness of the coating is dependent on the wavelength of the incident wave on the dielectric material. The minimum reflection is given

by a thickness (d) of material with refractive index (n), in the following relation²⁸:

$$d = \frac{\lambda}{4n} \quad (2)$$

To maximize the interference effects, the refractive index of the ARC is rationally chosen by calculating the geometric mean of the materials on both sides (e.g., air at the top and Si at the bottom). It can be expressed by^{28,29}:

$$n_{ARC} = \sqrt{n_1 n_2} \quad (3)$$

where n_1 is the refractive index of the top layer material or surrounding medium, and n_2 is the refractive index of the bottom layer.

While ARCs can reduce overall reflectance, and this can be further improved with multiple layers. For example, based on the AM1.5 G photon flux from 300 nm to 1150 nm, Wright et al. calculated and simulated the reflectance of the polished crystalline silicon wafer with the double ARCs (i.e., layer 1: SiN and layer 2: SiO²). Their results show that the single layer SiN ARC manages minimum reflectance of 0.104, and the combination of SiN and SiO² can give us an extremely low overall reflectance of 0.044. The equations are more difficult for multi-ARCs than for a single one, and well explained by the following equations³⁰.

First, we establish the following parameters: r_1 , r_2 , r_3 , θ_1 , and θ_2 , which are reflectance (r) for each layer and refracted angle (θ) at normal incidence. The surrounding area has a refractive index of n_0 , and the next layer has a refractive index of n_1 and a thickness of t_1 . The layer immediately under the first layer has a refractive index of n_2 and a thickness of t_2 , and the third layer (i.e., semiconductor layer) has a refractive index of n_3 ³¹.

$$r_1 = \frac{n_0 - n_1}{n_0 + n_1} \quad (4)$$

$$r_2 = \frac{n_1 - n_2}{n_1 + n_2} \quad (5)$$

$$r_3 = \frac{n_2 - n_3}{n_2 + n_3} \quad (6)$$

$$\theta_1 = \frac{2\pi n_1 t_1}{\lambda} \quad (7)$$

$$\theta_2 = \frac{2\pi n_2 t_2}{\lambda} \quad (8)$$

The total reflectance for the whole device can be calculated, and the equation is derived as follows^{32,33}:

$$R = |r^2| = \frac{r_1^2 + r_2^2 + r_3^2 + r_1^2 r_2^2 r_3^2 + 2r_1 r_2 (1 + r_3^2) \cos 2\theta_1 + 2r_2 r_3 (1 + r_1^2) \cos 2\theta_2 + 2r_1 r_2 (1 + r_3^2) \cos 2\theta_1 + 2r_1 r_3 \cos 2(\theta_1 + \theta_2) + 2r_1 r_2 r_3 \cos 2(\theta_1 - \theta_2)}{1 + r_1^2 r_2^2 + r_1^2 r_3^2 + r_2^2 r_3^2 + 2r_1 r_2 (1 + r_3^2) \cos 2\theta_1 + 2r_2 r_3 (1 + r_1^2) \cos 2\theta_2 + 2r_1 r_3 \cos 2(\theta_1 + \theta_2) + 2r_1 r_2 r_3 \cos 2(\theta_1 - \theta_2)} \quad (9)$$

By optimizing the refractive index and the thickness of the two layers and neglecting the practical errors, an overall reflectance of the whole device will eventually produce minimal values at a single wavelength. For example, we assume that the first layer is our ARC having a refractive index: 1.4, the second layer is an ITO layer having a refractive index: 1.97, and the third layer is our semiconductor layer having a refractive index: 3.4. After we calculate the best thickness of these layers, the minimal reflectance can be achieved and shown in **Fig. 1.4-2**.

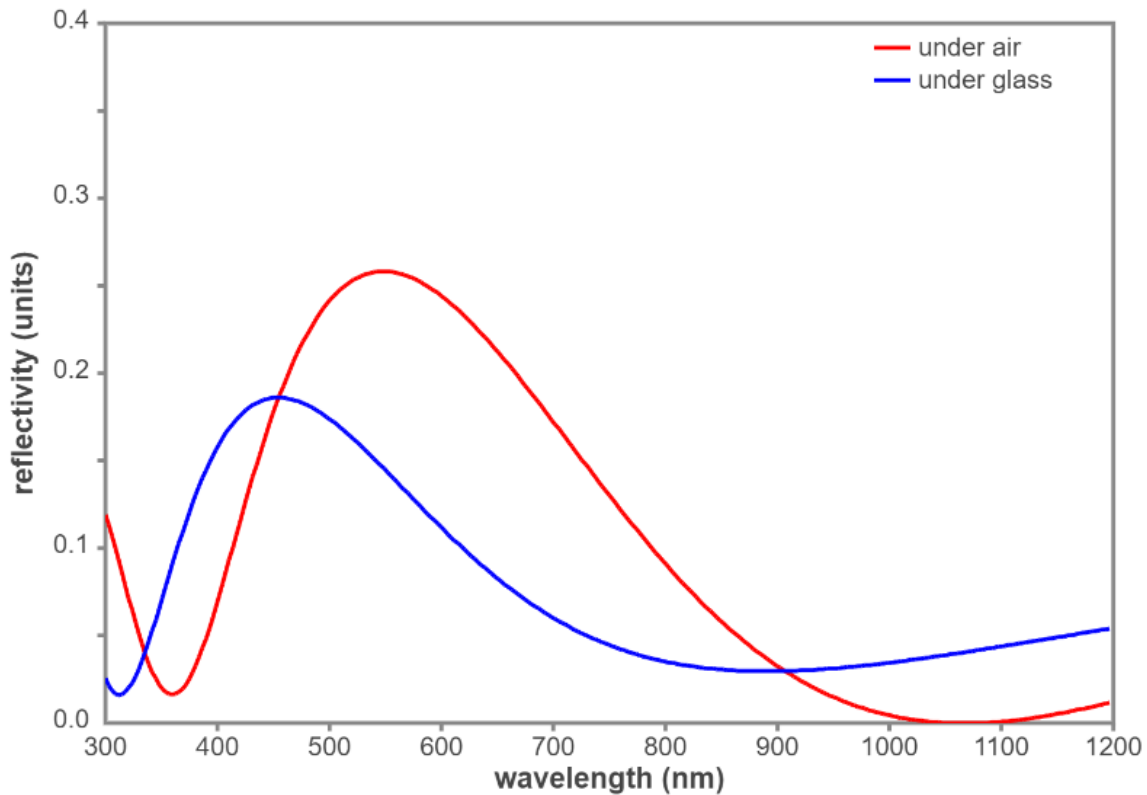


Fig. 1.4-2 The reflectivity of the Si-based solar cell with/without an ARC with the optimal thickness and ITO glasses.

The light-trapping property at the rear side is also crucial to achieve high efficiency by improving the short circuit current density. The conventional back reflectors are consequently designed for cells based on highly reflective materials, such as ZnO:Al/Ag. It allows the transmitted light to be reflected back into the cells again. We have the potential to increase the absorption by a factor of $4n^2$ by rationally applying a back reflector³⁴. In other words, it makes it possible for optical paths to be 50 times longer than the thickness of the actual device, making a successful light-trapping technique.

1.5 Nanostructure-based Technology

Alongside the ARCs and back reflectors, applying nanostructures to the layers inside solar cells is another typical approach for light-trapping properties. Any layers or coatings with nanosized grains or phases that range in size from a few to hundreds of nanometers are referred to as a nanostructured layer (see **Fig. 1.4-1 (c) – (d)**). In a variety of applications, these layers or coatings can provide a range of outstanding engineering properties, such as self-cleaning, anti-reflection, anti-microbial, and corrosion/erosion protection.

Periodic, random nanostructures have been developed and investigated for a wide range of purposes. As an illustration, periodic moth-eye design appropriately manages light on solar cells. One obvious optical effect is the diffraction, which usually takes place in the periodic structures. As it strikes the periodic nanostructured surface, the light will be refracted into distinct directions at specific angles, a process known as diffraction. The ability of periodic nanostructures to couple the incident light into more diffraction orders is in favor of light trapping properties³⁵.

In contrast, photonic random nanostructures possess exotic properties like more abundant Fourier spectra, resulting in Anderson light localization. For instance, random nanostructure inspired by glasswing butterfly has the omnidirectional and broadband anti-reflection, and structural color properties³⁶.

Consequently, nanostructure-based technology is more effective as it may randomize, re-direct, and prolong the optical length (i.e., light path) due to the nanostructured surface (i.e., rough surface) rather than a flat surface (i.e., smooth surface). It will satisfy the four factors for a light-trapping scheme, as aforementioned. Different optical effects can be achieved by modifying the direct or indirect parameters of the nanostructures, including the pitch sizes, the heights, the filling

ratio, the arrangement of the nanostructure and the spatial distribution of the nanostructure. Detailed principles and explanations will be further discussed in the following chapters.

The conventional nanostructures are classified into four categories based on their dimensions: 0-dimension (0D), 1-dimension (1D), 2-dimension (2D), and 3-dimension (3D). To be more specific, 0D refers to the structures that do not have any dimensions larger than nanoscales, such as particles and quantum dots. 1D referred to those structures only having one dimension belonging to nanoscales, such as grating. According to this rule, 2D and 3D are easy to be concluded. **Fig. 1.5-1** shows the examples of multidimensional nanostructures are categorized according to their sizes³⁷.

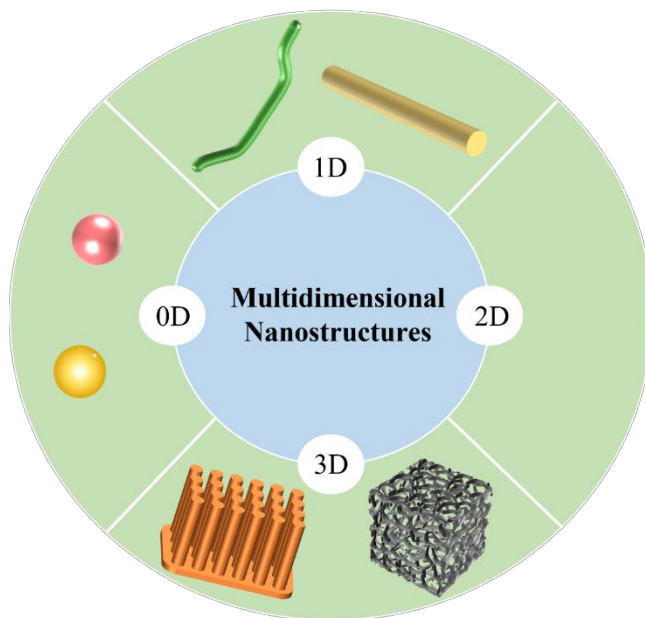


Fig. 1.5-1 The examples of multidimensional nanostructures listed as: (1) 0D; (2) 1D; (3) 2D; (4) 3D.

1.6 Objective of the Dissertation

The main objective of this dissertation is to propose highly effective approaches for designing, modeling, and optimizing nanostructures based on the advanced light-trapping schemes. In this dissertation, nanostructured ARCs or semiconductor layers are chosen as our embodiments to illustrate our concepts. The light-trapping concepts we show above are based on the literature review that the geometric parameters of the nanostructures (e.g., pitch size, height, shape, and the types of nanostructures), the spatial arrangement of the nanostructures (surface array, e.g., spiral, zigzag, concentric circles), and the spatial distribution (surface distribution for 2D and spatial distribution for 3D) of the nanostructure would be the main factors for the efficient light-trapping property. Therefore, in this dissertation, the following technical questions are addressed:

- 1) How to efficiently design and modeling the nanostructure using programmable binary data?
- 2) What are the best geometric parameters of nanostructures for the broadband visible light spectrum?
- 3) What is the best type of the nanostructure (i.e., periodic, random or quasi-random nanostructures) for the efficiency of the PVs?
- 4) What is the effect of the nanostructures' spatial arrangement on the light-trapping capacity?
- 5) How to characterize the optical properties of the quasi-random nanostructures (QRNs) based on their spatial distribution?
- 6) How does the multi-dimensional nanostructure pattern with different spatial distributions affect the quasi-random nanostructures?

- 7) How does the multi-dimensional nanostructure pattern affect the absorptance of a semiconductor?
- 8) How to optimize the quasi-random nanostructure to get a better and broader wavelength absorption of the solar devices under the normal and angular incidence?

1.7 Organization of the Dissertation

The thesis is organized into seven chapters. The contents of all sections are described below:

- i. CHAPTER ONE includes a general introduction as general background, challenges and efficiency limitation for PVs, research aims and objectives, and thesis organization are described in this chapter.
- ii. CHAPTER TWO describes a solar cell theoretical background, physics of the solar cells, solar cell parameters, and characteristics of electrical and optical properties of the solar cells, including a brief overview of the p-n junction, I-V characteristics, reflection, etc...
- iii. CHAPTER THREE introduces a numerical simulation for the solar cells (i.e., FDTD simulation), including its backgrounds, solver physics, parameter setting, and primary solutions.
- iv. CHAPTER FOUR presents a novel method to generate hybrid 2D quasi-random nanostructures by using programmable binary data and spiral arrangement. The optical and electrical performances are evaluated and discussed in this CHAPTER compared to bare thin-film solar cells or with the 1D grating nanostructure. Questions 2, 3, and 4 are addressed.
- v. CHAPTER FIVE demonstrates the different optical and electrical performances of the solar cells with different types of 2D quasi-random nanostructures. By assessing and

optimizing the quasi-random nanostructures based on their “star discrepancy” (i.e., the degree of surface randomness), questions 5, 6 and 8 are addressed

- vi. CHAPTER SIX is an extension of CHAPTER FIVE to further investigate the quasi-random nanostructures in 3D. The degree of spatial randomness is employed due to the randomized heights assigned to the 2D quasi-random nanostructures, which aims to answer questions 7 and 8.
- vii. CHAPTER SEVEN is the conclusions and future work.

2 CHAPTER TWO: FUNDAMENTALS OF SOLAR CELLS AND OPTICAL CHARACTERISTICS

2.1 Working Principles of a Semiconductor

The purpose of using a photovoltaic device is to convert sufficient solar energy into electricity. This process requires a unique material to absorb the light and produce both a current and a voltage. When the photon energy excites the electrons from a lower energy state to a higher energy state, the transport of these electron will lead to generating a drift external current. The excited electrons will fall back to their original energy state after dissipating their energy into electricity. The excited electrons are also called free carriers, which have free motion inside the material. **Fig. 2.1-1** shows the three different types of material based on their band gaps, namely: 1) insulator; 2) semiconductor; 3) conductor. It is not hard to conclude that the aforementioned process will not happen in insulators and conductors. For the insulators, the band gap (i.e., E_g) is so large that the materials need an extremely large amount of energy to excite the electrons from the valence band to the conduction band. For insulators, the valence band and the conduction band are overlapped so that the electrons can move without any restrictions. For the semiconductors, the band gap is small enough to allow the electrons to become free electrons by jumping from the valence band to the conduction band in response to the external energy input (i.e., electricity, light, and heat). Therefore, these unique materials are usually called semiconductor materials in the form of a p-n junction.

A p-n junction is a boundary or interface between the p-type and n-type semiconductor material inside a semiconductor. The process of doping produces the p-n junction in a semiconductor. In other words, the semiconductor has an excess of holes on the p-side, also known as the positive side, and an excess of electrons on the n-side, also known as the negative side.

Electrons diffuse from the n-type side to the p-type side because the n-type region has a high electron concentration, and the p-type region has a high hole concentration. The same diffusion movement happens to holes from the p-type to the n-type³⁸. When the diffusion process happens, the more positive ion cores in the n-type material and the more negative ion cores in the p-type material will therefore create an electrical field (i.e., \mathbf{E}), called the "depletion region". It is because the electric field quickly sweeps free carriers out, and the region is depleted of free carriers. A "built-in" potential V_{bi} is formed at the junction due to \mathbf{E} when we have an open circuit. Particularly, this "built-in" potential voltage can drift the light-generate carries within a p-n junction.

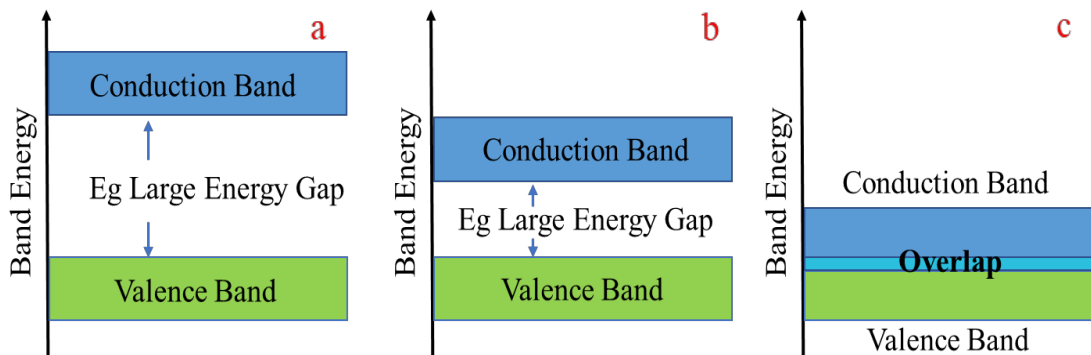


Fig. 2.1-1 Energy band in materials, (a) insulator; (b) semiconductor; (c) conductor.

2.2 Characterization of the Solar Devices (Overview)

Two crucial processes are involved in the production of "light-generated current", which is the current produced by an illuminated solar cell. To form electron-hole pairs, incoming photons must first be absorbed by a semiconductor. If the incident photon has an energy greater than the band gap, electron-hole pairs will be produced in the solar cell. However, due to their meta-stable

property, electrons in p-type materials and holes in n-type materials can only persist for about as long as the minority carrier lifetime before recombining. If the carrier recombines, no current or power can be generated due to the electron-hole pair loss³⁸⁻⁴⁰.

In a second process, by utilizing a p-n junction to spatially separate the electrons and the holes, the recombination can be effectively prevented. The carriers are separated by the action of the electric field (i.e., E) existing at the p-n junction. In other words, if a light-generated minority carrier reaches the p-n junction, it is swept across the junction by the electric field at the junction, where it will become a majority carrier. Suppose solar cell's emitter and base are connected are connected together (i.e., the solar cell is short-circuited), the light-generated carriers flow through the external circuit^{41,42}. The ideal flow at the short circuit is shown in **Fig. 2.2-1**.

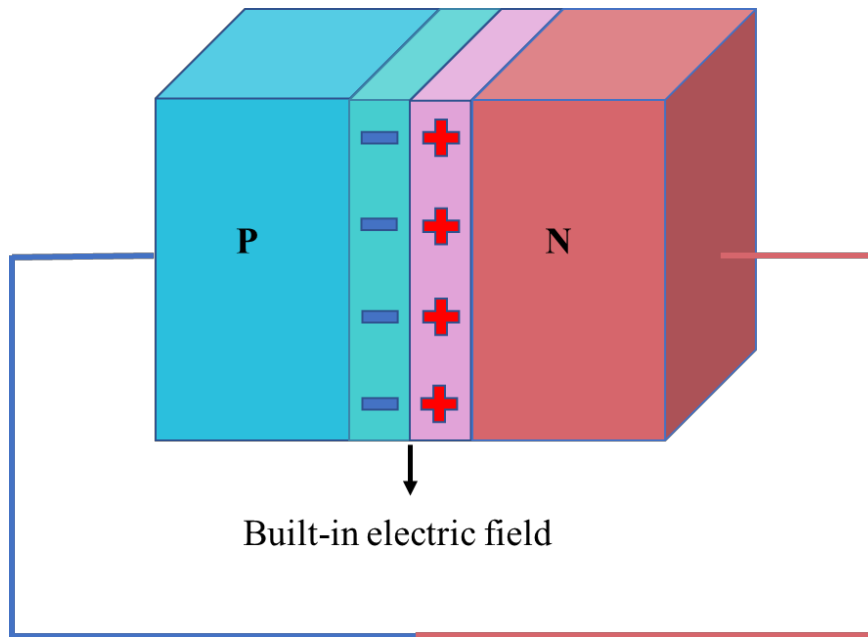


Fig. 2.2-1 Working principle of a solar cell with a p-n junction.

As a result, when an external circuit is applied to a p-n junction, the carriers no longer travel randomly but instead tend to drift in or out of the p-n junction, creating a current known as drift current that is dependent on the electric field. To be noticed, the p-n junction's material will attribute and affect dark saturation current without the illumination, depending on the recombination. Particularly, a p-n junction would have a large saturation current if its recombination rate was high, and more specific explanations about the relationship between current and voltage are discussed in section 2.3.

2.3 I-V Curve, Short Circuit Current and Open Circuit Voltage

An original I-V curve is the superposition of the I-V relationship of the solar cell in a dark environment with a light-generated current. Without illuminating a cell, a solar cell has the same electrical characteristics as a large diode, and the diode current equation is explained by Shockley's equation and defined as⁴³:

$$I = I_0 \left[\exp\left(\frac{V_d}{cV_t}\right) - 1 \right] \quad (10)$$

where I represent the diode current and I_0 is the reverse saturation current, V_d is the voltage across the diode, and c is a semiconductor constant that is usually set as 1~2. More specifically, V_t is the thermal voltage and can be extended to be $V_t = kT/q$ (k is the Boltzmann constant = 1.38×10^{-23} J/K, T is the temperature and q is the magnitude of the electronic charge = 1.6×10^{-19} C). So, the diode current equation can be further derived as:

$$I = I_0 \left[\exp\left(\frac{qV_d}{ckT}\right) - 1 \right] \quad (11)$$

Illuminating a cell adds to the normal “dark” current in the diode so that the diode equation becomes:

$$I = I_0 \left[\exp\left(\frac{qV_d}{ckT}\right) - 1 \right] - I_L \quad (12)$$

where I_L = light generated current. Plotting the above equations gives us the I-V curves with/without illumination, as shown in **Fig. 2.3-1**.

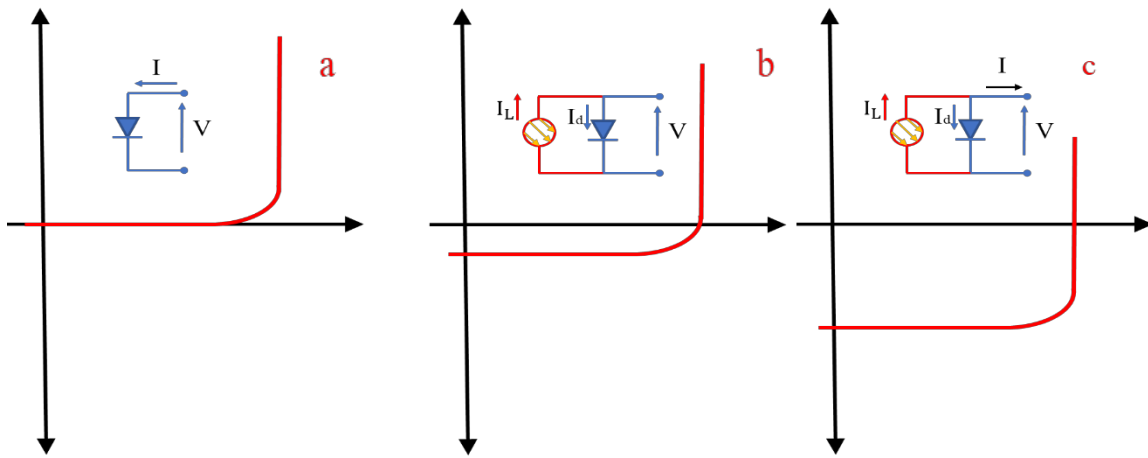


Fig. 2.3-1 The effect of light on the current-voltage characteristics of a p-n junction (x -axis: current, y -axis voltage), (a) the electrical characteristics without illumination (working as a large diode); (b) the shifted I-V curve with low incoming light intensity; (c) a standard I-V curve with normal illumination.

Based on the equations and plots, the term “-1” in the above equation are usually neglected for practical purpose. The exponential term is always $\gg 1$ with a larger applied voltage, while the light-generated current I_L dominates the equation with a small enough applied voltage so the term “-1” is no longer needed under the illumination. The working current for a solar cell under the illumination finally becomes:

$$I = I_L - I_0 \left[\exp \left(\frac{qV_d}{ckT} \right) \right] \quad (13)$$

Rearranging the voltage-current equation in the Eq. (13)⁴⁴:

$$V = \frac{ckT}{q} \ln \left(\frac{I_L - I}{I_0} \right) \quad (14)$$

Aside from these essential parameters, other significant parameters of a solar cell should be calculated and assessed, such as short-circuit current density (J_{sc}) and open-circuit voltage (V_{oc}). Experimentally, the J_{sc} can be derived from the I-V curve under the normal illumination when the external bias voltage is zero, see **Fig. 2.3-1**. From the plot, we can find out the short circuit current I_{sc} is at the intersection of the line and V (unit) axis. Therefore, assume the illuminated area to be A , the short circuit current density becomes:

$$J_{sc} = \frac{I_{sc}}{A} \quad (15)$$

There is no denying that the I_{sc} has a relationship with the intensity of the light source. For an effective light-trapping scheme, improving the optical path aims to improve the intensity of the light source, which leads to the enhancement of the I_{sc} . From another perspective, the current from a cell is generated due to the solar radiation, and at most one quantum of charge is generated per absorbed photon, denoted by $F(\lambda)$ (photon intensity per area per wavelength, $\text{Wm}^{-2}\text{nm}^{-1}$). For different materials, photons may not be absorbed at some wavelengths due to the weak absorption of the material. Furthermore, the cell may not generate one quantum of the charge for every absorbed photon. The external quantum efficiency (EQE) is employed and calculated for these two effects. Therefore, the J_{sc} could also be calculated as⁴⁵:

$$J_{sc} = q \int F(\lambda) EQE(\lambda, 0) d\lambda \quad (16)$$

where the EQE function will be detailed in following section 2.5.

Another crucial parameter for solar cells is the open-circuit voltage, which is the greatest voltage a solar cell can produce while there is no current flowing through it. The factors that can affect the V_{oc} are the band gap of the material, the built-in voltage, the intensity of the illumination, the reverse saturation current, the diode ideality factor, and the device parasitic resistances, etc.

- The change of the solar cell's temperature will lead to the change of V_{oc} linearly.
- The larger built-in voltage of a p-n junction caused by the larger bandgap of the p-n junction material will give a larger V_{oc} .
- Based on the Eq. (14), a minor increased V_{oc} is observed under a higher intensity of the illumination due to the exponential nature of the p-n junction's I-V characteristics.

The resistance of the solar cell will affect the open circuit voltage as well as fill factor (see section 2.4).

2.4 Fill Factor, Maximum Power, and Power Conversion Efficiency

The maximum current and voltage from a solar cell are known as the short-circuit current and open-circuit voltage, respectively. For both conditions, the solar cell's power output is zero when the output power $P_{out} = V_{oc} \times I_{sc}$. The "fill factor," abbreviated "FF," is a quantity parameter combined with V_{oc} and I_{sc} and determines the maximum power (P_{max}) output of a solar cell. The equation becomes⁴⁶:

$$FF = \frac{P_{max}}{V_{oc} \times I_{sc}} = \frac{V_{mp} \times I_{mp}}{V_{oc} \times I_{sc}} \quad (17)$$

As shown in **Fig. 2.4-1**, the FF is a measure of the "squareness" of the solar cell and is also of the area of the largest rectangle, which will fit into the I-V curve. Based on the above equation,

the $FF = \text{area A}/\text{area B}$. The Eq. (17) shows that a higher voltage will have a higher possible FF. However, the variations in open circuit-voltage can not be large enough within the same material system. It only can be significant for solar cells made of different materials. For example, a silicon-based solar cell has around a 0.83 FF value compared to a GaAs with a 0.89 FF value. Therefore, FF is an ideal factor for assessing the quality of the junctions and the recombination effect in a solar cell. The recombination mechanisms are not explained here, but they will cause the low open-circuit voltage with the high recombination effects.

The efficiency of a solar cell is the most commonly used parameter to evaluate the various solar cells' performance, which is the ratio of the output energy from a solar cell to the input energy given by the light source. In addition to reflecting the performance of the solar cell itself, the efficiency depends on the solar spectrum, the intensity of the incident sunlight, and the temperature of the solar cell. When evaluating the efficiency of one solar cell compared to another, these parameters should be carefully controlled. Based on the aforementioned equations, the input energy power is equal to the maximum power ($V_{mp} \times I_{mp}$). Therefore, the efficiency of a solar cell is defined as⁴⁶:

$$\eta = \frac{V_{oc} I_{sc} FF}{P_{in}} \quad (18)$$

where the input power is based on standard AM 1.5G (1000W/m²).

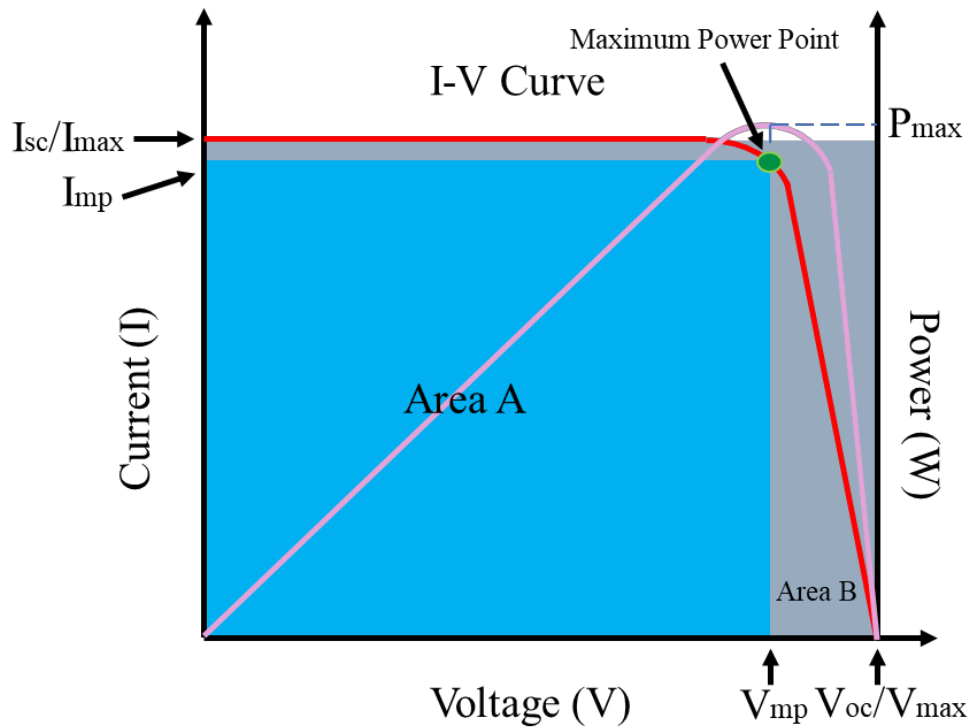


Fig. 2.4-1 A standard I-V curve of a solar cell (red line) with identified I_{sc} and V_{oc} , and its output power.

2.5 Quantum Efficiency

The quantum efficiency (QE) is the ratio of the number of carriers collected by the solar cell to the number of photons given by a light source on the solar cell. Due to this ratio, the QE results are dimensionless. However, based on the physical EQE experiment, it can be expressed and described in amps per watt. Moreover, since the photons have a relationship (i.e., inversely proportional) with their wavelength, the virtualized QE result is usually shown over a range of wavelengths to evaluate the solar cell's efficiency with different photon energy levels.

Since the movement of the carriers inside a solar cell causes an amount of the current, one can evaluate this amount of the current by integrating the cell's efficiency over the entire solar

spectrum when the sunlight is shining on the cell's surface. The equation has been laid out as Eq. (16). There are two types of quantum efficiency for a solar cell:

- External Quantum Efficiency (EQE): This is the ratio of the number of charge carries generated by the solar cell to the number of photons given by a light source on the solar cell from the outside of the whole device (i.e., reflection and transmission included).
- Internal Quantum Efficiency (IQE): This is the ratio of the number of charge carries generated by the solar cell to the number of photons absorbed by the cell.

Without considering the reflection and transmission of a solar cell, the IQE is theoretically larger than the EQE. To be more specific, the IQE is a measure of the energy conversion capability of the active layer in a solar cell, while the EQE is a measure of the energy conversion capability of the whole solar device, including the optical loss, such as reflection. The relationship between the IQE and EQE can be further derived as the following equations⁴⁷:

$$EQE = \frac{\text{generated electrons/sec}}{\text{photons/sec}} = \frac{\frac{I_{total}}{q}}{\frac{E_{total}}{E_g}} \quad (19)$$

$$IQE = \frac{\text{generated electrons/sec}}{\text{absorbed photons/sec}} = \frac{EQE}{1 - R - T} \quad (20)$$

where I_{total} is the tested current, q is the charge of one electron (1.6×10^{-19} C), E_{total} is the total power of the photons, E_{ph} is the energy of one photon (i.e., $E_g = hc/\lambda$, see Eq. (1)), R is the reflectance of the entire solar device, and T is the transmission of the solar device. **Fig. 2.5-1** shows the QE of a crystalline silicon solar cell, and it indicates that the blue response ranging from around 200 nm to 495 nm is reduced to the zero due to the front surface recombination, and the red response is reduced to zero due to rear surface recombination and low diffusion lengths.

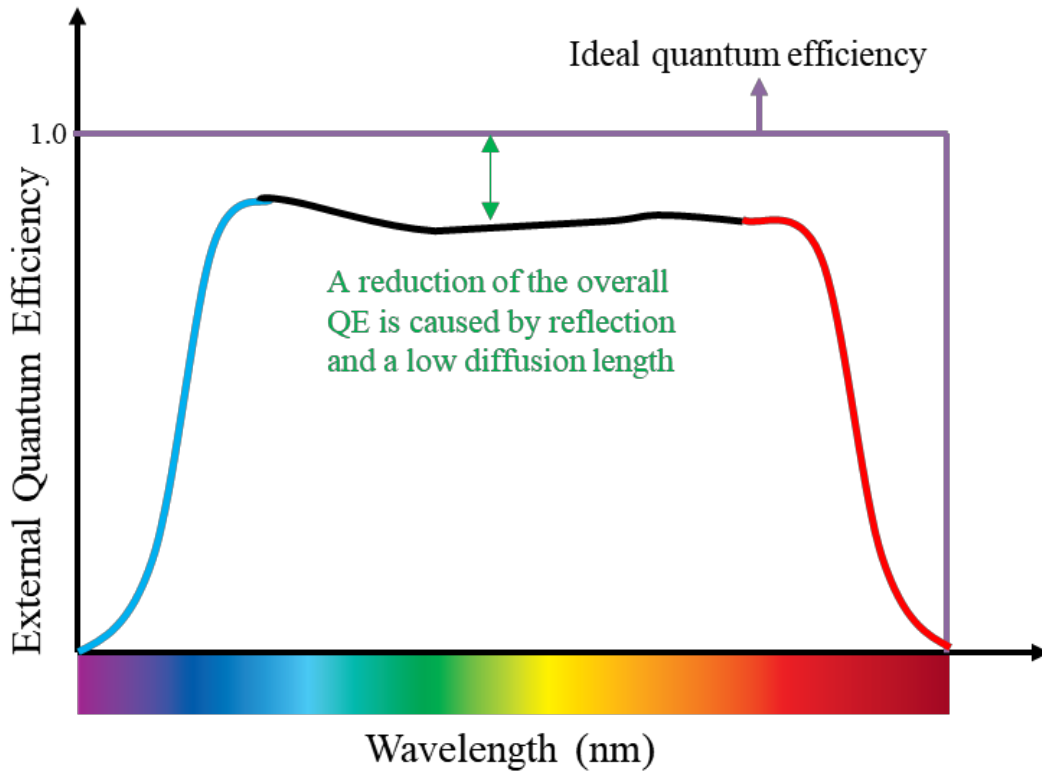


Fig. 2.5-1 The external quantum efficiency with wavelength of a crystalline silicon solar cell.

2.6 Reflection

The percentage of an electromagnetic wave is reflected at the interface depends on the reflectivity of a substance. Consider a simple illustration where two homogeneous, lossless, isotropic non-conducting/magnetic dielectric mediums are cross sectioned by a plane (preferably thin and infinite interface), the light wave is split into three distinct directions when it travels along this plane as seen in **Fig. 2.6-1**. (E_i : the incidence, E_r : the reflected wave, and E_t : the transmitted

wave). Based on the Maxwell's equations and boundary conditions, these three light waves can be expressed as⁴⁸:

$$E_i = E_{oi} \exp\{j[\omega t - n_1 k_0(x \sin \theta_i + z \cos \theta_i)]\} \quad (21)$$

$$E_r = E_{or} \exp\{j[\omega t - n_1 k_0(x \sin \theta_r + z \cos \theta_r)]\} \quad (22)$$

$$E_t = E_{ot} \exp\{j[\omega t - n_2 k_0(x \sin \theta_t + z \cos \theta_t)]\} \quad (23)$$

where the k_0 is the wave vector, n_1 and n_2 are the refractive of two medias.

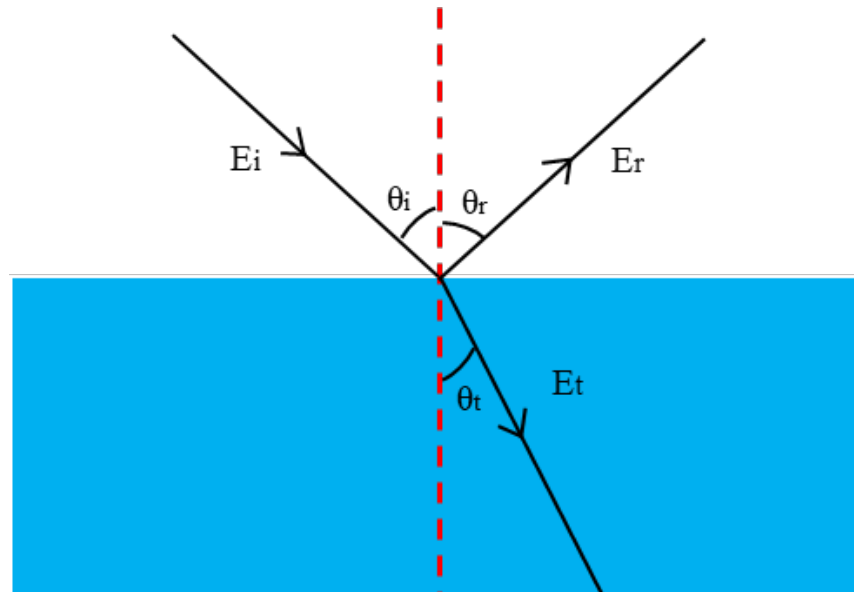


Fig. 2.6-1 Light propagating at a single plane interacts with the interface.

Thus, based on above equations and three identical waves, we get Snell's law⁴⁹:

$$\theta_i = \theta_r \quad (24)$$

$$n_1 \sin \theta_i = n_2 \sin \theta_t \quad (25)$$

We define the amplitude of E field to be A , and intrinsic impedance as Z_1 , which has the value $\mu_0 c / n_1$, and the magnitude of the H field amplitude as A/Z_1 (c is the light speed). The three sets of equations for E_i parallel to the incidence plane are:

$$E_{0i} = A(\vec{x} \sin \theta_i + \vec{z} \cos \theta_i) \quad (26)$$

$$H_{0i} = \left(\frac{A}{Z_1}\right) \vec{y} \quad (27)$$

$$E_{0r} = A'(\vec{x} \cos \theta_i + \vec{z} \sin \theta_i) \quad (28)$$

$$H_{0r} = -\left(\frac{A'}{Z_1}\right) \vec{y} \quad (29)$$

$$E_{0t} = A''(\vec{x} \cos \theta_t - \vec{z} \sin \theta_t) \quad (30)$$

$$H_{0t} = \left(\frac{A''}{Z_2}\right) \vec{y} \quad (31)$$

By considering the case at $Z=0$ at the interface, reflection coefficient can be derived as:

$$r_p = \frac{A'}{A} = \frac{n_1 \cos \theta_t - n_2 \cos \theta_i}{n_1 \cos \theta_t + n_2 \cos \theta_i} \quad (32)$$

Combining with Snell's law, the reflection coefficient can be further expressed as:

$$r_p = \frac{\tan(\theta_i - \theta_t)}{\tan(\theta_i + \theta_t)} \quad (33)$$

2.7 Optical Losses and Anti-reflectivity

Beyond the property limitations of the materials, the optical losses are the key factor affecting the efficiency of the solar cells, which becomes more severe when the solar cell has a larger incident angle. Optical losses are defined as when the incoming light source would be reflected by a smooth surface or shaded by the electrodes, and the light does not have a chance to reach to the semiconductor. Losing this fraction of light lowers the light intensity and is unable to provide the energy to generate the electro-hole pairs. The surface reflection is related to the refractive index of one or several layers inside the solar cells. Consequently, ARCs are widely used to minimize the effect of light reflections, as aforementioned. There are some strategies to achieve anti-reflection property:

- **Broadband anti-reflectivity** Anti-reflectivity needs to cover a broader range of the wavelength of the incidence⁵⁰. Typically, the wavelength of the visible light ranging from 300 nm ~ 900 nm is the best region for solar cells. Those wavelengths beyond 900 nm are not necessarily considered due to the lower energy below the bandgap energy. Using random nanostructures can largely improve the broadband anti-reflectivity by redirecting and prolonging the light path.
- **Omni-directional anti-reflectivity** Based on the Fresnel equations, the angle of incidence (AOI) plays a key role in the determination of reflectance. In fact, the commonly used ARCs (i.e., glasses and polymers) only have 4% reflection at the normal incidence^{51,52}. However, the reflectance can reach up to 100% at the grazing angles. Without building up a tracking system, the omnidirectional anti-reflectivity can be a strategy to address the issue.
- **Polarization insensitivity** Depending on Maxwell's equations, two types of polarization of light should be considered. The *s*-polarization carrying the electric field perpendicularly

propagates to the incidence plane, while the p -polarization carrying the electric field parallelly propagates to the incidence plane. Therefore, the s -polarization is mainly discussed in this dissertation.

3 CHAPTER THREE: NUMERICAL METHOD FOR SOLAR CELLS

3.1 Overview of Finite-Difference Time Domain (FDTD)

The FDTD method is one of the state-of-the-art methods using Maxwell's equations for complex geometries⁵³. Combining the time and space solution, it provides us a new possibility to solve all types of problems based on electromagnetics and photonics. In addition, by exploiting Fourier transforms, FDTD is given the capability to obtain the frequency solution, which means that the reflection/transmission of light related to the wavelength/frequency can be analyzed. By calculating how the EM fields propagate source through the structure, the simulation will be continued until there are essentially no electromagnetic fields left in the simulation region⁵⁴. Besides this, the frequency domain information located at different spatial points can be obtained via the Fourier transform based on the time domain information at the point. In other words, the power flow can be obtained over a wide range of frequencies from one simulation.

3.2 Solver Physics

In this section, the basic mathematics and physics formalism behind the algorithm is to solve the Maxwell's equations in dielectric materials⁵⁵:

$$\frac{\partial \vec{D}}{\partial t} = \nabla \times \vec{H} \quad (34)$$

$$\vec{D}(\omega) = \epsilon_0 \epsilon_r(\omega) \vec{E}(\omega) \quad (35)$$

$$\frac{\partial \vec{H}}{\partial t} = -\frac{1}{\mu_0} \nabla \times \vec{E} \quad (36)$$

$$\epsilon_r(\omega) = n^2 \quad (37)$$

where H , E and D are the magnetic, electric, and displacement fields, respectively, and $\varepsilon_r(\omega)$ is the complex relative dielectric constant.

In a three-dimensional (3D) space, the Maxwell equations contain six components, which are E_x , E_y , E_z , H_x , H_y , and H_z . For ease of simulation, the structure is assumed to be infinite in the z dimension so that the fields are independent of z , and the above equation can be further derived as:

$$\varepsilon_r(\omega, x, y, z) = \varepsilon_r(\omega, x, y) \quad (38)$$

$$\frac{\partial \vec{E}}{\partial z} = \frac{\partial \vec{H}}{\partial z} = 0 \quad (39)$$

In doing so, Maxwell's equations are converted into two independent sets of equations having three vector quantities each which can be calculated in the x - y plane. The **TE** (transverse electric) and **TM** (transverse magnetic) equations are the terms used to refer to these. By applying the following components, we can solve both sets of equations.

- **TM:** E_x , E_y , H_z
- **TE:** H_x , H_y , E_z

Take TM as an example, the Maxwell's equations can be derived as:

$$\frac{\partial D_z}{\partial t} = \frac{\partial H_y}{\partial x} - \frac{\partial H_x}{\partial y} \quad (40)$$

$$D_z(\omega) = \varepsilon_0 \varepsilon_r(\omega) E_z(\omega) \quad (41)$$

$$\frac{\partial H_x}{\partial t} = -\frac{1}{\mu_0} \frac{\partial E_z}{\partial y} \quad (42)$$

$$\frac{\partial H_y}{\partial t} = \frac{1}{\mu_0} \frac{\partial E_z}{\partial x} \quad (43)$$

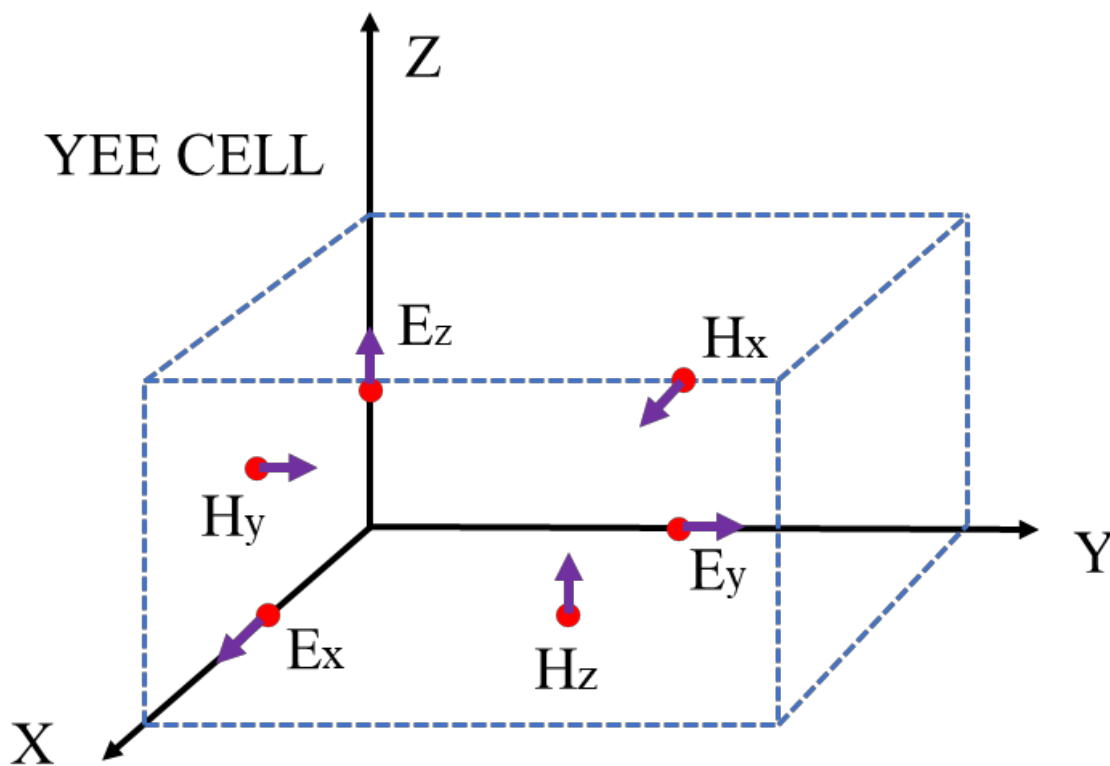


Fig. 3.2-1 The Yee Cell: a plot of the discretized field: E_x , E_y , H_z , H_x , H_y , E_z .

FDTD method solves these equations based on a discrete spatial and temporal grid (i.e., Yee cell)⁵⁶. Within a Yee cell, each field component is solved at a slightly different location, and data collected from the FDTD solver is automatically interpolated to the origin of each grid point (see Fig. 3.2-1).

3.3 Light Source

Different beam sources are chosen to satisfy various demands⁵⁷. In this thesis, two typical light sources (i.e., plane wave and BFAST source) are used and detailedly explained as follows:

- From a single pre-determined simulation zone, plane wave sources are employed to inject homogenous electromagnetic radiation. While the plane wave source in three-dimensional simulations injects along a plane, it injects along a line in two-dimensional simulations. It is also feasible to inject a plane wave at an angle. However, this may lead to diverging problems since the margins (i.e., Bloch/Periodic boundary conditions) of the simulation region will absorb some of the incompletely injected energy.
- When a broadband result at angled plane wave incidence is pursued with one simulation without using Bloch/Periodic boundary conditions, the Broadband Fixed Angle Source Technique (BFAST) can be used to sweep the wavelength or frequency.

3.4 Boundary Conditions (BC)

Three main BCs are introduced in this this section: Periodic BCs, Bloch BCs and PML BCs, and they are detailly explained as follows:

- Periodic BCs: By simulating and gathering the results from a single unit cell, Periodic BCs enable us to reduce the complexity of the simulation⁵⁸. The EM field responses that have been created on the other side of the boundary condition will be copied by the Periodic BCs after a successful FDTD simulation. Consequently, the advice for using periodic BCs is that the system needs to be periodic for both the physical structure and the electromagnetic fields. Some simulated results that were published and displayed in other articles turned out to be inaccurate. Although their structures are periodic, the EM fields for their nanostructures are not periodic.
- Bloch BCs: Bloch BCs are widely used in a variety of situations, but they are most frequently used in simulations when the periodic structures are illuminated by an angular incidence. Additionally, all BCs should be Bloch BCs if a BFAST source is used in a

simulation to prevent simulation mistakes. Bloch BC results will be equivalent to periodic BC outcomes under normal incidence.

- PML BCs: Normally, the PML BCs are designed to absorb the incident light source with minimal reflections⁵⁹. Therefore, the PML BCs are usually used for the z-direction, which is the same directions of the incidence. However, a limited number of reflections are always generated in practice as a result of the discretization of the underlying PML equations, and this may result in numerical instabilities. It is important to choose the right parameters to reduce reflection mistakes.

3.5 Reflectance and Transmittance Flux Spectra

When we set up the proper parameters, including the light source and BCs in a simulation, the FDTD simulations are consequently run to investigate the reflectance and transmittance flux as a function of the frequency of incident light. A single time-domain simulation assesses the power flux for a range of frequencies by using Fourier Transform (FT) to analyze the responses. The integral of the Poynting flux is calculated and used to compute the power at each frequency⁶⁰:

$$P(\omega) = R \iint E_{\omega}(x) \times H_{\omega}(x) dA \quad (44)$$

where the $E_{\omega}(x)$ is electric field with the specific frequencies and $H_{\omega}(x)$ is magnetic field with the specific frequencies.

To compute reflectance and transmittance spectra requires setting up two power flux monitors inside a simulation to record the incoming and outgoing fluxes for each simulation. The transmittance flux is then computed as the ratio of the transmitted power and the reference power as:

$$T(\omega) = \frac{P(\omega)_{out}}{P(\omega)_{ref}} * 100 \quad (45)$$

The incident and reflected power together make up the reflected power for reflectance. As a result, before taking the ratio, the entering power is subtracted from the reference:

$$R(\omega) = \frac{P(\omega)_{ref} - P(\omega)_{in}}{P(\omega)_{ref}} * 100 \quad (46)$$

4 CHAPTER FOUR: A BIOINSPIRED HYBRID LIGHT-TRAPPING STRUCTURE AND ITS FABRICATION FOR THIN-FILM SOLAR CELLS

4.1 Introduction

Thin-film solar cells are one of the important candidates for reducing the cost of photovoltaic production with less use of active materials. However, thin-film solar cells' low light absorption stifles their development when the photons have to be absorbed within a layer as thin as a few hundred micrometers (or less)⁶¹. An effective light-trapping structure/coating can address this optical challenge to maximize the solar cell's PCE. Over the past decade, quasi-random structures, as an alternative light-trapping structure to conventional periodic ones, have been intensively investigated due to their neither periodic nor fully disordered geometries, which can also be found in nature (e.g., sunflower, feather barbs)^{62,63}. Moreover, the biological surfaces in nature have developed to be multi-functional in order to furthest possess an outstanding ability to manipulate light during long-term evolution. Besides the light-trapping nanostructures, sunflowers also exhibit a unique spiral phyllotaxis structure arrangement to have superior and stable light capture capability⁶⁴⁻⁶⁷. For example, the seed-formed spiral in a sunflower enables the seed head to utilize the least amount of material and lowest energy to grow up, expand the structure in a deterministic way without reducing the light absorption and enhancing the structure tolerance. To date, far less attentions has been paid to spiral structure due to its complexity in nanomanufacturing. Thus, here we present a Hybrid Light-Trapping Structure/Coating (HLTSC) by combining the superiority of QRNs with an Archimedean Spiral Arrangement (ASA) to maximize solar energy conversion on thin-film solar cells. Moreover, as current complex nanostructured light-trapping structures are fabricated either through expensive and time-consuming top-down nanomanufacturing or the burgeoning but not yet perfected bottom-up fabrication processes, there is an urgent need to

develop a low-cost, fast-production, and reliable fabrication technique. In this chapter, we concurrently present a new manufacturing approach via the modern optical storage technique (e.g., optical discs). As a proof-of-concept, we coated the HLTSC on the silicon thin-film solar cells, confirming the improved photon absorption and energy conversion efficiency. In addition, we numerically demonstrate the advancement of this technique for enhancing broadband and omnidirectional light-trapping capacity. In summary, the presented study may open up a new area that repurposes a low-cost consumer product for high-end, value-added photovoltaic applications.

As discussed, the main challenge is to directly mimic the spiral curve in the plant, relying on expensive and time-consuming top-down nanomanufacturing such as e-beam lithography or focused-ion beam lithography. Fortunately, the Archimedean spiral can also be found on any data storage technique, such as CDs, DVDs, and Blu-rays. On a compact disc (i.e., Blu-ray), binary data with values “1s” and “0s” starts from the innermost track and is burned in an outward direction in a spiral arrangement⁶⁸. Thanks to the optical disc technology, it provides us advantages of low-cost and high throughput to directly fabricate “pits” and “lands” nanostructure form determined by binary data (i.e., 1s and 0s) along the spiral track (see **Fig. 4.2-1 (a)**). Inspired by sunflowers, we imported the binary Fibonacci (Fibo) sequence as our binary data to represent the relationship between pits and lands. That is because the Fibonacci sequence of numbers forms the best whole number approximation to the Golden Ratio, which is also found in sunflowers^{69,70}. This kind of structure offers a better volume fraction and filling ratio to capture the light. The most reliable study on 768 clockwise or anticlockwise parastichy numbers in sunflowers indicates that 80% of the parastichy numbers are Fibonacci numbers, which indicates the dominance of the Fibonacci structure in sunflowers. Furthermore, Smith *et al.* prove that the pattern generated from an optical disc belongs to quasi-random nanostructures, which gives us the following strategies for light

manipulation: 1) the Mie-scattering occurred due to the different nanostructure sizes formed from the wavelength range of 300 nm ~ 900 nm; 2) the local randomness broke the mirror symmetry at the microscopic and prolonged the light path due to the multiple internal reflections⁸.

4.2 Method

4.2.1 1D Fibonacci binary sequence design

Here, we imported the binary Fibonacci sequence as the guide of QRNs' design because its filling ratio approximates the Golden Ratio for light capturing. The Fibonacci pattern is the paradigm of deterministic quasi-periodic order that can be obtained by combining two different building blocks. The Fibonacci structure shows distinct diffractions that cannot be found in either periodic or random structures. The Fourier spectra of Fibonacci structures have isolated Bragg peaks with incommensurate periods, which appear to continuously fill into the reciprocal space, a typical feature of the quasi-random structure. These spectra feature lead to exciting physical properties possessed by Fibonacci patterns. In fact, they have been used to induce symmetry resonance, enhance the nonlinear coupling, and suppress the group velocity at the band edge states. Recently, it was also used for plasmonic light-trapping layers for thin-film solar cells and was discovered that it outperformed both periodic and random patterns.

In this case, to fabricate Fibonacci patterns, we will begin with, representing the “land” as blank and representing the “pit” as building blocks, respectively. According to the concatenation rule⁷⁰,

$$S_j = S_{j-1}S_{j-2} \quad (47)$$

The first six generations of the sequence will be generated like,

$$1 \rightarrow 11 \rightarrow 1110 \rightarrow 11101101 \rightarrow 1110110111100010 \quad (48)$$

The sequence can keep continuous. Recall that the quasi-random structures are mesoscale periodic. This fabrication method can create the mesoscale periodicity on demand by selecting a generation of the sequence as the element for repeating.

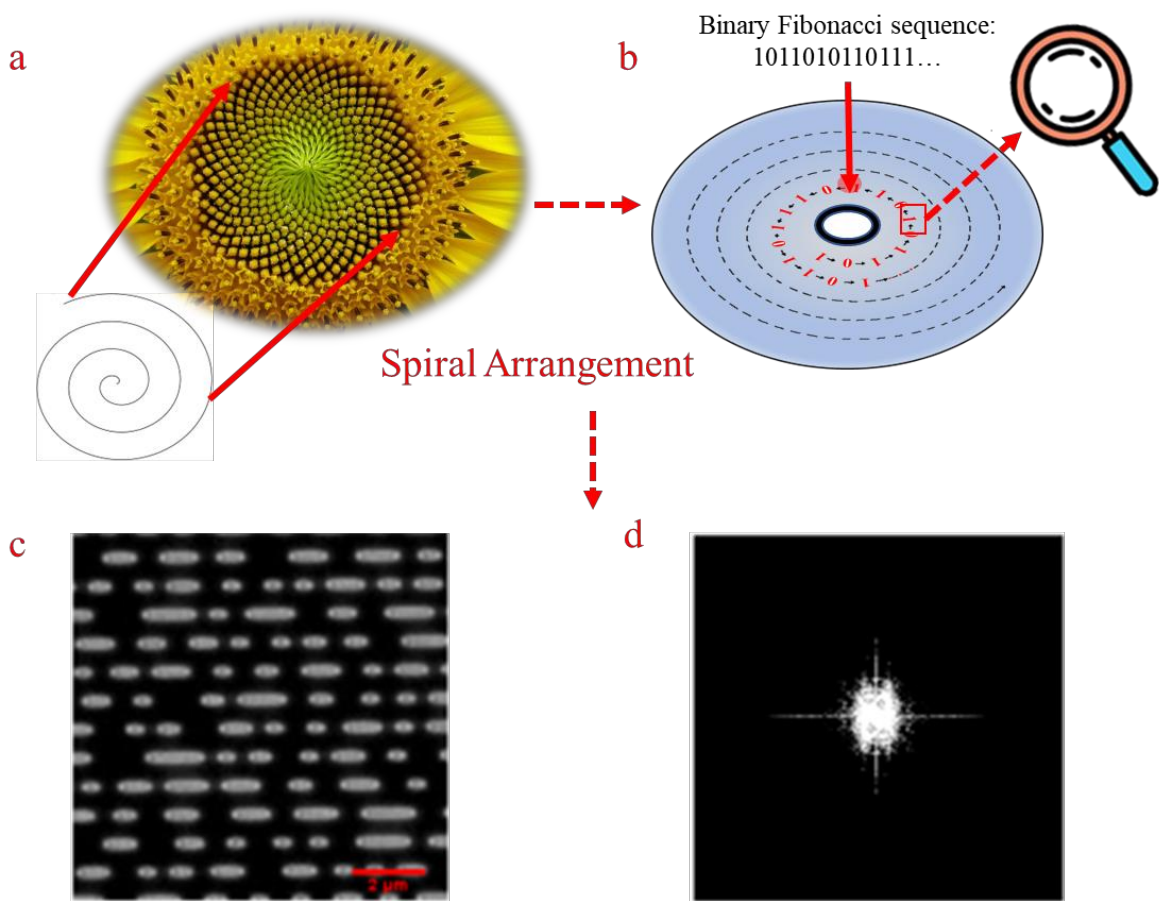


Fig. 4.2-1 (a) A spiral curve in a sunflower; (b) the schematic of a binary Fibonacci sequence mapped into writable disc; (c) the SEM image of the Fib QRN inside an optical disc; (d) the FT based on the SEM image of the Fib QRN.

4.2.2 Converting 1D binary sequences to virtualized 2D nanostructure patterns

Once the 1D binary Fibo sequence is confirmed, the entire binary sequence is further converted into a 2D binary matrix in a specific arrangement. In this CHAPTER, a spiral arrangement is used to arrange the 1D binary sequences into the 2D binary matrix, which is the Archimedean spiral arrangement inspired by the sunflower. This kind of 2D binary matrix can contribute to optimizing light capture because the structure arrangement correlation at the macroscopic has a significant impact on the optical performance of nanostructures. In doing so, the binary sequences with values “1s” and “0s” are arranged from the innermost track in the outward direction along the spiral track. This spiral arrangement can be easily realized by using optical disc technology, and it will be detailly explained in the following section. Assume that the total length L of the track could be calculated by the following equation:

$$L = (2\pi R) \cdot VT \quad (49)$$

where the R is the radii to the track, the V is the velocity of the writing speed or conversion speed, and T is the time. Due to the infinite nature of the binary sequences, the whole pattern can be infinitely extended by spiraling. Therefore, the continuous nature of such an array allows the whole integrated nanostructures to tailor the specific sizes at the surface (i.e., x - y plane) for different applications. Take a nanostructured solar cell as an example, assume a customer needs a 200W output solar device. If each square inch solar device provides 50W, $\pi R^2=4$ square inches would be enough to generate the output power. Then, the total length L of the track is calculated based on the requirements, and the length of the binary sequence can be determined and extended without interrupting the property of the nanostructures. It enables us to precisely control the size of the nanostructures so that we can modify and extend the nanostructure size as needed. Finally, each

binary element (i.e., 1 or 0) in the binary matrix is represented in the 2D geometry by a unit square (1s→pits, 0s→lands).

4.2.3 Transferring designed 2D QRN pattern using an optical driver

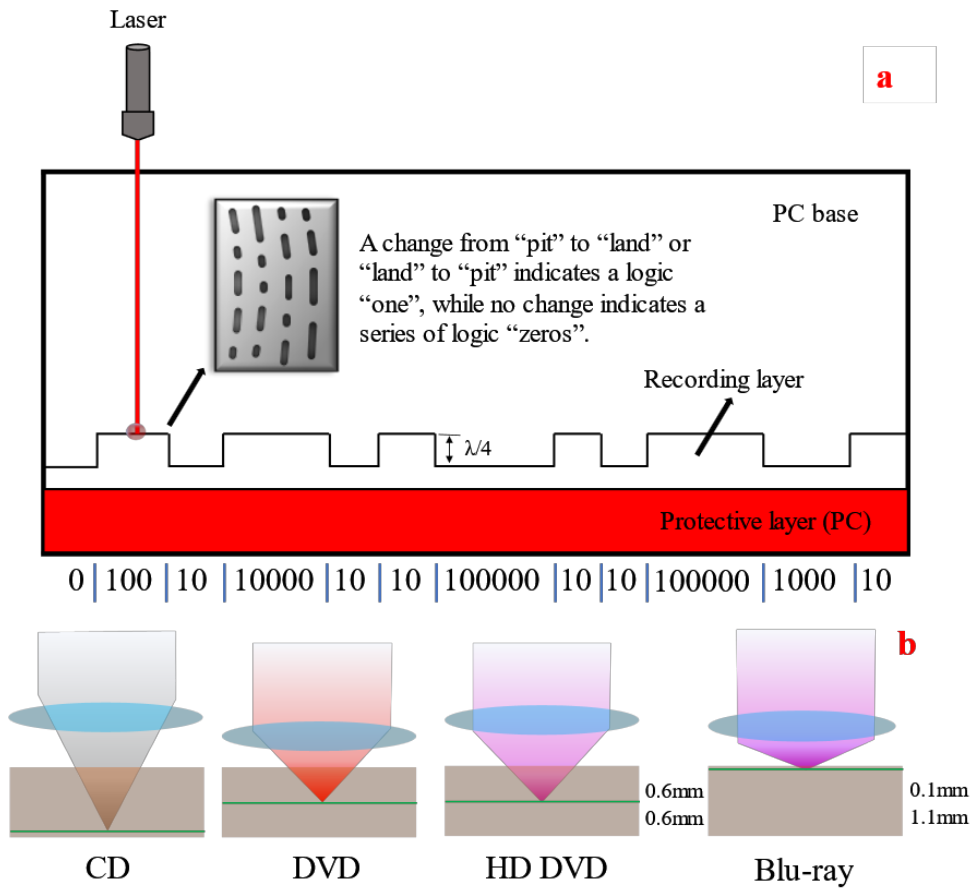


Fig. 4.2-2 (a) Layer structure of an optical disc; (b) schematics of the optical disc structure with different lasers for different optical discs (CD, DVD, HD DVD, and Blu-ray).

An optical driver is used to transfer our proposed 2D Fibo QRN pattern to a real mold for future ARC fabrication. The optical drivers are the standard equipment of personal computers used to write and read digital information on the discs. Briefly, during the writing process, the diode laser is directed by a polarizing beam splitter, which rotates the polarization plane of the laser beam. As a result, the light beam is collimated, creating a parallel beam. The parallel beam through an objective lens is focused onto the data track in the disc to write the “lands” and “pits” based on the pre-stored programmed digital information (see **Fig. 4.2-2**)^{71,72}. The laser beam scans the disc’s surface in a spiral pattern from the center to the outer as the optical disc counter-clockwise rotates.

4.2.4 HLTSC mold fabrication using optical disc technology

The optical discs, like CDs, DVDs, and Blu-rays, were developed for high-density data storage. Following optic disc industry standards, our designed binary Fibonacci sequence was 1:1 converted to precise nanoscale pits and lands with lengths from 150 nm to 800 nm. The nanomanufacturing method in this CHAPTER makes use of the stamps derived from the optical media discs in order to nanoimprint the designed 2D patterns contained within the recording layer of the optical media discs onto ARCs. Because the optical disc was designed for the continuous binary data reading with relatively few random seeks, and its data track forms an Archimedean Spiral Arrangement. This unique feature perfectly matches to our proposed QRNs. Therefore, the generated 2D QRNs are naturally distributed along the Archimedean spiral data tracks (see **Fig. 4.2-1 (a) – (b)**). Moreover, different optical media disc formats (e.g., CDs, DVDs, and Blu-rays) also offer an efficient way to tune the QRNs to achieve the desired effects for different applications by adjusting the pit sizes of the QRNs, which almost covers the whole wavelengths of the visible light (see **Fig. 4.2-2 (b)**). The specification data is shown in *Table 1*: (1) track pitch: 320 nm, 740

nm, 1600 nm; (2) minimum pit length: 150 nm, 440 nm, 830 nm; (3) pit width: 130 nm, 320 nm, 600 nm, from Blu-ray, DVD to CD, respectively.

The delaminated Blu-rays (Vinpover Digital Company) are used as the substrate for the nanopatterned molds. These coded Blu-rays were clipped from the middle and preheated in the water bath (Poly Science Company) at a temperature of 50°C for 30 mins. After that, the Blu-rays were dried up by compressed air and trimmed at the edges. The protective layer (reflective layer) should be gently peeled off. Then, the molds were trimmed again and cleaned in DI water by an ultrasonic cleaner for 480s. In the end, the Blu-ray molds (i.e., the polycarbonate recording layer) were ready to use after drying the mold.

Table 1 The specification of different optical storage disc formats

<i>Optical Storage Disc Formats</i>	<i>Track Pitch (nm)</i>	<i>Single Pit Length (nm)</i>	<i>Pit Width (nm)</i>
<i>CD</i>	1600	800	600
<i>DVD</i>	740	400	320
<i>BD(Blu-ray)</i>	320	150	130

4.25 HLTSC enhanced solar cell manufacturing

In this work, the coatings were directly fabricated on the thin-film solar cell devices using the nano-imprinting method, as schematically shown in **Fig. 4.2-3**. Based on the experiments and calculations, it was found that 5 grams of SYLGARD 184 silicone elastomer curing agent and 50 grams of SYLGARD 184 silicone elastomer base (1:10 ratio) would be good enough to generate

a 0.75mm thick PDMS (polydimethylsiloxane) coating on the solar cell devices, which provided us with the best conditions in the test. The base and curing agent are thoroughly mixed for 5 minutes by hand stirring or using a magnetic stirrer. Then, the mixed solution was placed into a vacuum chamber (Bel-Art vacuum chamber) and a vacuum pump was turned on (Gast Doap 704aa compressor vacuum pump 18 HP 115 Vac) for 30 mins. Afterward, the pump was turned off, and the vacuum chamber valve was slowly pulled out to let the air in. By repeating this step, all bubbles would be finally removed from the solution. After that, the solar cell device was placed into the petri-dish and attached to it using Scotch tape, and then the treated mixture was drop-cast over the device gently. After that, the dish was put back into the vacuum chamber, and the pump was turned on again since it would have a mass of bubbles under the device. Transfer pipettes were used to eliminate the trapped tiny bubbles in the solution. The dish was taken out and pre-heated in a Mini Incubator (Bio-Rad Company) for 10 mins at a temperature of 80°C. The solution will be stickier after pre-heating. Then a mold with the nanopatterned side facing down was laid onto the mixture. Eventually, the dish was put back into the incubator and cured it for at least 2 hours at the temperature of 80°C.

After two hours of baking, the whole PDMS coating layer was completely cured. Then, tweezers are used to peel off the DVD mold and trim the edges of the device carefully, Finally, the device with the PDMS nanopatterned coating layer could be ready for testing. Compared with the data from the experiments, it is found that the M-disc DVDs can be more effective at inverting the different structures than standard DVDs due to their rock-like layers, which are more stable than the dye layers of standard DVDs.

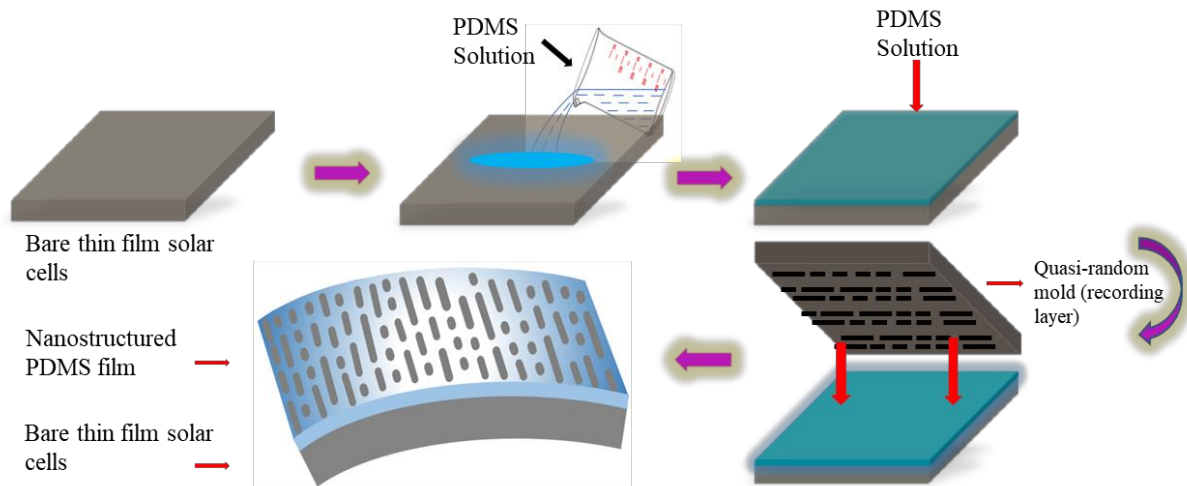


Fig. 4.2-3 Schematics of thin-film solar devices fabrication with HLTSC and its final device configuration.

4.3 Results and Discussion

Firstly, we computed the Fourier Transform Analysis (FTA) of the generated 2D HLTSC images to demonstrate the improvement of the power spectral density related to spatial frequency in **Fig. 4.31**, and the power spectral density illustrates that our HLTSC achieves a broader spectrum of energy compared to the bare and spiral only pattern. Then we numerically evaluated and verified the reflectance improvements by the commercial LUMERICAL FDTD software among bare thin-film solar cell, ASA only enhanced one, and the HLTSC one (see **Fig. 4.3-1 (a)**). The results clearly demonstrate the significant anti-reflection improvement at 550 nm, which is the critical region for light-to-electricity conversion in an a-Si:H thin-film solar cell. Although the thickness of ARC can not be ruled out for reflectance property, we concentrate the discussion on the patterned surface by fixing the thickness at 0.75mm. The changed reflectance behaviors are attributed to two possible explanations: 1) the reflectance behaviors are caused by the gradual refractive index profile from air to active layer; 2) the light path can be increased with an ARC

because of the scattering generated, multiple internal reflections, and redirection-assisted refracted light by an ARC.

A quantitative measurement is needed to evaluate light absorption over the entire solar spectrum. **Fig. 4.3-2 (a)** illustrates the current-voltage characteristics measured under AM 1.5G illumination from a solar simulator for the coated solar cell. For the sake of comparison, the grating nanostructures derived from a blank disc (i.e., grating spiral track without burning any data) were also fabricated and tested. As expected, the grating nanostructures beat the bare Si-based thin-film solar cell due to the spiral arrangement, and the Fibo QRNs outperformed the grating structure due to their local randomness caused by their “pits” and “lands” form. Our HLTSC yielded a relative 8.62% short-circuit current improvement and an 8.31% power conversion efficiency enhancement compared to bare solar cell. The difference in I_{sc} arises from the superior antireflection performance by gradual refractive index change related to the local randomness change.

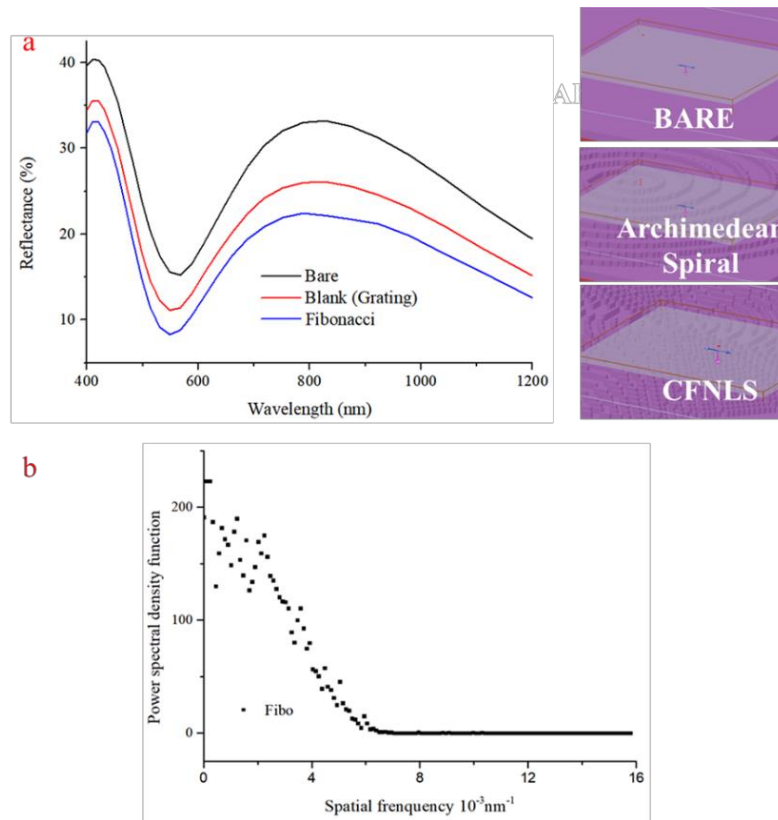


Fig. 4.3-1 Simulated reflectance of the thin-film solar cell with/without HLTSC and ASA Only as comparison; (b) Spatial frequency related Power spectral density of the 2D Fibo QRNs.

It is worth noting that over the time the angle of solar irradiation varies during a day. Therefore, the omnidirectional light-harvesting capability is important for a solar cell. According to Fresnel's law, the reflection often becomes more severe when the incident angle increases. Thus, it is critical to reduce the reflection loss at large incident angles to meet the requirements of practical application. According to the Lambert-Beer law⁷³, the derived equation becomes: $\eta(a) = 1 - \exp(-\alpha L)$, where $\eta(a)$ is absorption efficiency and α is the wavelength-dependent absorption coefficient. Therefore, a longer optical path length leads to more efficient light absorption.

Furthermore, the scattered light will propagate into the device in the same direction as the incidence, which also prolongs the optical path length. Under normal-direction light illumination, the optical path is related to the thickness of an active layer, which is $L=2n \cdot d$ (n is the refractive index of the active layer), while the scattered light leads to an optical path length of $L=2n \cdot d/\cos\theta$. For an increased θ , the resulting L can be many times longer than that of the normal incidence.

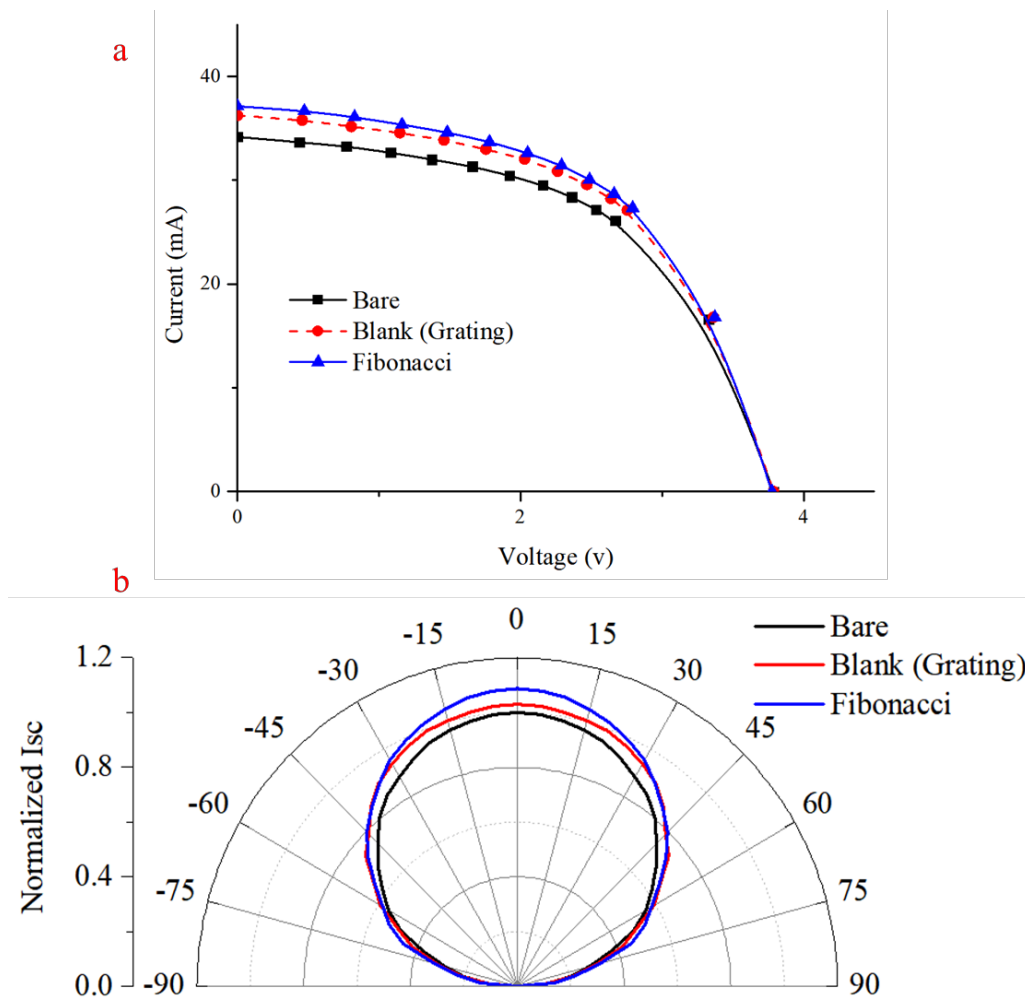


Fig. 4.3-2 (a) The I-V curves of a thin-film solar cell with HLTSC, ASA Only and without any coatings; (b) the angular dependence of a normalized photocurrent with HLTSC, ASA Only and without any coatings.

To validate the concept, the short-circuit current of a-Si:H solar devices with grating ARC and with/without HLTSC were measured for different angles of the light incidence, varying from 0° to 75° . **Fig. 4.3-2 (b)** indicates that a larger photocurrent improvement of over 10% was observed in a wide incident-angle range of $0^\circ\sim 75^\circ$, suggesting an omnidirectional distribution of redirected incident lights. Benefiting from our Fibonacci pattern with the Archimedean spiral arrangement design, the HLTSC on the a-Si:H device can present a 11% higher photocurrent than that of the flat reference device at 30° incident light (30 degree from the perpendicular incident light). The omnidirectional improvement in the conversion efficiency is significant for the practical deployment of solar panels without a tracking system.

4.4 Conclusions

In summary, an innovative hybrid 2D nanostructure design is proposed based on the merit characteristics of both Archimedean spiral and quasi-random nanostructures to achieve an outstanding light-trapping capacity. Optical technology and Fibo binary sequence enable us to fabricate “pits” and “lands” nanostructures along with an Archimedean spiral arrangement. With our well-designed nanostructured ARC, the efficiency improvement of the solar cell devices is up to 8.31%. Meanwhile, the reflectance on the surface is tremendously reduced by 11.62% compared to bare solar cells at 550 nm. In addition, a larger photocurrent improvement of over 11% was observed in a wide incident-angle range of $0^\circ\sim 75^\circ$, suggesting an omnidirectional distribution of redirected incident lights. The results reveal that our hybrid nanostructure indicates great performance in light-trapping and has the potential to be a new alternative in the light-trapping scheme.

5 CHAPTER FIVE: 2D DISCREPANCY-ASSISTED DETERMINISTIC QUASI-RANDOM NANOSTRUCTURE DESIGN AND OPTIMIZATION

5.1 Introduction

Beyond the advances in material growth and device's multiple layer design, photon management on the nanoscale (e.g., surface decoration) provides a promising way to further improve the optical performance (e.g., PCE) of various types of optoelectronic devices, including light-emitting diodes, photovoltaics, and photodetectors^{74,75-78}. Balancing the advantages of both conventional periodic and random nanostructures, quasi-random nanostructures (QRNs) retain distinctive optical features, such as richer Fourier spectra for broadband optical performance. Quasi-random nanostructures (QRNs) are commonly found in nature with rising popularity due to their extraordinary functions, such as iridescent color in birds' feathers, and butterflies' wings (structural coloration) for camouflage and intimidation and the bright-white appearance of beetles^{62,74,79}.

The current design for QRNs can be classified into three categories, 1) topology optimization method, 2) descriptor-based method, and 3) correlation function⁸⁰. However, the difficulty of QRN designs is hard to tailor toward the desired path of light propagation due to their inherent non-deterministic properties. To be specific, topology optimization suffers from randomly testing thousands or even millions of design variables to achieve the desired optical performance. Because the topology optimization method uses real-space representation, and many variables need to be clarified to describe the complex geometries, which results in a modification obstacle in large-scale design and optimization. Moreover, it is necessary to build up the correlation between the structures' spatial distribution and their topology optimization. The descriptor-based method skillfully bypasses a large number of variables by employing an efficient indirect parametric

concept to optimize limited structure descriptors, such as filling ratio, volume fraction, and porosity. The third calculates the correlation between any two points in a structure to represent its uniformity/randomness by intensifying/weakening the oscillation. However, the second and third methods are less intuitive and may not be achievable in fabrication.

In this paper, we propose an innovative closed-loop methodology for deterministic 2D QRN design (see **Fig. 5.1-1 (a)**), optimization, and scalable fabrication based on two fundamental concepts: digitalization and star discrepancy (D_N^*). A quasi-random pattern (QRP) is a 2D projection of the QRNs since the heights of the QRNs are fixed to minimize structural complexity and ease fabrication. We first segment a 2D plane into a mesh matrix, wherein each element can be filled by either a “0” or a “1”, corresponding to a unit-size “land” or “pit” in a 2D plane. The binary assignment of each element (i.e., “0” or “1”) is derived from iteratively generated discrete quasi-random sequences (e.g., Thue-Morse (TM), Fibonacci (Fibo), Rudin-Shapiro (RS), etc.) and plots (e.g., Halton, etc.). By doing so, these generated binary matrices are directly converted into a deterministic 2D pattern over a mesh area with designed “lands” and “pits”. This one-to-one mapping process between patterns and matrices is named as the digitalization of a QRP. Meanwhile, it has been reported that the nanostructures’ spatial randomness (3D) is a key factor for optoelectronic devices’ light-trapping capability because those nanostructures with a higher degree of spatial randomness are more likely to randomize, re-direct, and prolong the light path⁸¹⁻⁸³. For a QRP, we focus on the surface randomness (2D) of the QRNs instead of the spatial randomness with the fixed nanostructure height. Therefore, we introduce the star discrepancy (D_N^*) to describe the surface randomness of each 2D QRP and run the corresponding finite-difference time-domain (FDTD) simulation and physical experiments to reveal the correlation between the QRNs’ optical performance and their surface randomness (represented by D_N^*), i.e., the QRN with

a higher D_N^* has a lower reflectance rate. Guided by this observation, we can therefore design a QRP or optimize the existing QRP to achieve a higher D_N^* to further improve the optical performance of an optoelectronic device. To prove this concept, we fabricated the anti-reflective coatings (ARCs) with well-designed QRN patterns onto the thin-film solar cells using optical disc technology, which employs stamps derived from the recording layer of a disc for nanoimprinting. The best ARC with RS QRNs realized broadband light-trapping with $> 13.58\%$ PCE enhancement over the commercial solar cells, while its 46th optimized iteration pattern reduced an average 20% of the reflectance over a broad wavelength range. The optical simulations and physical experiments confirm our approach and demonstrate the superior optical performance of QRNs over periodic and random nanostructures in broadband and omnidirectional light-trapping capabilities. The proposed systematic QRN design, optimization, and fabrication approach overcomes the aforementioned barriers with the following advantages, 1) the surface morphology of a QRN directly depends on the generation of a binary matrix instead of complicated and indirect physical variables (e.g., volume fraction, material filling ratio, etc.); 2) suitable binary matrices can be selected and optimized by evaluating their D_N^* values; 3) the generated binary matrices are easily converted into physical pit/land nanostructure via optical disc technology (see section 4.2).

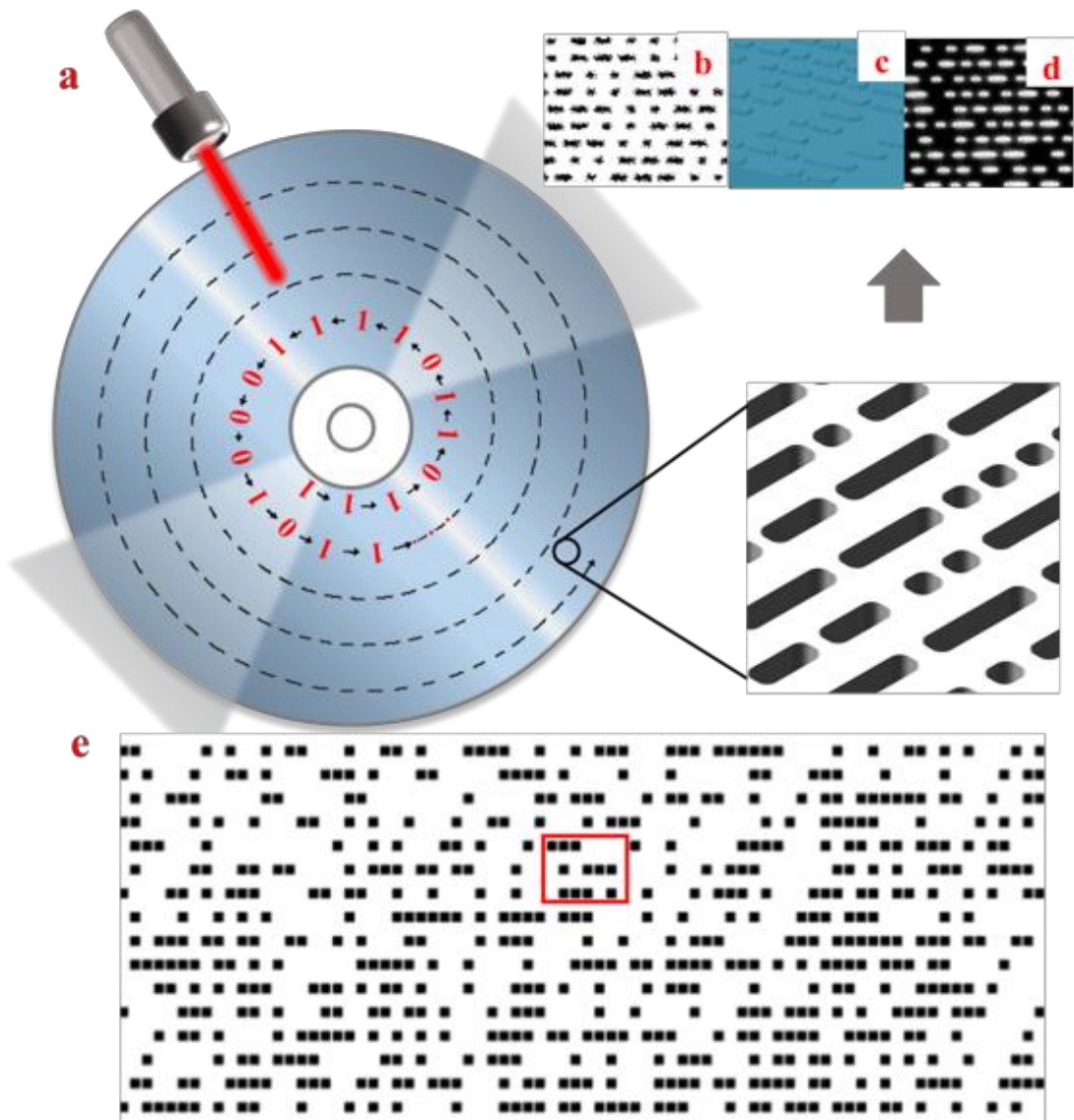


Fig. 5.1-1 (a) the schematic of a writable disc and its recording layer; (b) a generated edge blurred QRP design based on binary RS sequence with MATLAB; (c) a simulated QRN image on Lumerical FDTD software; (d) the SEM image of the fabricated QRNs derived from the optical recording layer; (e) illustration of a 2D QRP generated by binary RS sequence.

5.2 Method

5.2.1 Binary quasi-random sequences generation

- *Fibonacci*: The generation of the binary Fibonacci sequence can be found in CHAPTER FOUR and will not be further explained in this CHAPTER.
- *Rudin-Shapiro*: Another well-known quasi-random deterministic system whose Fourier spectra are continuous and even constant is the Rudin-Shapiro structure (RS). The Rudin-Shapiro sequence is typically generated using a four-letter substitution rule to induce the new generation from the old one^{84,85},

$$A \rightarrow AB, B \rightarrow AC, C \rightarrow DB, D \rightarrow DC \quad (50)$$

Beginning with the letter A (Initial character), the first four generations are:

$$A \rightarrow AB \rightarrow ABAC \rightarrow ABACABDB \rightarrow ABACABDBABACDCAC \dots \quad (51)$$

By substituting each “ A ” and “ B ” with “1” and each “ C ” and “ D ” with “0”, we can have a RS sequence in four letter form transformed to a binary sequence. By doing so, the substituted equation becomes:

$$1 \rightarrow 11 \rightarrow 1110 \rightarrow 11101101 \rightarrow 1110110111100010 \dots \quad (52)$$

- *Thue-Morse*: There are even more complex deterministic quasi-random structures, possessing singular continuous Fourier spectra, such as the Thue-Morse system^{86,87}. In mathematics, the Thue-Morse sequence is considered to be the prototype of a substitutional aperiodic symbolic map. It has been shown that the Thue-Morse patterns can give rise to coherent multiple wave scattering. The infinite product comes with:

$$\prod_{i=0}^{\infty} (1 - x^{2^i}) = \sum_{j=0}^{\infty} (-1)^{t_j} x_j \quad (53)$$

where t_j is the j th element if we start at $j = 0$.

Here, we will generate the Thue-Morse pattern by the simple inflation rule:

$$1 \rightarrow 10, 0 \rightarrow 01 \quad (54)$$

The Thue-Morse sequence goes on like:

$$1 \rightarrow 10 \rightarrow 1001 \rightarrow 10010110 \rightarrow 1001011001101001 \dots \quad (55)$$

- *Halton*: A 2D Halton pattern is introduced by applying two different generation rules along the horizontal and the vertical directions based on different co-prime numbers, alternatively⁸⁸. To generate 2D Halton quasi-random patterns, we first generate the sequence on prime “2” by dividing the interval (0,1) in half, which gives us:

$$\frac{1}{2}, \frac{1}{4}, \frac{3}{4}, \frac{1}{8}, \frac{5}{8}, \frac{3}{8}, \frac{7}{8}, \frac{1}{16}, \frac{9}{16}, \dots \quad (56)$$

Equivalently, generating the sequence on prime “3” gives us:

$$\frac{1}{3}, \frac{2}{3}, \frac{1}{9}, \frac{4}{9}, \frac{7}{9}, \frac{2}{9}, \frac{5}{9}, \frac{8}{9}, \frac{1}{27}, \dots \quad (57)$$

When we pair them up, we get a sequence of points in a unit square. By doing so, the star discrepancy appears a converged tendency with increased point number. This method provides us a way to avoid the clumping and gapping in the pattern formed by 1D sequences.

5.2.2 Different 2D QRP design

For any binary 2D pattern, we can always use rectangle unit building blocks that are small enough to digitize the entire 2D pattern and map it to an m -row-by- n -column binary matrix, like a digital image in pixels. In other words, each unit building block in a 2D nanostructure pattern stands for either a “pit” (i.e., “1” or a black building block in a 2D matrix pattern) or a “land” (i.e., “0” or a white building block in a 2D matrix pattern), and its position in the matrix is defined by a pair of integer tuple (x, y) as its coordinate, where $1 \leq x \leq m, 1 \leq y \leq m$ (see **Fig. 5.1-1 (c)** and **(d)**). In doing so, we establish a one-to-one mapping between a real 2D pattern and a matrix where each individual element can be programmed to achieve the exact desired 2D pattern. Based on this concept, we introduce three approaches to develop the desired binary 2D QRPs for light manipulations, namely: 1) converting 1D binary sequences to 2D QRPs; 2) directly generating 2D QRPs; and 3) digitalizing the existing 2D QRPs in other forms (e.g., channel and particle forms).

Converting 1D binary sequences to 2D QRPs: Since profound connections are observed between substitutional sequences and their optical properties on the spatial correlations, multiple widely used substitutional binary sequences (e.g., Fibo, TM, RS) are selected to generate 2D QRPs. Each binary element (i.e., 1 or 0) in the sequence is presented by a unit square ($1 \rightarrow$ pit, $0 \rightarrow$ land) in the 2D geometry, and the entire binary sequence is mapped to the 2D space in the shape of an Archimedes spiral arrangement, which is commonly found in nature (e.g., sunflowers) due to its superior light capture capability. By doing so, since the binary substitutional sequence can be infinitely extended, a scalable binary 2D pattern is created, and its property of QRNs is examined and explained following the definition in the next section.

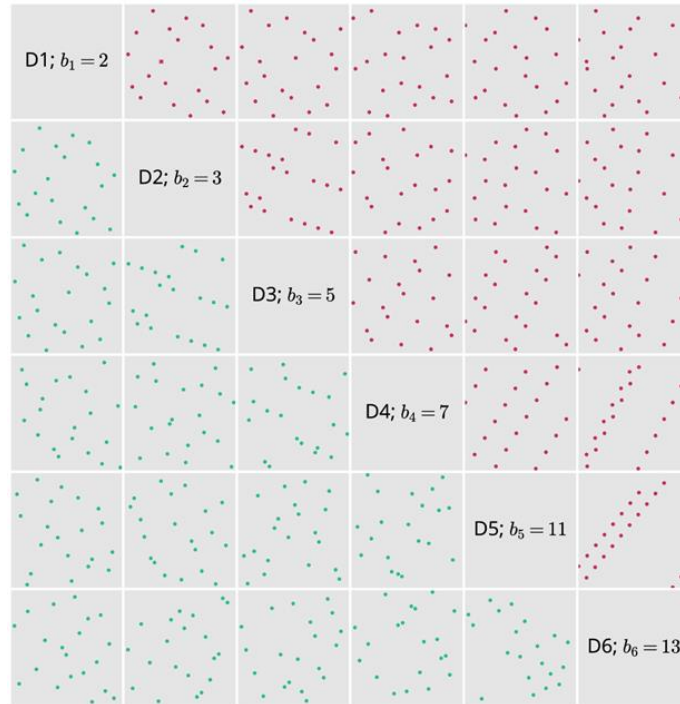


Fig. 5.2-1 Two-dimensional Halton sequences generated from combination of primes from dimension 2 to dimension 13; the red part is formed by 1D standard Halton sequence, and the green part is formed by optimized sequence.

To be noticed, some converted 1D sequences do not exhibit quasi-random structure properties in high dimensions, such as the Halton sequence, the Sobol sequence and the d-dimensional Kronecker sequence⁸⁹. These sequences use different coprime numbers (≥ 2) or bases in each dimension to fill space to get a highly uniform property. Due to the curse of dimensionality, such sequences still suffer from the correlation problem as manifested in higher dimensional projections due to the bad quality of multi-dimensional coverage. These correlations cause the Halton sequence to have poor two-dimensional projection for some coprime numbers. For example, for primes “11” and “13”, the first 8 of generated points would have perfect linear correlation (see **Fig.**

5.2-1)⁹⁰. Therefore, coprime numbers “2” and “3” are determined to avoid the correlation problem generated by higher primes.

Direct 2D QRP generation: The 2D lattice method can also be employed to directly assign 1s/pits and 0s/lands to each unit square in the 2D pattern according to their coordinates (x, y) . For instance, a 2D Halton pattern can be achieved by first generating two decimal Halton sequences/vectors, $x = \{x_1, x_2, \dots, x_i\}$ and $y = \{y_1, y_2, \dots, y_i\}$, with two co-prime numbers, and then assigning 1s/pits for each (x_i, y_i) , $i = 1, 2, \dots, i$ and leaving the rest units to be 0s/lands. The generation rule guarantees that any 2D Halton pattern is a QRP.

Digitalizing existing 2D QRP in other forms: Principally, all 2D patterns, including popular channel and particle types of QRPs, can be projected onto digital greyscale photos/images of various resolutions. Using the finite element method, each pixel on the photo can directly represent either as a single black (i.e., $0 \rightarrow$ land) or a white (i.e., $1 \rightarrow$ pit) unit square block by enhancing the contrast and other image processing technologies. Doing so provides an efficient method to reconstruct and further optimize the existing 2D QRPs without relying on specific physical intuition (e.g., filling ratio, volume fraction, etc.) as other methods do.

5.3 Theory

5.3.1 Discrepancy-assisted QRP design reaching desired surface randomness

Since QRPs are in somewhere between a perfect order and a complete random pattern array, various concepts have been proposed, including SDF or two-point correlation, to design and tailor the QRPs for optimal optical performance, yet most of them usually lack a connection between QRP design and structure descriptors⁹¹⁻⁹³. Fortunately, it has been reported that the different degrees of surface randomness can contribute to the enhancement of the light-trapping capacity

caused by their irregular surfaces. Therefore, the evaluation of a surface's randomness emerges as an alternative guidance to assist the QRPs design. The main geometrical factors for evaluating the effect of surface randomness are nanostructure features (e.g., depth/height, shapes, pitch sizes, etc.) and spatial arrangement. For convenience, the nanostructure feature and depth (height) are fixed (as pitch size of 400 nm and height of 120 nm) and beyond the scope of this paper, and we focus on the effect of the nanostructure arrangement on surface randomness. Thus, the geometric discrepancy of a 2D surface is imposed to calculate its uniformity, which has a negative correlation to randomness and is expected to assess its surface randomness and related optical performance. By doing so, we bridge the connection between the complicated physical nanostructure model and a simple mathematical computational model to prevent us from tweaking dozens of design variables (e.g., filling ratio, pitch sizes, and depth) associated with higher dimensionality (≥ 2 dimensions) for simulations and experiments.

Without loss of generality, in a d -dimension finite even-distributed binary mesh space $I^d \in [0,1]^d$, where each unit is occupied by either 1 or 0, if there are N units of 1s (i.e., $X = \{x_0, x_1, \dots, x_{N-1}\}$) and the rest are all 0s, the discrepancy of a rectangular sub-space J in I^d is defined as Eq. (58)^{89,94,95}:

$$D_N(J) = \mu_x(J) - \mu(J) \quad (58)$$

where J represents a subset in I^d , $\mu_x(J) = (\text{The number of points in } J)/(\text{Total points, i.e., } N) \in [0,1]$, and $\mu(J) \in [0, 1]$ is the Lebesgue Measure of J . In other words, $\mu(J)$ is the fraction of X in J over I^d , while $\mu(J)$ is the fraction of J over I^d . For I^d of $d=1, 2, 3$, $\mu(J)$ turns out to be the fraction of length, area, and volume, respectively. The dimension of space is limited as “2” in the scope of

this paper. Generally, the larger discrepancy in 2D area indicates more random (i.e., less uniform) distribution of a set of points over the area, and vice versa.

$$\prod_{i=0}^d [a_i, b_i], 0 \leq a_i < b_i < 1 \quad (59)$$

Applying this concept to the 2D QRP designs described in the last section that the 2D binary mesh space segmented into unit square boxes, each box is painted into black if it is assigned “1”, and white otherwise (see **Fig. 5.1-1 (e)**). Therefore, the discrepancy becomes:

$$D_N = \left| \frac{\text{Number of black boxes in } J}{\text{Total black boxes}} - \frac{A}{B} \right| \quad (60)$$

where A is the area of J , and B is the area of total boxes in I^2 . An example of Eq. (60) is illustrated in **Fig. 5.1-1 (e)** where I^2 contains 31×78 unit squares in total and 581 black ones, while a subset J (i.e., the red rectangle) has 11 black boxes in total of 5×7 squares. Thus, the discrepancy of J becomes $D_N = \left| \frac{11}{581} - \frac{5 \times 7}{31 \times 78} \right| \approx 4.45 \times 10^{-3}$. Because this is just one single case for the discrepancy of this particular J , which cannot simply represent the discrepancy (i.e., the degree of randomness) of the entire space.

Being more trackable than the varied values of discrepancies for all subsets J in I^2 , the maximal deviation of all possible discrepancies, the star discrepancy (D_N^* , Eq. (61)), is employed as a criterion to evaluate the degree of surface randomness of the pattern morphology⁹⁶.

$$D_N^* = \text{Sup}_{J \in I} |D_N(J)| \quad (61)$$

The computation results (Section 4) show that a pattern with more randomness (i.e., less uniformity) has a higher D_N^* . **Fig. 5.3-1(a)** and **(b)** show two different degrees of surface randomness for two patterns with the different D_N^* . More importantly, a pattern is quasi-random if:

$$D_N^* \leq c \frac{(\log N)^2}{N} \quad (62)$$

where c is a constant coefficient, and N is the total number of 1s in the matrix (i.e., pits in this paper). Eq. (62) not only enables us to determine whether the pattern is a QRP, but also helps maintain the “quasi-random” property when the pattern is tailored to be more “random” for promoted light-trapping capability.



Fig. 5.3-1 (a) simulated quasi-random structures with low discrepancy value (more uniform); b) simulated pseudo-random structures with high discrepancy value (more random).

5.3.2 The relationship between the discrepancy and optical performance for QRPs

The star discrepancies of various 2D patterns with increasing pattern size scale are examined and plotted (**Fig. 5.3-2 (a)**). Three 2D QRPs are generated based on corresponding 1D binary sequences (i.e., RS, Fibo, TM) and the fourth (i.e., Halton (2,3)) is generated directly by assigning binary values to each unit building block in the mesh space. The size of each 2D pattern increases from 500-unit building blocks to 4000-unit building blocks in each dimension (x and y axis). Detailed D_N^* values for each size are listed in *Table 2*.

*Table 2 The star discrepancy calculation of the different quasi-random patterns based on the area R^2 (500*500~5000*5000)*

Unit	Sequence			
	RS	Fibo	TM	Halton (2,3)
500	3.08×10^{-3}	2.92×10^{-4}	2.79×10^{-4}	3.51×10^{-3}
1000	1.98×10^{-3}	9.47×10^{-5}	1.04×10^{-4}	1.96×10^{-3}
1500	1.17×10^{-3}	5.33×10^{-5}	6.58×10^{-5}	1.17×10^{-3}
2000	8.31×10^{-4}	3.60×10^{-5}	4.70×10^{-5}	8.73×10^{-3}
2500	5.84×10^{-4}	2.59×10^{-5}	3.17×10^{-5}	6.75×10^{-4}
3000	4.93×10^{-4}	2.22×10^{-5}	2.58×10^{-5}	5.88×10^{-4}
3500	4.34×10^{-4}	1.63×10^{-5}	1.94×10^{-5}	4.92×10^{-4}
4000	4.53×10^{-4}	1.41×10^{-5}	1.75×10^{-5}	4.87×10^{-4}

Fig. 5.3-2 (a) indicates that 1) all four fitting curves of D_N^* over P approximately obey Eq. (62), confirming that 1) these patterns are quasi-random; and 2) the order of surface randomness (i.e., discrepancy) among these patterns remain unchanged as the pattern size scales up (i.e., $\text{Halton}(2,3) \approx \text{RS} > \text{TM} > \text{Fibo}$), implying that computing D_N^* in small scale can cover the large scale scenario, reducing the computational complexity. In comparison, a pseudo-random pattern may have an unpredictable tendency of D_N^* over pattern size, and it indicates that if the discrepancy value curve of a pattern can not fit into the Eq. (62), the pattern does not have a quasi-random property. It can also explain why 2D Halton QRP can not be designed using a 1D converted binary sequence. **Fig. 5.3-2 (c)** shows the 1D Halton (2,3) sequence is converted to 2D QRP by spiral arrangement. The tendency with increased pattern size and N points (i.e., 1s) does not show the convergency, which means the re-shaped 2D pattern does not have QRP properties.

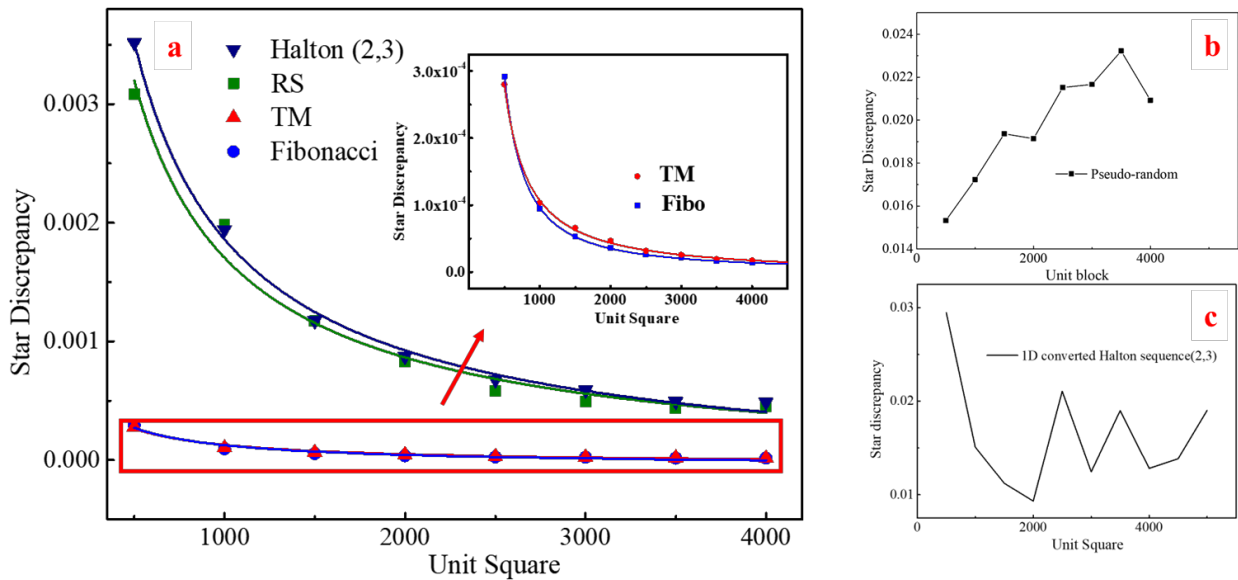


Fig. 5.3-2 (a) The relationship between star discrepancy and pattern scale on different QRPs (i.e., RS, TM, Fibo, Halton (2,3)); (b) The tendency of the star discrepancy with increased unit square based on the pseudo-random pattern; (c) The tendency of the star discrepancy with increased unit square based on 1D Halton (2,3) sequence.

5.4 Results and Discussion

5.4.1 The relationship between the discrepancy and optical performance for QRPs

To investigate how D_N^* is related to the optical performance, a numerical analysis of the electromagnetic field features is performed using the FDTD method. 3D schematic models of each QRN are established with a Si-based solar cell sandwiched by a nanostructured ARC and a silver reflector. Each QRN of 500×500 -unit building blocks is simulated over an $11 \mu m \times 11 \mu m$ area with perfectly matched layers (PML), and the mesh resolution is configured as $0.01 \mu m$. The reflectance is calculated through the field monitor located above the plane wave source (**Fig. 5.4-1**). The results show that the reflectance of the four QRP nanostructures coated on the Si-based solar devices follows the order: Halton (2,3) \approx RS $<$ TM $<$ Fibo in the almost entire visible light spectrum, opposite to the relationship presented in D_N^* (**Fig. 5.3-2 (a)**), revealing that a higher degree of randomness improves the antireflection capability in wavelengths of 500 nm \sim 900 nm. It also presents an enhancement of 2D QRN coated Si-based solar cells in a broader spectral range, rather than the distinct power peaks observed in periodic nanostructures.

To double/cross-check the FDTD optical simulation of the four QRPs, SDF can be performed to fast validate the results. Traditionally, spectral density function (SDF) is employed to evaluate and reconstruct the optical and morphological characteristics for various nanostructures^{91,92}. However, it may not be the optimal approach to modify the surface morphologies for better light-trapping capacity due to the unpredictable SDF distortion and defects caused by the discrete pixels in the finite element meshing in the SDF-to-spatial arrangement distribution calculations. **Fig. 5.4-3** illustrates the corresponding 2D patterns, Fourier Transforms Analysis (FTA) and SDFs of each QRP and confirms that Halton (2,3) and RS QRNs achieve a broader spectrum of energy with a

higher degree of randomness in comparison to the other two QRPs. In other words, the SDF results agree well with our FDTD simulations.

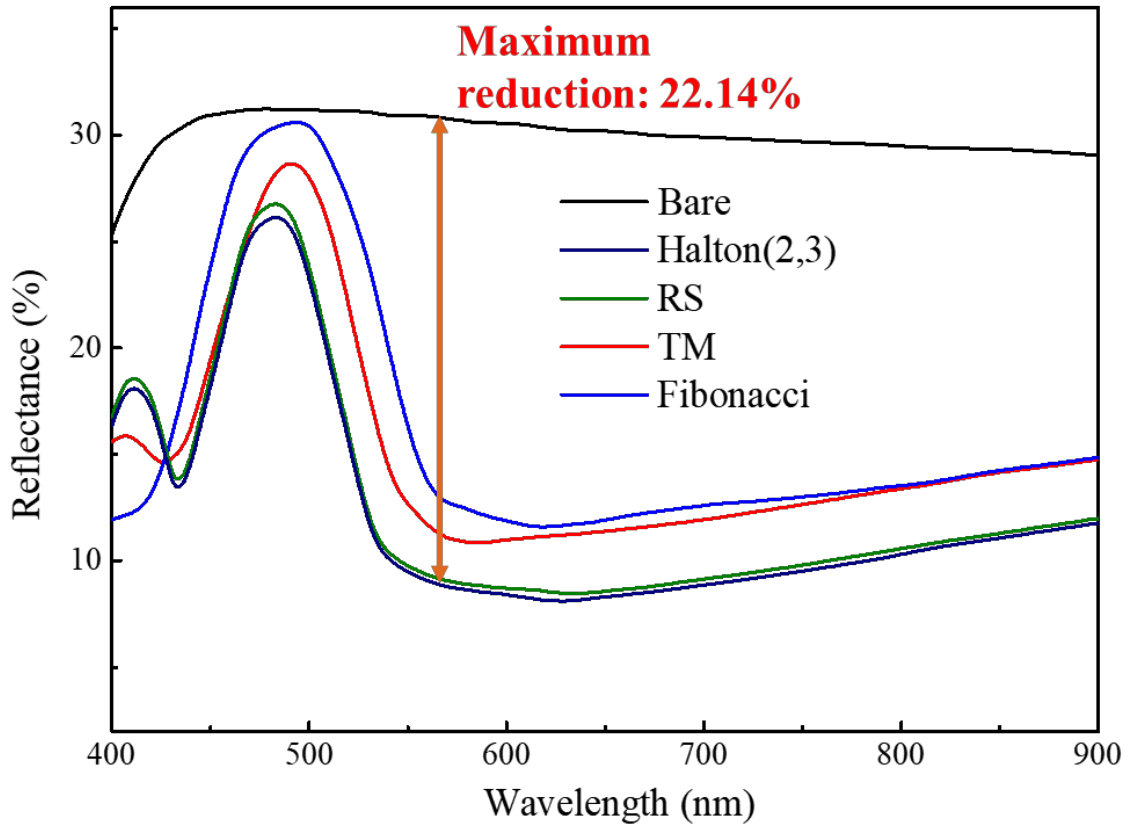


Fig. 5.4-1 The reflectance of a thin-film solar cell (Si-based) with different QRN coatings by Lumerical FDTD simulations.

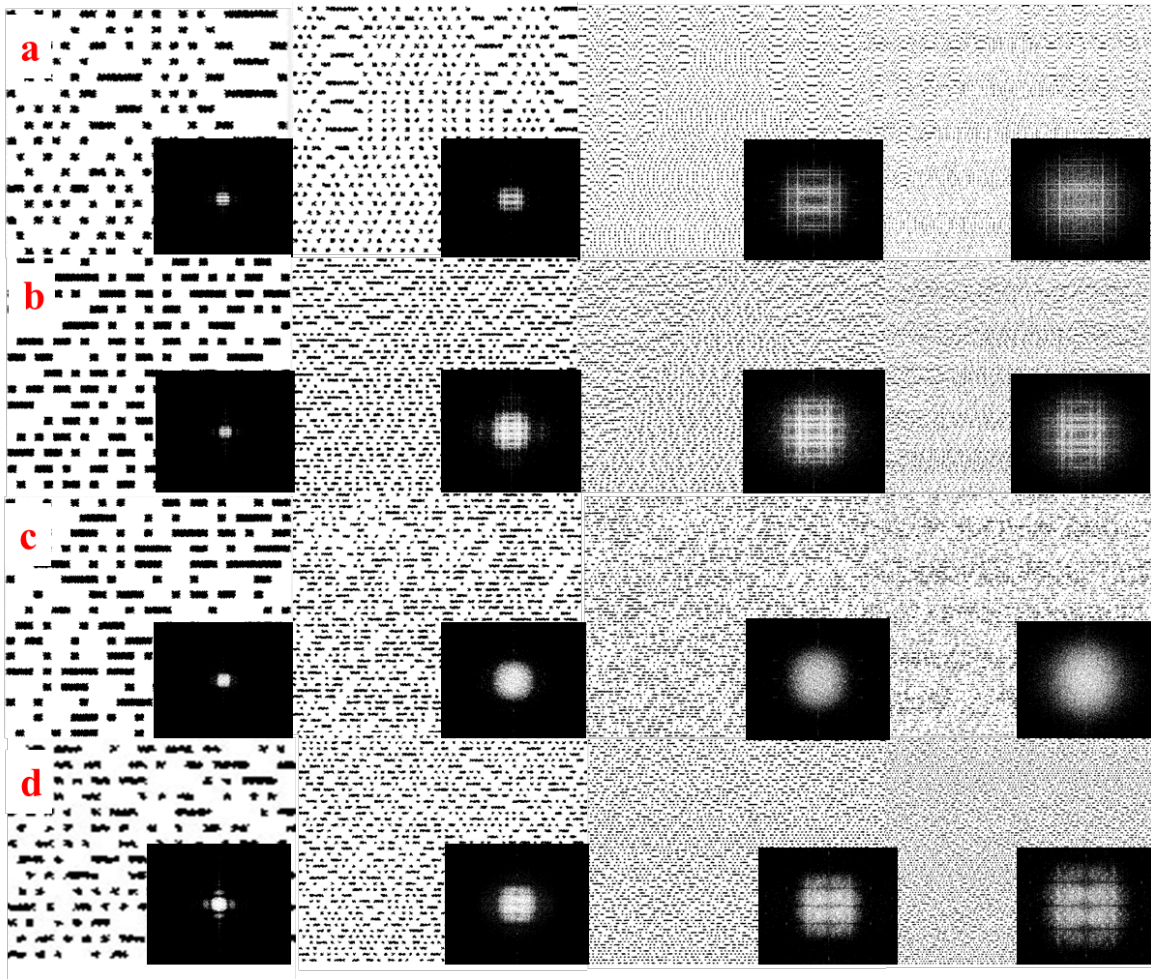


Fig. 5.4-2 Fast Fourier transform from 30 unit* 30 unit to 300 unit* 300-unit (a) Fibonacci; (b) Thue-Morse; (c) Rudin-Shapiro; (d) Halton (2,3) with 0.5 filling ratio.

To be noticed, the FTA is determined by the distribution of the Fourier components (e.g., the effect of its shape and position). With increased pattern size, the appearance of FTA maintains the same but the size changes, which indicates that our QRPs remain their properties with the pattern size increased due to the same spiral arrangement (see **Fig. 5.4-2**).

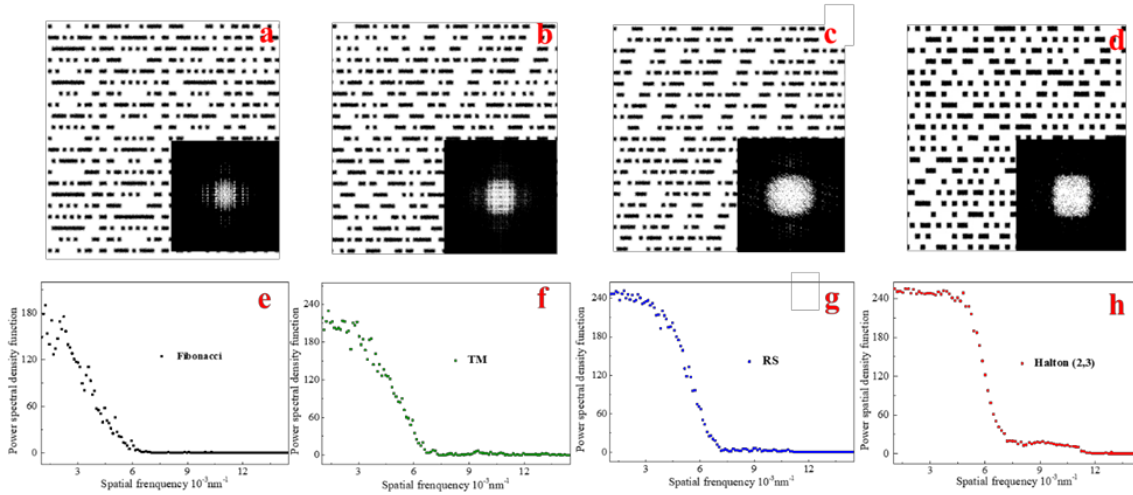


Fig. 5.4-3 (a)-(d) Different quasi-random patterns and their Fourier Transform Analysis; (a) Fibonacci sequence; (b) Thue-Morse sequence; (c) Rudin-Shapiro sequence; (d) Halton (2,3) sequence. (e)-(h) Comparison of spectral power density functions for representing quasi-random structures.

5.4.2 The comparison of fabricated QRNs and simulated QRNs and its schematic fabrication process

As a proof of concept, our technology could perfectly fabricate the well-designed quasi-random sequences into a real-space nanostructure. To quantitatively characterize the QRNs, the different QRN ARCs were fabricated on the various thin-film solar cell devices using the optical disc technology-based soft-lithography method, as schematically shown in **Fig. 5.4-4 (a)**. The detailed ARC fabrication processes are explained in section 4.2. In doing so, we characterized the quasi-random nanostructures derived from PDMS coatings by FTA of the SEM images. **Fig. 5.4-4 (b) - (i)** shows the SEM images from different nanostructures derived from the recording layers and the simulated nanostructures derived from mathematical algorithms. The SEM images indicate that our quasi-random nanostructures comprise a plurality of “pits” and “lands” arranged in a

plurality of tracks. Here, we use the theory from Dr. Huang's group to calculate the k-value based on different photoactive and electrode materials⁶⁸. In this work, the photoactive material is chosen as a-Si:H, and the electrodes are made of Ag. The circles from the inner (solid green, smallest k-value) to the outer (dash red, biggest k-value) denote the solar spectrum wavelength range from 315nm to 2.5 μ m coupling with the k-values. Besides this, **Fig. 5.4-4 (b) – (i)** also shows the FTA of our fabricated QRNs is similar to our simulated QRNs, which indicates that the fabricated nanopatterns are like those predicted computationally.

5.4.3 Effect of the different surface randomness for photocurrent generation

In addition to the FDTD simulation and verification, we measure our designed 2D QRNs' photocurrent generational capability. To illustrate, we burn the QRP matrix onto a blank writable optical disc and generate "pits" and "lands" on the disk recording layer as the building blocks to create QRNs.

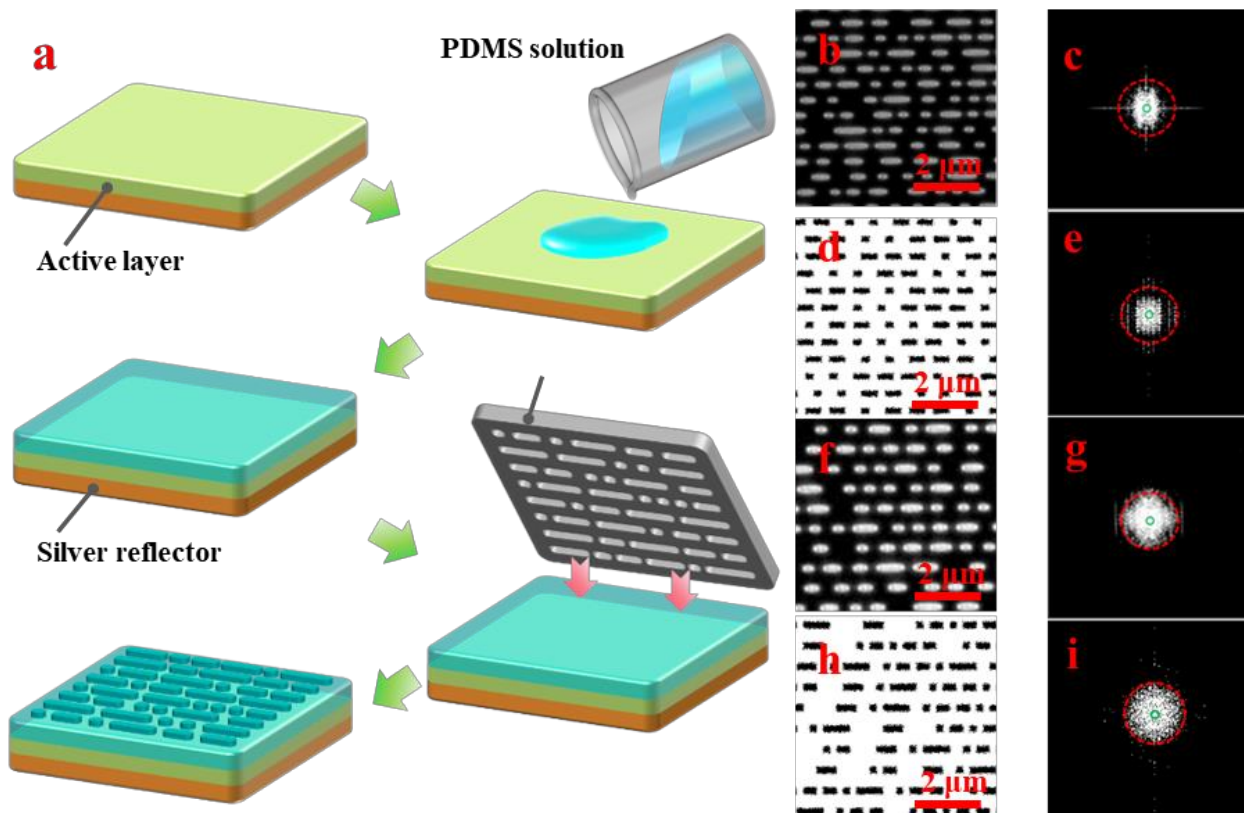


Fig. 5.4-4 (a) Schematics of thin-film CIGS fabrication and final device configuration; (b)-(e) SEM and simulated image of the Fibo quasi-random nanostructures and their Fourier Transform Analysis; (f)-(i) SEM and simulated image of the RS quasi-random nanostructures and their Fourier Transform Analysis.

The light absorption of various nanostructures over the entire solar spectrum is evaluated by measuring the current-voltage characteristics under AM 1.5G illumination (see Fig. 5.4-5 (c)). The enhancement in absorption is interpreted by an increase in short-circuit current (I_{sc}) from a bare module (34.178 mA) to the solar device with RS QRNs (38.816 mA), a maximum of 13.57% improvement on photon-to-electricity efficiency. Multiple factors contribute to this improvement:

1) the nanostructured ARC forms a gradient refractive index $\eta_{Ag} > \eta_{a-Si:H} > \eta_{PDMS} >$

$\eta_{PDMS-RS} > \eta_{air}$ (Fig. 5.4-5 (b)); 2) the QRN induces the Mie-scattering phenomenon, which normally takes place in the spectral range close to the multiple of the pit length and generates a strong forward scattering (i.e., the same direction as the incident light); 3) the gradient I_{sc} improvements between each QRP are matched to their increased degrees of surface randomness.

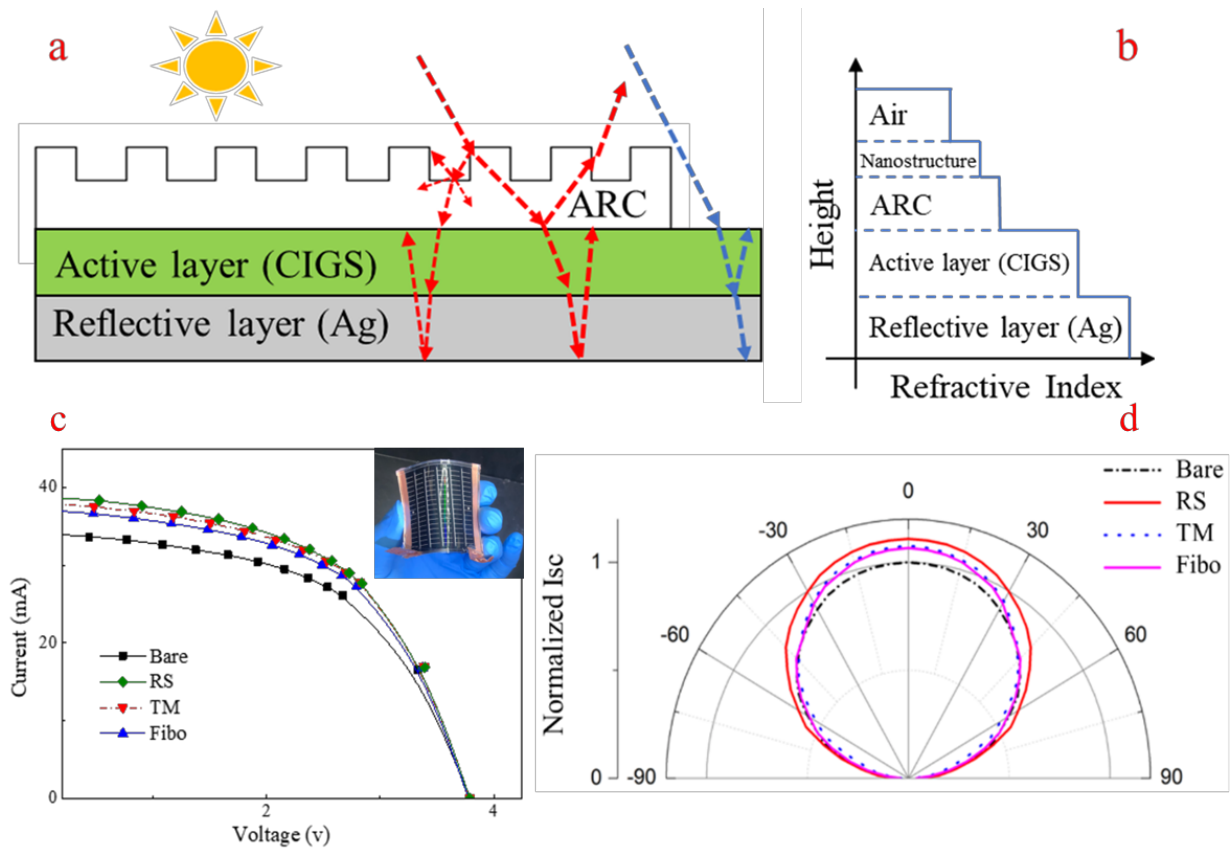


Fig. 5.4-5 (a) Schematic illustration of light behavior for solar device with/without nanostructured coating; (b) the relationship between height position and material refractive index; (c) the I-V curve of a thin-film solar cell (a-Si:H) with the different nanostructured coatings (RS, TM, Fibo) and without (solid black line) any coatings; (d) the angular dependence of a normalized photocurrent with/without the nanostructured coatings.

Since the angle of solar irradiation affects the optical loss by Fresnel's law, we also examine the omnidirectional light-harvesting capability. For an increased incident angle θ , the path of the propagated light from outside to inside will be changed, and the efficiency of the solar devices will be enhanced by optical redirection-assisted light-trapping (**Fig. 5.4-5 (a)**). Therefore, the I_{sc} of the Si-based devices with and without ARC was measured for different angles of the light incidence varying from $0^\circ \sim 75^\circ$. **Fig. 5.4-5 (d)** indicates an average of 10% photocurrent (up to $\sim 12\%$) is observed for the Si-based solar cell coated with RS QRN in a wide incident-angle range of $0^\circ \sim 75^\circ$, suggesting an omnidirectional distribution of redirected incident light. The working principle of QRNs under AOI can be further discussed. When the incident light is not perpendicular, the degree of surface randomness not only randomizes the angle of reflection, but it also impacts the angle of refraction and results in optical path enhancement of light as light travels a longer distance in a semiconductor. It is thus of importance to reduce the reflection loss at large incident angles to meet the requirements of practical application.

Table 3 Solar cell performance. I_{sc} , V_{oc} and corresponding enhancement of a-Si:H thin-film solar devices

Sample	I_{sc} (mA)	V_{oc} (v)	I_{sc} Improvement	Efficiency Improvement
s				
Bare	34.178	3.7882	0%	0%
Fibo	37.127	3.7767	8.63%	8.3%
TM	38.095	3.7881	11.46%	11.46%
RS	38.816	3.7886	13.57%	13.58%

For our QRN patterns, two advantageous processes occur with the nanostructured coating illuminated by angular incident light: 1) Light striking the pit sidewalls at microscopic scale will result in a more than 90 degree change in incident angle due to reflection on the sidewalls, as well as an increase in the length of refracted incoming light. 2) light reflecting off one pit may strike a neighboring pit or land, which results in an incident angle favorable for transmission. The reflection from a rough surface which randomizes the incident light into a random direction is also known as Lambertian reflection⁹⁷. A higher degree of surface randomness helps in tuning the angle of incidence and achieving the required condition leading to total internal reflection.

5.4.4 Broad practicability and adaptability of our QRNs for all generation solar cells

To assess the broad practicability and adaptability of our well-designed nanostructure for different solar cells, we applied our fabricated QRN ARCs to the different solar cell generations. In fact, our QRNs not only avoid the optical losses by reducing the surface reflection based on their surface randomness, but also generate a forward scattering effect and internal reflections inside the solar cells to increase the “optical path” for all generations of the solar cells.

Fig. 5.4-6 (a) – (b) shows the I-V curve of the different solar cells (i.e., first generation: Si-based photodiodes, second generation: CIGS thin-film solar cells, and photodiode cell) with our QRN ARCs. For Si-based photodiodes, the weak absorption happens at 550 nm due to the Si material being an active layer. The pitch sizes (~400 nm) of our fabricated QRNs will largely have a chance to tune the 550 nm wavelength of the light into “quasi-random” waveguide mode. Moreover, for the CIGS thin-film solar cells, the internal reflections and surface reflectance reduction play important roles. The specific explanation can be found in sections 4.3 and 5.43. Furthermore, as shown in **Fig. 5.4-6 (c) - (d)**, the QRNs have broadband and omnidirectional

antireflection properties over a wide AOI, indicating that our QRNs have a broad adaptability for all generations of the solar cells.

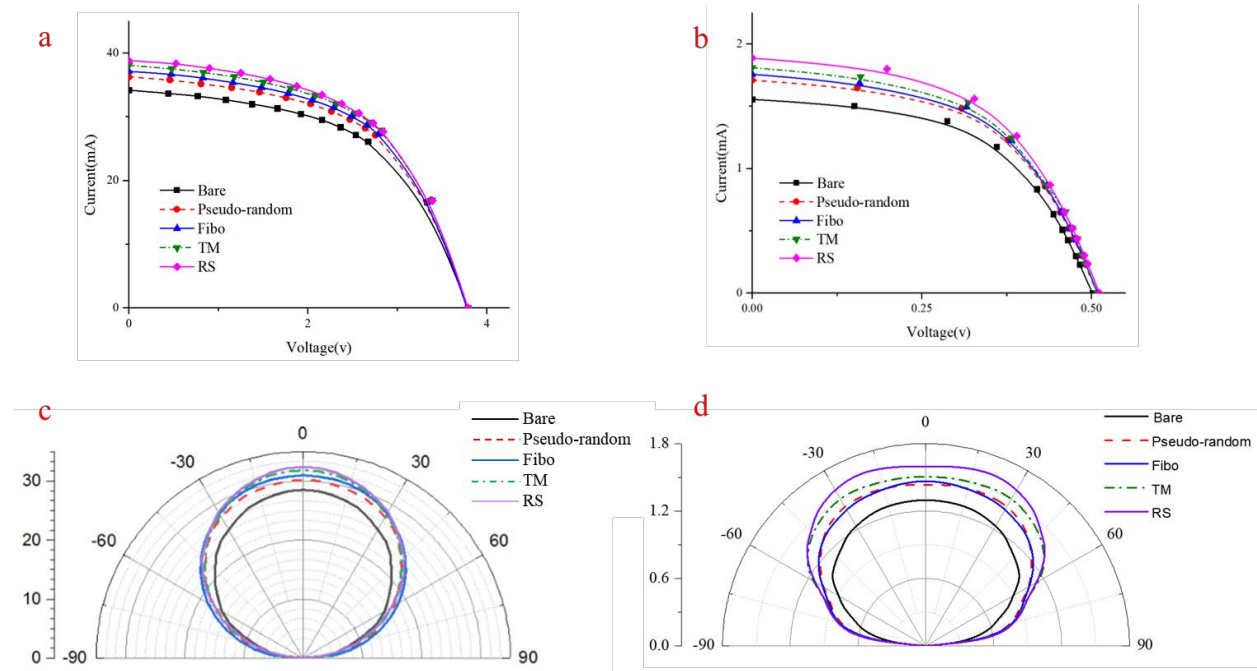


Fig. 5.4-6 (a) the I-V curve of a thin-film solar cell (CIGS) with the different nanostructured coatings and without (solid black line) any coatings; (b) the I-V curve of a photodiode device with the and without (solid black line) any coatings. (c) the omnidirectional distributions of a CIGS thin-film solar cell with different nanostructured coatings; (d) the omnidirectional distribution of a photodiode device with different nanostructured coatings.

5.4.5 Optimization of QRNs based on star discrepancy-assisted patching method

Broadband optimization for reflectance in an exemplary solar device can enhance the average absorption over the visible light spectrum. Here, a patching strategy is proposed to further optimize the selected QRP (i.e., RS as discussed in the previous section) to reduce the reflectance⁹⁸. For a

given QRP, we select different fixed-size square regions and slide them over the entire QRP to calculate the discrepancy values of these regions in relation to the entire pattern. During the heuristic calculations of discrepancies for various region sizes, we have found that the histogram of discrepancy vs. region size roughly obeys a Gaussian distribution, and the maximum discrepancy value of the entire QRP usually occurs when the region size is approximately a half of the short side of the QRP (95% confidence interval). Empirically, optimizing this size should most significantly affect the star discrepancy value of the entire QRP. Thus, we set the region size to be a half of the short side of the QRP, scan the QRP with this region size, copy the region that has the highest discrepancy and paste it to cover the region that inherits the lowest discrepancy, so that the star discrepancy of the entire QRP can increase or converge to a larger value. In doing so, the discrepancy value converts the physical model to a mathematical model and saves us from tweaking dozens of design variables (e.g., filling ratio, pitch sizes, and depth), which could cause numerical simulation issues (e.g., diverging error) and tedious data analysis associated with higher dimensionality (≥ 2 dimensions).

In this optimization process, there are three critical characteristics that we need to confirm: 1) the size of the region with the highest discrepancy value should match the region with the lowest discrepancy value that is to be replaced; 2) the optimization target function is the star discrepancy value of QRP instead of any other physical descriptors (e.g., absorption coefficient); and 3) with a number of replacement/patching iterations, the discrepancy value of the entire QRN will converge to a stable range. Once the three objects are fulfilled, the reflectance simulations for the newly generated/optimized patterns are conducted via Numerical FDTD to validate the optimized optical performance of the new QRPs.

In this paper, we assume that the original RS pattern has a size of 501 units \times 501 units, and we compute the discrepancy values of all possible 250 units \times 250 units regions, which approximately cover $\frac{1}{4}$ of the entire QRP (x - y plane). Based on Eq. (60) and (61), once the region with the highest discrepancy value and the one with the lowest discrepancy value in the original RS pattern are recognized respectively, the patching process is to directly copy the former to cover the region of the latter. This process can be further repeated iteratively until the star discrepancy value converges to a stable zone. The diagram of the QRP's star discrepancy vs. the number of optimization/patching iterations is depicted in **Fig. 5.4-7 (a)**. The star discrepancy of the original RS pattern (without patching optimization) starts at 0.00298, and the star discrepancy value tends to be stable along with the optimization iterations, while the maximum value reaches to 0.01156 (denoted by the red dot at the 46th iteration). For further validation, FDTD simulations are conducted on the original RS pattern and two of its optimized patterns: the original pattern (star discrepancy value: 0.00298) and the optimized pattern at the 7th iteration (star discrepancy value: 0.00618). The structural parameters in this case are set to be pitch size= 400nm and height = 120 nm. A broadband optimization of the QRN light-trapping performance is observed over the solar spectrum from 400 nm to 800 nm and is plotted in **Fig. 5.4-7 (b)**. The two optimized QRNs with drastically increased star discrepancy gradually reduce the surface reflection by up to a 25% decrement in the strong reflectance region (\sim 500nm). In conclusion, optimizing the QRNs based on their star discrepancy values instead of tailoring the QRN physical descriptors in real-space provides a fast and efficient way to avoid thousands of optical simulations to tune the surface morphology parameters for QRNs.

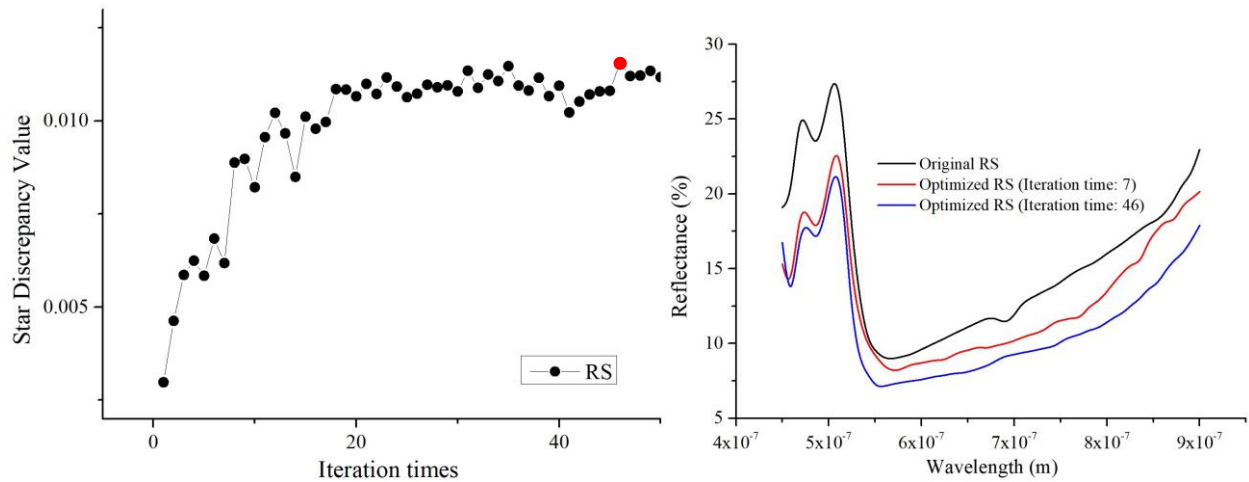


Fig. 5.4-7 Optimization of QRNs' star discrepancy and reflectance for broadband light-trapping. (a) Optimization history of RS QRNs' star discrepancy with 50 iteration times. (b) Simulated reflectance spectrum of the QRNs' structures, before and after optimization over the wavelength range from 400 nm to 900 nm.

5.4.6 Mechanical stability for flexibility and bendability of the thin-film solar cells

Flexibility is a desirable feature of the second generation solar cells for some specific applications, such as outdoor activities and aerospace. As our ARCs are made of PDMS, which are transparent flexible layers, characterization of flexibility and bendability are critical for the thin-film solar cells and its ARCs. Interestingly, it was found that nanostructure could largely enhance the flexibility and the bendability of the thin-film PV devices. In this section, nano-scale thickness renders the thin-film solar cells and our ARCs with respectable flexibility, and **Fig. 5.4-8** shows a photograph of a flexible device. To demonstrate the robustness of the whole device, the PCE improvement of the device with/without QRN ARCs under a bending angle from 0° to 90° was plotted in **Fig. 5.4-8 (a)**. Note that the change of light projection area on the device during a

bending process is considered when calculating the power conversion efficiency. Evidently, the efficiency of thin-film solar devices with our QRNs demonstrates a negligible drop even at a large bending angle, which is much better than its flat counterpart. Based on the schematic diagram in **Fig. 5.4-8 (b)**, the bending angle θ has a relationship with the shortened distance L_s and the maximum height (h_{max}) of the bent cells with reference to the supporting surface $\theta = \arctan\left(\frac{2h_{max}}{L_{solar\ cell}-L_s}\right)$. Note that the PV devices characterized here to have a length ($L_{solar\ cell}$) of 6 cm. Therefore, the whole device was bent with a shortened distance of up to 2 cm when the bending angle was 90° , as shown in the inset photograph of **Fig. 5.4-8 (a)**, while maintaining $\sim 85\%$ of the improved efficiency. Note that the light illumination area of the device was decreased when the shortened distance was increased. This led to a reduction of the input optical power on the device. Therefore, the device PCE improvement was a relative enhancement by considering the change to the device's actual projection area.

To examine the bendability of the devices, we used the same thin-film solar cells with a length of 6 cm and bent them to a shortened distance of 4 cm by applying mechanical force up to 200 cycles. Then, after 100 cycles and 200 cycles, the device electrical performance was measured repetitively. The maximum bending angle of a flexible device was found to be 90° . Beyond that, the flexible bare thin-film solar cell is prone to break the active layers. The effect of the bending cycles on the I_{sc} of the device is presented in **Fig. 5.4-8 (c)**. As a result, the I_{sc} of the device decreased from 32.2 mA to 31.5 mA after 200 bending cycles. During the bending cycles, microcracks and delamination could be produced at the interfaces between different interfaces of the thin-film solar cells, which would deteriorate the device and increase the series resistance of devices. It is noteworthy that in the current device structure, there is no backside passivation, and the entire device is not laminated; thus, the active layer is not in the mechanical neutral plane

during bending. With proper packaging and placement of the films in the mechanical neutral plane, the bending side effects can be minimized, and performance degradation upon bending is expected to be much less.

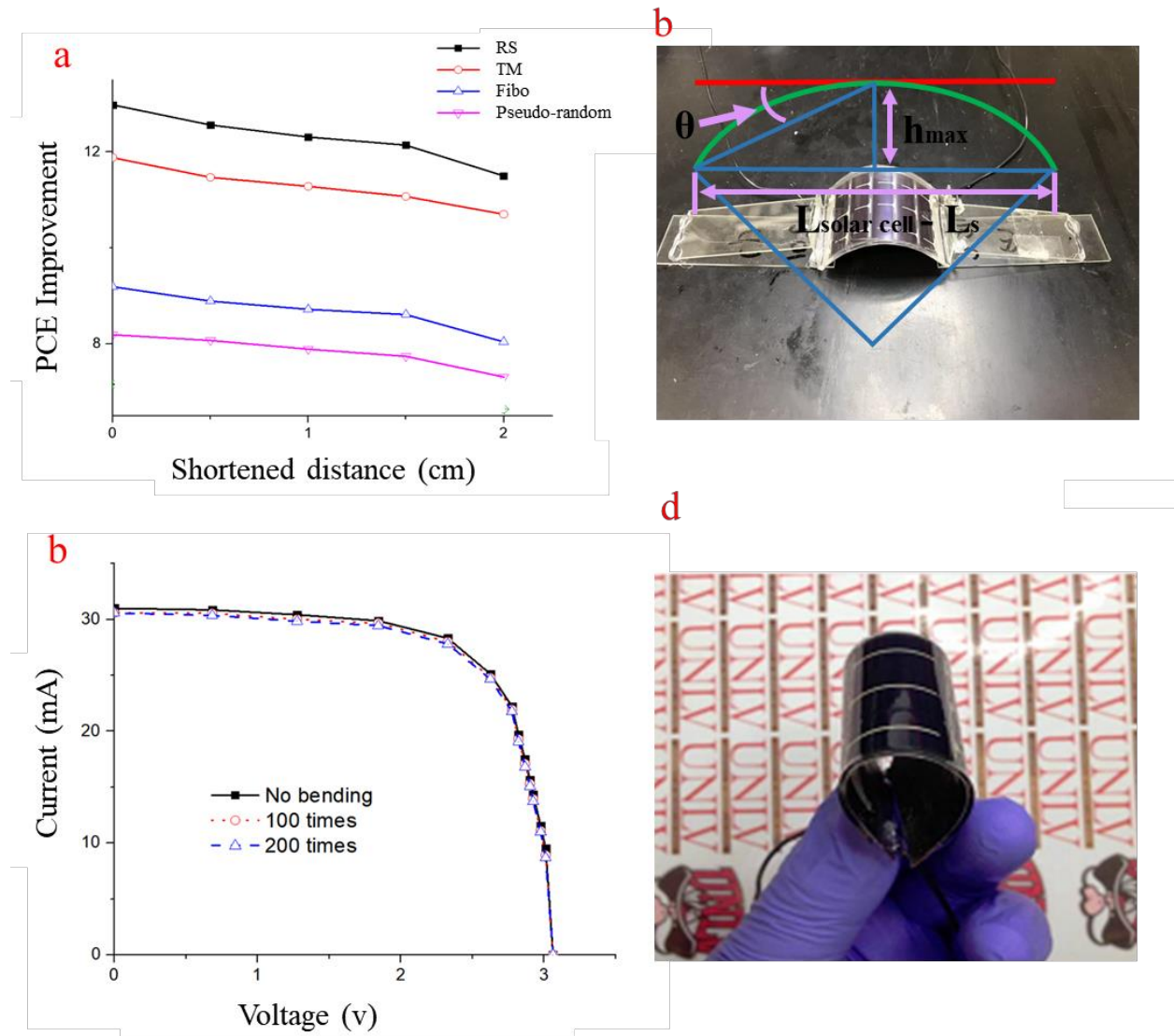


Fig. 5.4-8 (a) The PCE improvement of the different bending angles applied on the thin-film solar devices with our nanostructured coatings; (b) the schematic of the experiment process and its bending angle calculation; (c) the I-V curve with different bending times; (d) the illustration of the flexibility of the thin-film solar cell.

5.5 Conclusion

In this paper, we innovatively import programmable binary data to rapidly and deterministically design 2D QRNs without complicated real-space morphology modeling. The programmable binary QRN design, optimization, and fabrication methodology can be used in any application that benefits from reducing surface reflection in ARCs to broadband light-trapping structures in optoelectronic devices. Furthermore, we introduce the “star discrepancy” as a criterion to assess the degree of surface randomness of QRNs, and further as a guidance to design and optimize QRNs to improve the light-trapping capability. Based on star discrepancy calculation, our QRN follows the order: Halton (2,3) \approx RS < TM < Fibo. A PDMS quasi-random nanostructured coating is created as an ARC as a demonstration. Our well-designed QRNs can be created via nanoimprinting using optical disc technology. Although other storage mediums may eventually replace the conventional optical disc technology for data storage, thanks to our digitally programmed fabrication, we believe that this technology can stand on its own, defy the fate of optical discs in the market, and create a brand-new, exciting high-end, value-added market for the laser-assisted nanostructure fabrication technique. The FDTD simulation shows that the reflectance of the four QRP nanostructures coated on the Si-based solar devices follows the order: Halton (2,3) \approx RS < TM < Fibo in the almost entire visible light spectrum, the opposite to the relationship presented in D_N^* , revealing that a higher degree of randomness improves the antireflection capability. As a result, our best QRNs (i.e., RS) demonstrated the lowest reflectance (10%) at 570 nm and approximately 12% overall PCE enhancement in simulations and optical experiments. The FTA results validate our concept that quasi-random nanostructures offer us a promising potency in light management compared with other nanostructure formats. In addition, a larger photocurrent improvement of over 10% was observed in a wide incident-angle range of

$0^\circ\sim 75^\circ$, suggesting an omnidirectional distribution of redirected incident lights. Except for the optical properties, the flexibility of the solar cell devices has also been studied by applying mechanical forces with 100/200 cycle times. Minor changes in I_{sc} and V_{oc} have been found after each cycle. We expect that this systematic methodology could readily be generalizable to other nanostructures across all length scales, whose performance largely depends on the surface randomness (2D) or even spatial structure distribution (3D).

6 CHAPTER SIX: ENHANCED BROADBAND OMNIDIRECTIONAL ABSORBER UTILIZING 2D/3D DETERMINISTIC QRNS FOR THIN-FILM SOLAR CELLS

6.1 Introduction

Recently, thin-film solar cell technology has been employed to satisfy a variety of practical needs. For example, in aeronautics and astronautics, a solar-empowered drone is competent to carry out the long distancing work without any regard to the power supply⁹⁹. However, those high-altitude long-endurance (HALE) systems are hindered by the low efficiency of the thin-film solar cells due to the massive optical losses at interfaces with the angular incidence in high altitude or latitude areas^{50,61,100}. Therefore, the cell surface must be highly anti-reflective for a broadband solar spectrum (300 nm~900 nm) over a wide angular range so that the solar energy can be adequately absorbed and trapped in the cell. To suppress the surface reflection, surface decoration using nanostructures is a prevalent approach for the light-trapping scheme because the path of the incident light is increased in the absorber by optimizing the morphology at the interfaces. Although a variety of 1D/2D nanostructure designs are consequently carried out to show a great potential for light manipulation, most of the studies have focused on 1D/2D characteristic parameters (i.e., x - y plane), such as feature size, aspect ratio, and filling ratio, which cannot solely explain the high performance of light-trapping structures at the angular incidence. Apparently, a different situation would be attained if light-trapping could not only be controlled at the x - y plane but also be tuned along the z -direction. Therefore, rational 3D nanostructure designs for broadband efficiency improvement under normal incidence and large angle incidence are still needed for many applications. Other characteristic parameters describing the 3D space distribution, but not limited to 1D/2D plane parameters, should be taken into account. When contemplating achieving a better antireflection at a wider AOI, the other key factor is unknown and constantly questioned.

Interestingly, plants adapt to contrasting harsh environments by simultaneously obtaining optimal configurations in multiple traits, such as wide angular insolation in a high latitude region. The ecological adaptability, as a result of nature survival strategies, makes plants have both different morphology and dimensions in order to achieve the needed functionality. Those plants with broad distributions show collective variances in leaf morphology and photosynthetic physiology, which could be adaptive to difference insolation caused by seasonal and latitude shifts. One such species is the narrow-leaf cottonwood (*Populus Angustifolia* James), which is a foundation species along the Rocky Mountains, spanning 16° of latitude in North America¹⁰¹. Based on the investigation of ecophysiological adaptation associated with latitude, the deciduous trees from higher latitudes exhibit higher photosynthetic capacity, compensating for the shorter daytime and reduced insolation in high latitude areas. By researching the association between leaf morphology (*Populus Angustifolia* James) and photosynthetic physiology in northern and southern areas, the folia traits contribute to higher photosynthetic capacity in higher latitude zones, manifesting in different structure geometries on the surface of leaves¹⁰². The prominent veins and trichomes on the leaves have various heights from various areas with different latitudes to ensure the plants have surface reflection reduction and self-protection. Furthermore, the heights of the vein segments tend to be a quasi-random like distribution to make the leaf surface rough and have a higher mass density in the northern area. The underlying optical physics can be used to explain and investigate these leaf traits¹⁰³. In low latitude areas or during the summer, the leaves of *Populus* receive more direct sunlight, and the excessive sunlight containing strong UV light will damage the leaf surface and raise the leaf temperature. It could be a disadvantage because respiration rates and temperature should be closer to optimal for photosynthesis. Meanwhile, in high latitude areas or winter (i.e., insufficient sunlight conditions), the leaves of *Populus* need to adjust their surface

morphology to minimize the reflectance of the invisible light wavelength and the long wavelengths, allowing the leaves to increase the sunlight absorption. A natural survival strategy to achieve this goal is to change the height and arrangement of veins and trichomes. Taking this incredible finding back to our study, these characteristic parameters (i.e., pitch sizes, heights, surface arrangement) could be essential elements in exhibiting broadband and omnidirectional antireflection over a wide AOI, as well as assisting us in determining the optimal nanostructure design for thin-film solar cells.

Inspired by nature, this CHAPTER presents a systematic 3D deterministic disordered nanostructure design based on their spatial distribution, in which their surface morphology, arrangement, and height can be precisely controlled by tuning the nanostructures' characteristic parameters at both the x - y plane and the z -direction to reasonably manipulate light reflection, extraction, and propagation. The digitalized binary sequences (Rudin-Shapiro, Fibonacci, Thue-Morse) are used to create pit/land quasi-random nanostructures (QRNs) for the thin-film (Si-based absorber). Furthermore, our proposed method is mass-production compatible with the existing optical disc technology, giving us a cost-effective way to fabricate these nanostructures. The FDTD simulation is applied to test the reflectance and works perfectly well for textured surfaces. As a result, the 3D QRNs outperformed the 2D QRNs in the optical and electrical simulations. For the best spatial distribution, 3D Rudin-Shapiro QRNs with a 150 nm nanostructure pitch size and quasi-random distributed heights, we see a considerable improvement in the electrical/optical properties. Reflection is suppressed for a wide range of AOI, resulting in the greatest efficiency enhancement at an incident angle of 75 degree (around 35% reflection reduction). This work could pave the way for oblique incidence to overcome the 1D and 2D issues while also achieving a quasi-random appearance with the randomized heights.

6.2 3D Nanostructured Cell Design and Method

6.2.1 3D nanostructure design overview based on its spatial distribution

In this CHAPTER, the spatial distribution refers to simultaneously controlling the distribution of surface morphology and arrangement at the x - y plane as well as heights along the z -direction in 3-dimensional space. In an innovative way for deterministic disordered nanostructure design, programming binary data is proposed as an innovative method to describe the spatial distribution of the 3D deterministic disordered nanostructures. It provides us with an efficient way to build up a connection between the physical model and the mathematical model. Thus, two individual sets of binary data would be generated by different approaches to describe the spatial distribution in x - y - z space, and they are detailly explained in sections 6.22 and 6.23. In an exemplary embodiment, the binary matrixes are generated for surface morphology and arrangement at the x - y plane, and a string of binary data is also generated for the randomized heights along the z -direction. For the x - y plane, there are two main methods to rationally design the 2D patterns of nanostructures: 1) a binary matrix for 2D patterns at the x - y plane is generated by arranging the original 1D binary sequences in an inside-out Archimedean spiral way; 2) a binary matrix for 2D patterns at the x - y plane by directly using 2D sequence generators to generate the 2D binary matrix. For the z -direction, a string of binary data is generated using a quasi-random generator, and the binary string is divided into sub-intervals. For sake the of comparison, the spatial distributions are classified as periodic and quasi-random nanostructures.

6.2.2 Surface morphology (x - y plane) design using programmable binary data

For any binary 2D pattern, we can always use rectangle unit building blocks that are small enough to digitize the entire 2D pattern and map it to an m -row-by- n -column binary matrix, like a digital image in pixels. In other words, each unit building block in a 2D nanostructure pattern

stands for either a “pit” (i.e., “1” or a black building block in a 2D matrix pattern) or a “land” (i.e., “0” or a white building block in a 2D matrix pattern), and its position in the matrix is defined by a pair of integer tuple (x, y) as its coordinates, where $1 \leq x \leq m, 1 \leq y \leq m$. Based on this concept, three approaches to develop the desired binary 2D QRPs for light manipulations, namely: 1) converting 1D binary sequences to 2D QRPs; 2) directly generating 2D QRPs; and 3) digitalizing the existing 2D QRPs in other forms (e.g., channel and particle forms), have been detailly described in section 5.22.

6.2.3 Randomized heights design of QRNs with quasi-random distribution along the z -direction

For the randomized heights of nanostructure design along the z -direction, the binary sub-intervals with assigned height values are generated for pits to ensure the pits’ heights along the z -direction have pseudo-random or quasi-random distribution by the following method:

A string of binary data (like {0100110...}) is generated using a 1D pseudo-random or quasi-random generator. Then, the string will be divided into m sub-intervals with n bits inside to meet different requirements. These sub-intervals with different height scales are assigned to pits in an orderly fashion. To be noticed, the same sub-interval represents the same height scale. In doing so, the pits’ heights along the z -direction can be quasi-random distribution. In a basic embodiment, we select a total of 3 bits in a sub-interval, like {010}, {011} The total number of height scales becomes $2^3=8$ scales. Then, the sub-intervals representing different height scales are assigned to each pit, followed by the 2-dimensional arrangement (inside-out spiral). Eventually, the 2D deterministic disordered pattern can be extruded to be a 3D deterministic disordered nanostructure design, whose spatial distribution dominates light-trapping properties.

6.2.4 Converting 2D nanostructure pattern to 3D nanostructure patterns by assigning randomized height scale

For the randomized heights of nanostructure design along the z-direction, the number of the height scales is determined by binary data selection. In this CHAPTER, a binary data set has 3 bits inside. The total number of height scales is $2^n=8$. The total number of height scales becomes $2^3=8$ scales. The eight height scales are set as 50nm, 60nm, 70nm, 80nm, 90nm, 100nm, 110nm, and 120nm, respectively (*Table 4*). The order of allocation will follow the rules of 1D quasi-random binary data. For example, 1D Rudin-Shapiro binary data goes like this:

$$1110110111100010 \dots \quad (63)$$

Equivalently, separating the sequence by every 3 bits gives us:

$$111/011/011/110/001/011 \dots \quad (64)$$

Then, these eight height scales (*Table 4*) will be assigned to each unit nanostructure (i.e., pit). It makes the 2D patterns turn out to be a 3D nanostructure design, whose spatial distribution dominates the light-trapping properties.

Table 4 Eight specific height scales related to the sub-intervals (3 bits)

Binary	Height (nm)	Binary	Height (nm)
000	50	111	90
001	60	100	100
010	70	110	110
011	80	101	120

As shown in **Fig. 6.2-1**, 3D QRPs are designed on the surface of the active layer of an a-Si:H thin-film solar cell to inherit the merits from 2D QRNs and the randomized heights that cause the higher spatial randomness. The pitch size is designed to be 150 nm, and 8 height scales assigned to each pit are discussed above. Because the purpose of this CHAPTER is to study how the different degrees of spatial randomness could further reduce the surface reflectance and favor the absorptance, we perform the dependence studies on the degree of spatial randomness while other characteristic parameters are fixed. The FDTD simulations and CHARGE simulations are established to evaluate the 3D QRNs and verify our concepts.

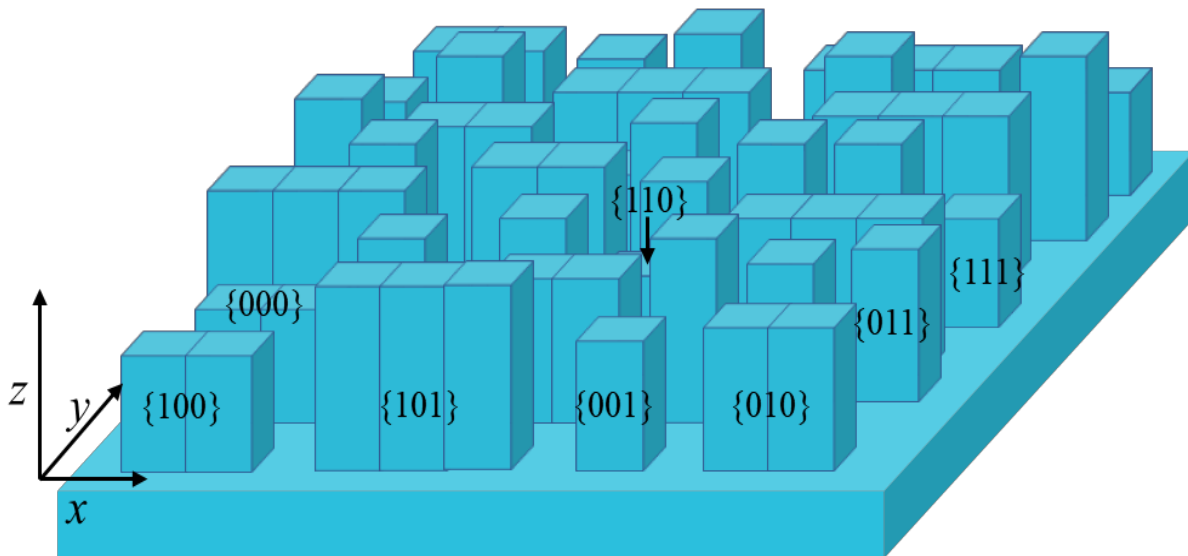


Fig. 6.2-1 An illustration of a 3D QRN design assigned by randomized heights, and 8 heights are quasi-randomly distributed.

6.3 Theory

Based on CHAPTER FIVE, the different degrees of surface randomness (2D) for different QRNs were investigated, and one can find the higher surface randomness would give us a lower reflectance under the normal or angular incidence. The spatial distribution is further evaluated in this CHAPTER by varying the surface morphology at the x - y plane and the heights along the z -direction. Using our discrepancy calculation and controllable binary data, we can easily evaluate the spatial distribution of the QRNs in spite of how complex the QRNs are.

6.3.1 Spatial distribution evaluation based on discrepancy calculation

Applying the theory in Section 5.31, we first segmented the 2D binary matrix into unit square blocks at the x - y plane, and each block is painted into black if it is assigned “1” and white otherwise. For $\mu_x(J)$, it will be calculated the sum of the volume of the black blocks in subset J over the sum of the volume of the total black blocks in I^3 . For $\mu(J)$, it will be calculated the total volume of subset J over the total volume of total blocks in I^3 . Therefore, the discrepancy becomes:

$$D_N = \left| \frac{\text{Total volume of black boxes in } J}{\text{Total volume of total black boxes}} - \frac{A}{B} \right| \quad (65)$$

where A is the total volume of J , and B is the total volume of total blocks in I^3 . Take a similar example of Eq. (60), as that is illustrated in **Fig. 5.1-1 (e)**, I^3 contains 31×78 unit-blocks in total and 581 black ones, while a subset J (i.e., the red rectangle) has 11 black blocks in a total of 5×7 blocks. Thus, the total volume of black blocks in J is the sum of the volume of these 11 black blocks. Remember that the height scales will be assigned to these black blocks (i.e., pits), and the height values of these 11 black blocks can be easily tracked from the sub-intervals. Therefore, the total volume of black blocks in J and the total volume of all black blocks in this pattern can be calculated. The total volume of J is considered as the whole area of $J \times$ the largest value of the

height scales, and the total volume of total blocks in I^3 is considered as the whole area \times the largest value of the height scales. Thus, the discrepancy of J in this pattern becomes $D_N =$

$$\left| \frac{(\text{height}_1 + \text{height}_2 + \dots + \text{height}_{11}) \times \text{unit area}}{(\text{height}_1 + \text{height}_2 + \dots + \text{height}_{581}) \times \text{unit area}} - \frac{5 \times 7 \times 6}{31 \times 78 \times 6} \right| \approx 8.45 \times 10^{-2}.$$

Being more trackable than the varied values of discrepancies for all subsets J in I^3 , the maximal deviation of all possible discrepancies, the star discrepancy (D_N^*), is employed as a criterion to evaluate the level of randomness of the spatial distribution.

6.3.2 Relationship of the degrees of 2D surface randomness and the degrees of 3D spatial distribution

For ease of calculation, 30 pits are chosen inside each pattern to calculate the star discrepancy for each type of QRNs (i.e., RS, TM, Fibo). As shown in **Fig. 6.3-1**, the degrees of surface randomness for each type of QRNs follow the order: RS > TM > Fibo, while the degrees of spatial randomness exhibit the same tendency, implying that the higher dimensional QRN design can further increase the degrees of the randomness at the interface. Besides this, when the height of each pit is randomized, the D_N^* of the Fibo and TM are even higher than the best 2D QRP (i.e., RS). Due to the mentioned concept of CHAPTER FIVE, we hypothesize that our 3D QRN design could outperform the 2D QRNs in a light-trapping scheme. Although both surface morphology and randomized heights play an important role in light-trapping properties, calculating and optimizing the D_N^* of the QRNs show us a way to efficiently design and evaluate the QRNs without being hindered by control variate technique.

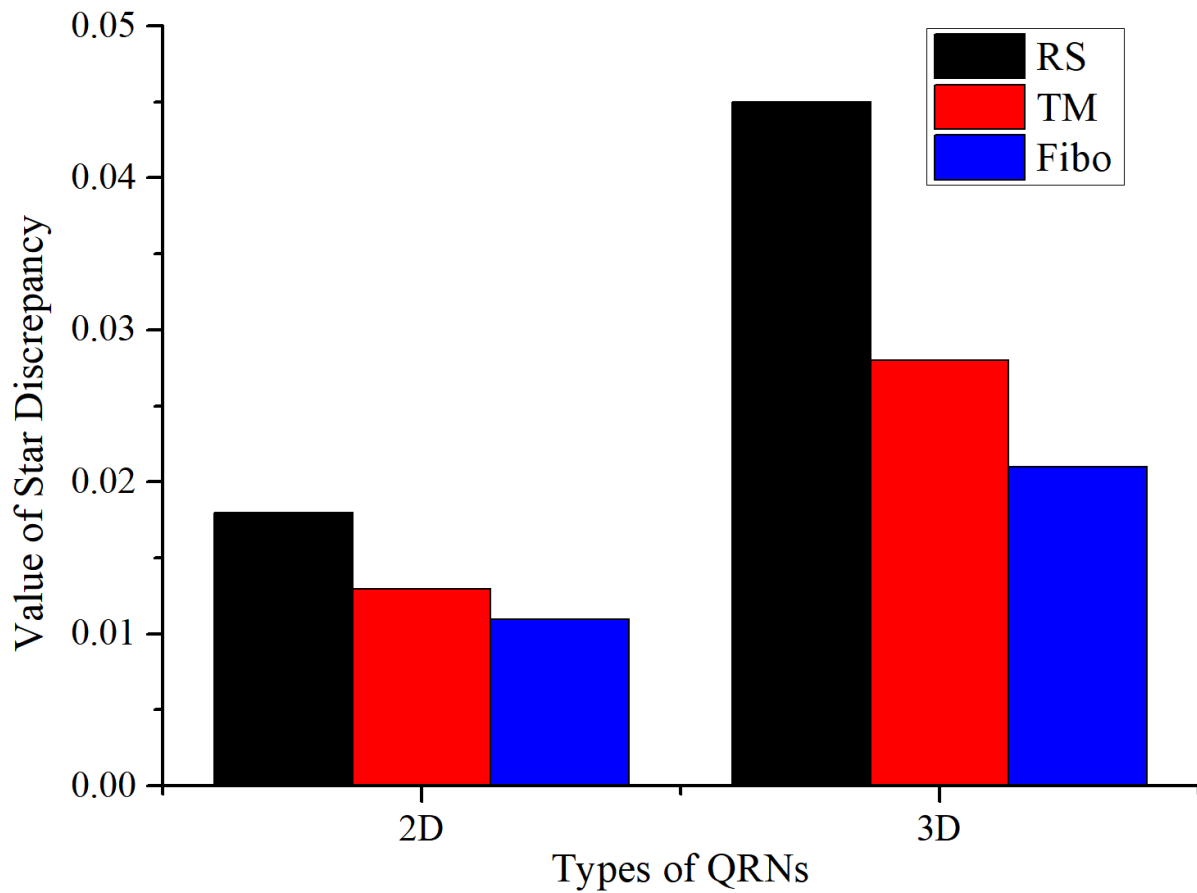


Fig. 6.3-1 The comparison of 2D and 3D QRNs based on their star discrepancy.

6.4 Discussion and Conclusions

6.4.1 The reflectance and absorption analysis based on numerical results

To understand the lower reflection over a broad visible wavelength, the reflection spectra of the 3D, 2D QRNs and the slab cell are presented in **Fig. 6.4-1 (a)**. In the broad spectrum from 300 nm to 1200 nm, less reflection of the 3D QRNs is observed compared to those of the 2D QRNs, and slab cell. However, in the relative narrow bandwidth from 700 nm to 900 nm, the reflectance

of the 3D QRNs almost has the same amplitude. This appearance demonstrates that our 3D QRNs assist our solar cell better in a shorter wavelength range. To be noticed, the reduction of the reflectance is slowly converged when the reflectance of the whole device reaches up to 10%, which results in the absorption enhancement factor: $4n^2$, where n is the refractive index of the absorbing material.

Subsequently, the absorption is calculated and evaluated by the electric field distribution of one unit row. Note that our QRNs were designed along a plurality of tracks. Therefore, from one particular side (i.e., the y - z plane), the cross-sectional figure of the nanostructured semiconductor is the same as the nanostructured grating. **Fig. 6.4-1 (b) – (g)** depicts the distribution of electric field density ($|E|^2$) with a propagated electromagnetic (EM) wave at 500 nm. To be more specific, the plane EM is propagated from the topside ($Y=3\mu\text{m}$) to the surface of the nanostructured coating ($Y=0\mu\text{m}$). A higher magnitude of $|E|^2$ at the interface between nanostructures and air could be seen by different color indexes, which indicates that our quasi-random nanostructures have stronger electric field intensity inside solar semiconductors. It means our quasi-random nanostructures could easily couple the plane EM wave and increase the light-trapping property. From top to bottom in **Fig. 6.4-1 (b) – (d)**, a higher electric field intensity is observed inside nanostructures compared to the **Fig. 6.4-1 (e) – (f)**, indicating that our 3D QRNs outperform the 2D QRNs. Besides this, the electric field intensity is extremely dropped when reaching to the bottom of the semiconductor layer, implying that most of the light has been absorbed by the semiconductor. However, for the 2D QRNs, there is a strong electric field intensity at the bottom, where the light will be transmitted and finally go through the semiconductor.

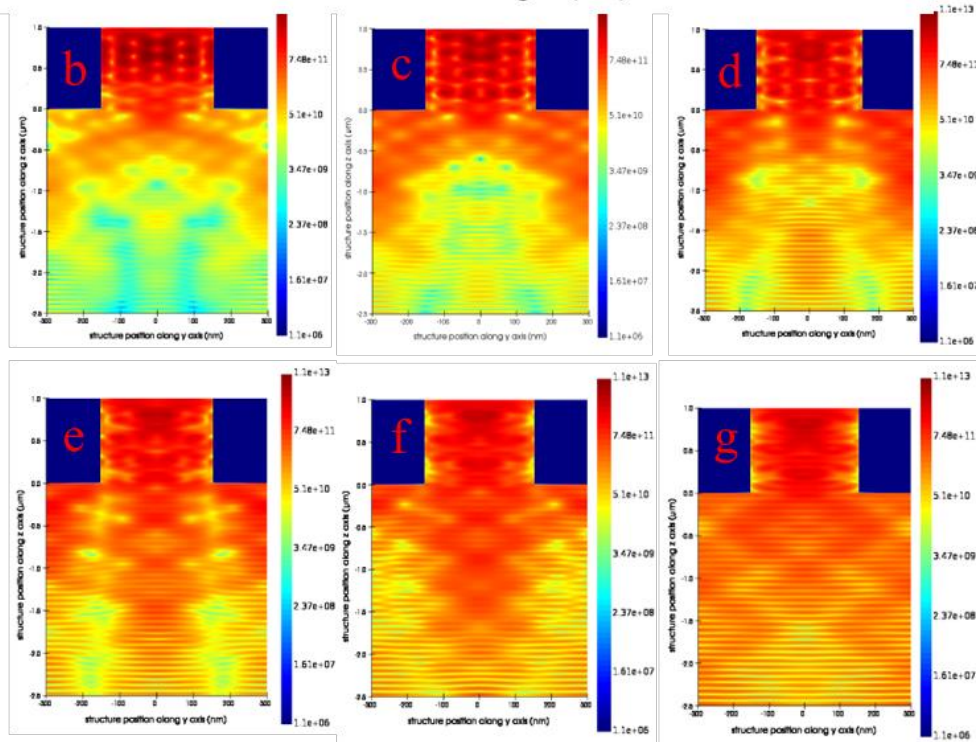
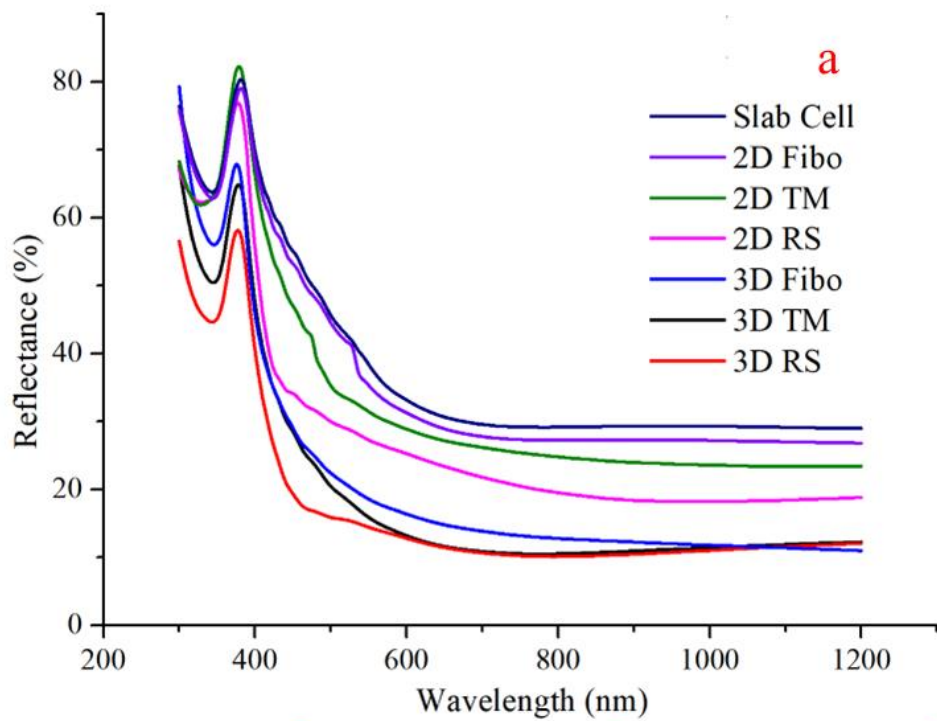


Fig. 6.4-1 (a) The reflectance of a thin-film solar cell (Si-based) with different 2D and 3D quasi-random nanostructured active layers (without any back reflectors). (b)-(g) the filed electric field intensity for different 2D and 3D quasi-random nanostructured Si-based active layer: (b) 3D RS; (c) 3D TM; (d) 3D Fibo; (e) 2D RS; (f) 2D TM; (g) 2D Fibo.

6.4.2 Simulated I-V characteristic

In this section, the CHARGE solver (Lumerical company) is used to model the real solar cell working situation. Compared to the ideal Si material in FDTD, the CHARGE solver enables us to take the non-ideal effects such as bulk and surface recombination into consideration¹⁰⁴⁻¹⁰⁶. Based on the simulations and calculations, the short circuit density (J_{sc}) is 22% lower than the one generated in FDTD. The reason is that the carriers now have the chance to recombine before they are collected at the contact, and the distance they are traveling depends on where they are generated. **Fig. 6.4-2** shows the J - V curve of the Si-based solar cell with our 2D/3D QRNs. As a result, the 3D QRNs beat the 2D QRNs with the highest improvement of around 15%, and around 19.2% compared to slab cell. This result also matches up with our star discrepancy calculation and FTA results.

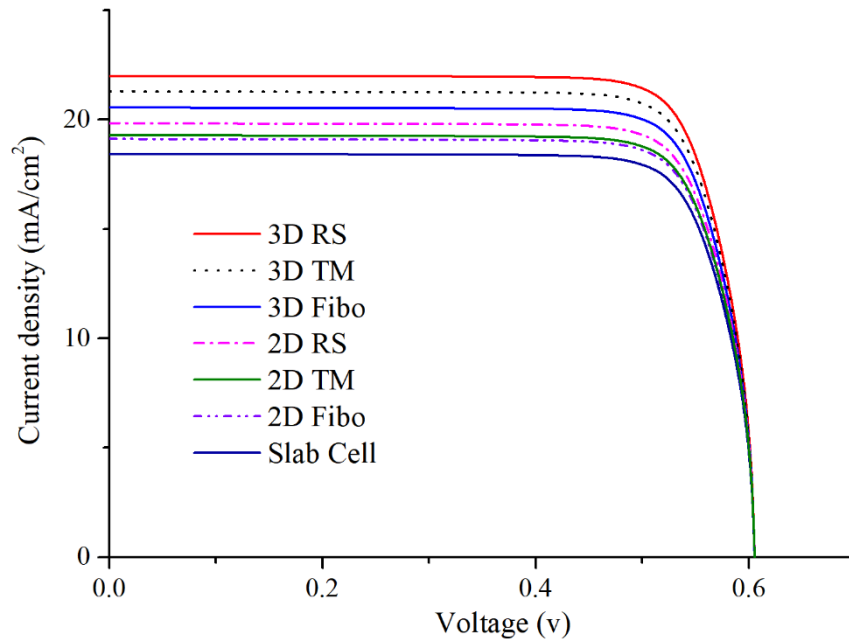


Fig. 6.4-2 The I-V curve of the Si-based solar cell with the different 2D/3D quasi-random nanostructured active layers.

6.4.3 Angular wavelength-dependent for Si-based solar cell with 2D/3D QRNs

It is worth pointing out that all the experiments above were conducted under perpendicular incident light. In fact, sunlight dynamically irradiates the land from the east to the west during the daytime. Therefore, we have investigated the wavelength-related reflectance of the Si-based solar cell with our 2D/3D QRNs under the angular incidence. The incident angle is defined as the angle between the incident light and the horizontal plane of the devices. Particularly, the light incident angle was changed from 0° to 75° with a 15° step, and the reflectance was weighted for ease of assessment. As a result, **Fig. 6.4-3** indicates that our 2D/3D QRNs have a slightly better broadband reflection reduction compared to the normal incidence for small incident angles, while the reductions are largely increased for large incident angles. This is because, for large incident angles, the gaps between every single pit cause more internal reflection leading to more photon travel path length. Comparing 2D QRNs and 3D QRNs, it clearly indicates that 3D QRNs demonstrate a better reflection reduction all over the visible light wavelength with difference incident angles. This intriguing effect can be explained as follows. A pattern with a higher dimension and degrees of spatial randomness will cause more scattering effect (i.e., Mie scattering), generating a forward scattering in addition to the efficient light-trapping property. Besides this, a higher degree of spatial randomness will have more chances to randomize the light path and to generate more internal reflections, resulting in lower broadband reflectance all over the incident angles. The largest reduction is observed at 75 degrees, which gives us $\sim 35\%$ reduction on weighted reflectance. The omnidirectional improvement of light absorption and energy conversion efficiency is of the significance for practical deployment of solar panels without a costly solar tracking system.

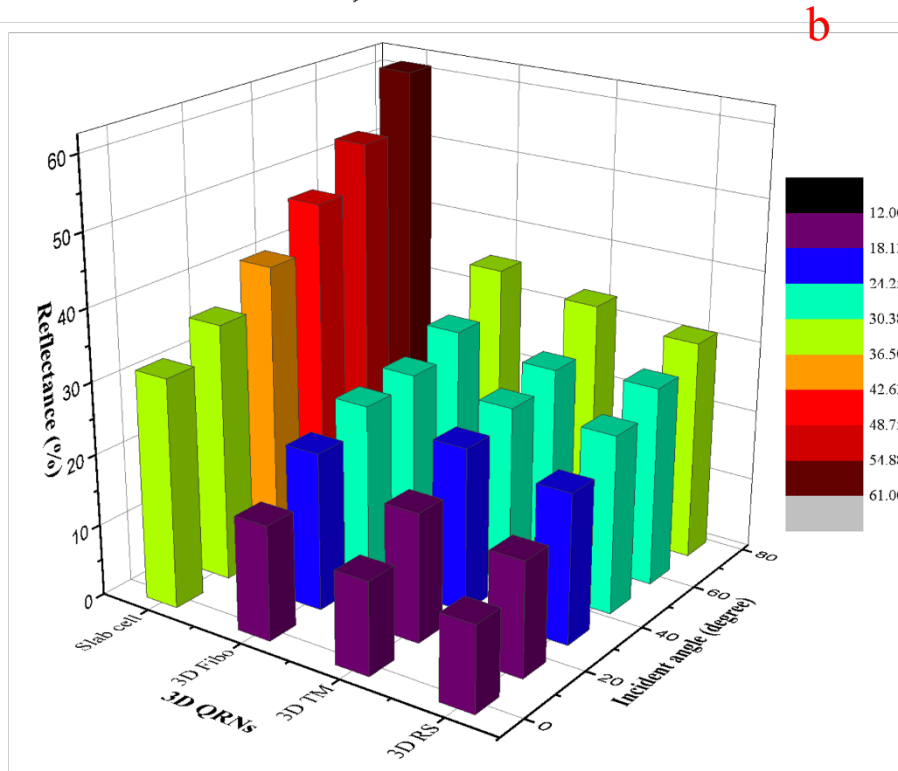
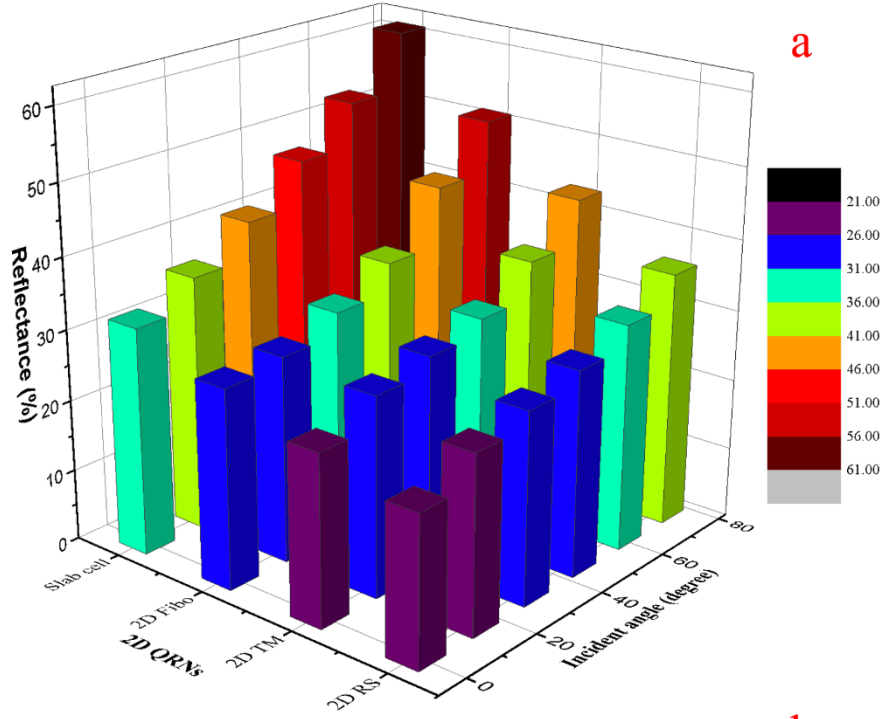


Fig. 6.4-3 The 3D plot of the reflection, AOI, and different types of QRNs with x - y , x - z , and y - z bars of the data plotted inside the cube.

6.5 Conclusions

In conclusion, we have demonstrated the use of the FDTD simulation and CHARGE solver to assess the optical and electrical performance of the 2D/3D QRN nanostructured Si-based solar cell. We find that the 3D QRN design outperforms the 2D QRN design for a nanostructured semiconductor layer of a solar cell by taking the randomized heights into consideration. These different types of 3D QRNs possess a higher degree of spatial randomness by assigning the randomized heights to the nanostructures, which leads to a highest J_{sc} enhancement of up to 22% compared to slab cell. Furthermore, the 3D QRNs resulted in an omnidirectional and broadband reduction in optical reflectivity. The successful 3D QRN design here can be extended to other material systems to enable high-performance PVs.

7 CHAPTER SEVEN: CONCLUSIONS AND FUTURE WORK

7.1 Conclusions

This dissertation focused on the several types of QRNs working as light-trapping structures to reduce the surface reflection and maximize the absorption all over the visible light wavelength for current photovoltaic devices, emphasizing correlation of their spatial randomness and optical properties using combined physical experimental and simulation approaches. A novel design method is proposed in this dissertation to efficiently digitize and program the QRNs, which skillfully bypasses the uncertain QRN generation and makes the QRN design deterministically programmable. Despite many direct and indirect characteristic parameters (e.g., pitch size, porosity, filling ratio and nanostructure arrangement, etc.) for nanostructure design, a “star discrepancy” calculation is employed as a criteria to guide us to evaluate and further optimize the designed QRNs.

This work has shown that our proposed QRNs have a broad practicability in a light-trapping scheme. In CHAPTER FOUR and FIVE, the 1D spiral grating nanostructure and the different types of the 2D QRNs (i.e., RS, Fibo, TM, and Halton (2,3)) are designed and generated on the ARCs, which largely reduce the optical losses and prolong the light path inside the devices. In CHAPTER SIX, the 3D QRNs are designed by extruding the 2D QRPs with assigned various height scales. Using FDTD and CHARGER solver, optical and electrical properties are investigated, and we show that our 3D QRNs can further increase the absorption of the semiconductor and manipulate the light path inside the semiconductor. Besides this, our QRN design also shows a broad adaptability for all generations of photovoltaic devices. Our QRN ARCs demonstrate a broader band of wavelength-dependent reflectance reduction for Si wafer-based, thin-film solar cells (e.g., CIGS), and photodiodes.

In CHAPTER FOUR, an innovative hybrid 2D nanostructure design is proposed based on the merit characteristics of both Archimedean spiral and quasi-random nanostructures to achieve outstanding light-trapping capacity. Using optical technology and the Fibonacci sequence enables us to perfectly fabricate “pits” and “lands” nanostructure form along with the Archimedean spiral arrangement. Broadband, angle-independent nanostructured ARCs are assessed using FDTD simulation and experimentally validated by presenting the I-V curve and omnidirectional test results. Compared to the bare solar cells, the efficiency improvement of the solar cell devices is up to 8.31%. Meanwhile, the reflectance on the surface is tremendously reduced by 11.62% at 800 nm. The results show that either the spiral arrangement of nanostructure or QRNs play the key role in the light-trapping scheme.

In CHAPTER FIVE, we investigate how the different types of 2D QRNs with fixed height affect the light-trapping property. We introduce the star discrepancy as a criterion to assess the degree of surface randomness of QRNs, and further as a guidance to design and optimize 2D QRNs to improve the light-trapping capability. The optical disc technology enables us to generate our well-designed QRNs on the PDMS ARCs. As a result, the performance of our best QRNs (i.e., RS) has demonstrated the lowest reflectance (~10%) at 570 nm and approximately 12% PCE enhancement in simulation and physical experiments. By changing the star discrepancy (i.e., the degree of surface randomness for 2D nanostructure) of RS QRNs, the RS QRNs can be optimized. The two optimized QRNs with drastically increased star discrepancy gradually reduce the surface reflection by up to 25% decrement in the strong reflectance region (~500 nm). Except for the optical properties, the flexibility of the solar cell devices has also been studied by applying mechanical forces with 100/200 cycle times. Minor changes in I_{sc} and V_{oc} have been found after each cycle.

In CHAPTER SIX, different height scales are assigned to 2D QRPs, making the 2D QRPs into 3D QRNs. A higher-dimensional “star discrepancy” (i.e., degree of spatial randomness) is calculated to evaluate the light-trapping properties. In this work, the 2D/3D QRNs are designed on the active layer for the sake of greater absorption for thin-film solar cells. Two different numerical methods were applied to test the optical and electrical properties of the 2D/3D nanostructured a-Si:H solar cells. One is used for the reflectance of the solar device with/without our designed QRNs under the normal and angular incidence all over the visible light wavelength, and the other is to produce the $J-V$ curve for comparison. The results exhibit that the absorption of 3D QRNs outperform the 2D QRNs, and the improvement follows the order with their star discrepancy: 3D RS > 3D TM > 3D Fibo > 2D RS > 2D TM > 2D Fibo. In addition, to lift the optical performance and electrical performance of the thin-film solar cells, 3D QRN design has shown their advantages in a higher degree of spatial randomness due to the randomized heights compared to 2D QRNs, especially under the angular incidence.

Finally, these outcomes contribute to the field of PV due to the QRNs in the light-trapping scheme to further improve the efficiency. They can be utilized on not only as an ARC but is also relevant to improve the absorption of the semiconductor layer. In order to convert the optical benefits to the efficiency of the PVs, more work needs to be done to efficiently translate our designed QRNs to real-world surfaces. Meanwhile, the use of optimizing the degree of spatial randomness for QRNs in this thesis is an achievable task. A better optimization method instead of patching optimization method should be further developed.

7.2 Future Work

7.2.1 Achieving a higher degree of the spatial randomness for QRNs

In this thesis, we discussed the QRNs generated by the use of optical disc technology. However, due to the spiral arrangement property, our fabricated QRNs have a grating view from the y - z plane. It limits the degree of spatial randomness for QRNs. Since our 2D QRNs are fabricated by a mold derived from an optical disc, it provides us a new way to break the symmetry from the y - z plane by rotating the second mold at a specific angle and transferring the QRP on the second mold to the first mold. Luckily, the hot embossing technology makes this concept achievable:

Complex 2-D QRN design via stacking method:

Complex 2D QRNs could be designed by stacking the same or different QRPs according to their configurations (i.e., different optical discs) with independent angles θ_{stack} (0-180 degree) via hot embossing and soft lithography technologies. The angle θ_{stack} is defined as the angle between the two longitudinal axes of one QRP and another QRP. Herein, angle θ could be multiple and not limited, which depends on how many stacks need to be applied to the molds. Thus, every QRP stacked with one or more additional QRPs will provide us an easy way to generate 2-D nanostructures, expanding the “pits” and “lands” format in different directions.

Hot embossing technology:

In a basic embodiment, the QRP mold derived from an optical disc is made of polycarbonate. First, we prepare two QRP molds (i.e., CD, DVD, or Blu-ray molds) for future use. Then, we use soft-lithography technology to transfer the QRP on the second mold to a PDMS template. After finishing the soft PDMS template process, the first QRP mold will be placed on the heating platen,

and the PDMS template will be laid over it. A pressure of 2.23 MPa will be applied to the first QRP mold for the hot embossing under a temperature of 165 degrees (the glass temperature of the polycarbonate substrate) for 5 mins. After cooling down, a polycarbonate mold with two QRP stacked at an angle is ready to be used. To be noticed, it is one stacking process for complex 2D QRNs, and repeating this process can make multiple stacks available depending on the requirements.

By choosing different optical storage disc formats, a complex 2D nanostructured mold with one stack would be fabricated to be a CD-CD 2D QRP mold, a DVD-DVD 2D QRP mold, a Blu-ray-Blu-ray 2D QRP mold, a DVD-CD 2D QRP mold, a CD-Blu-ray 2D QRP mold, or a DVD-Blu-ray 2D QRP mold.

To validate our fabricated complex 2D QRNs, the diffraction phenomenon of the light caused by the molds (i.e., CD, DVD, and Blu-ray molds) is observed. A 405 nm laser is applied to the QRN molds, and all the samples are tested with/without an angle $\theta_{stack}=60^\circ$ between two overlaid QRPs. In **Fig. 7.2-1 (a)**, there are three different diffraction phenomena, which are: 1) third-order diffraction for the CD mold, 2) first-order diffraction facula for the DVD mold, and 3) zero-order diffraction for the Blu-ray mold. In **Fig. 7.2-1 (b)**, a complex 2D QRP mold (CD-CD mold), the diffractions are distributed as a hexagon shape, and the diffraction along two longitudinal axes becomes brighter than the others, which indicates that the second QRP is successfully transferred to the first QRP mold. To simply evaluate the optical performance of the complex 2D QRNs, FFA is conducted as shown in **Fig. 7.2-1 (c)**. A higher spectral power density illustrates our complex 2D QRNs achieve a broader spectrum of energy than the original 2D QRNs.

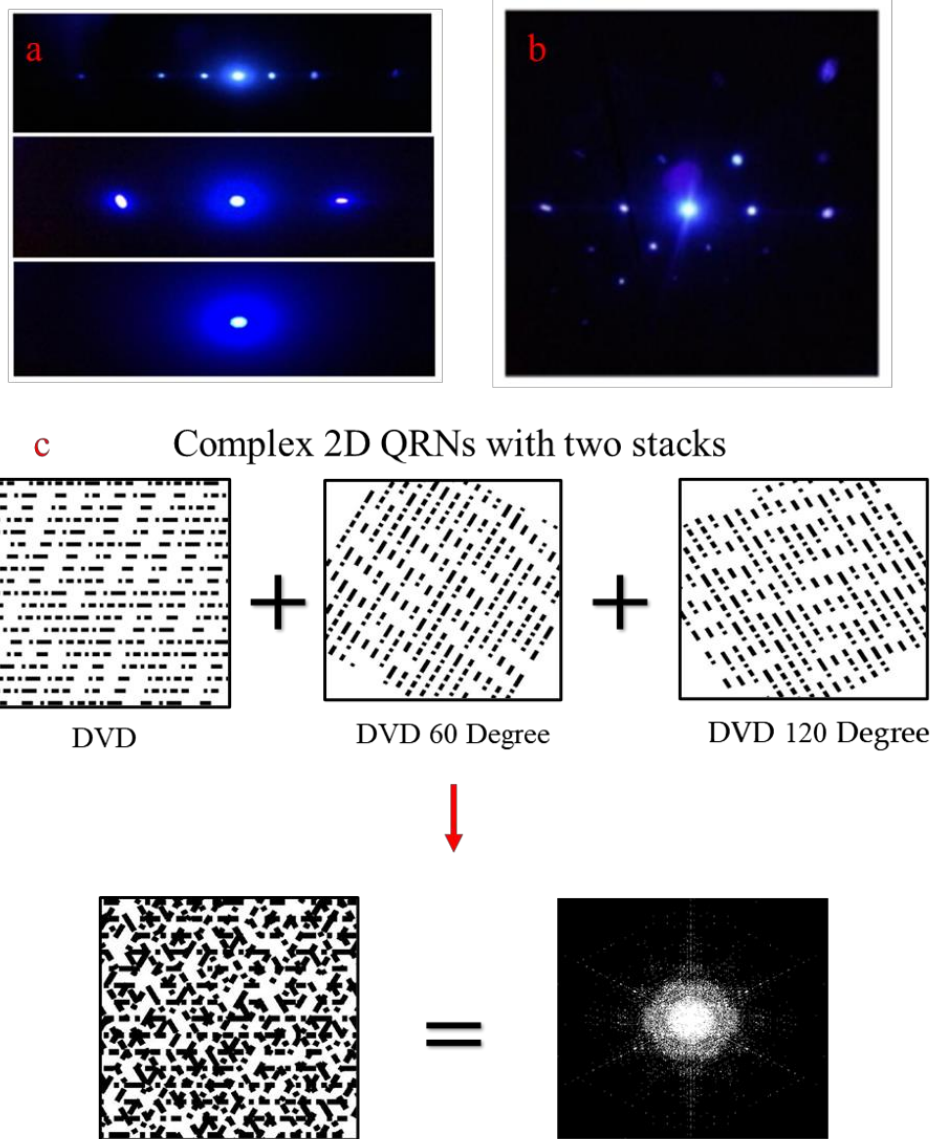


Fig. 7.2-1 (a) – (b) Three different diffraction phenomena; (a) third-order diffraction for CD molds, first-order diffraction for DVD molds, and zero-order for Blu-ray molds, respectively. (c) a schematic illustration for stacking method and its FFA result.

8 REFERENCES

1. Kober, T., Schiffer, H. W., Densing, M. & Panos, E. Global energy perspectives to 2060 – WEC’s World Energy Scenarios 2019. *Energy Strateg. Rev.* **31**, (2020).
2. Brent, A. C. & Pretorius, M. W. an Analysis of the Industrial and Commercial Opportunities To Utilise Concentrated Solar Thermal. **2040**,.
3. BP. BP Statistical Review of World Energy 2014 - 22 August 2014. (2014).
4. Krawicz, A., Cedeno, D. & Moore, G. F. Energetics and efficiency analysis of a cobaloxime-modified semiconductor under simulated air mass 1.5 illumination. *Phys. Chem. Chem. Phys.* **16**, 15818–15824 (2014).
5. Reese, M. O., Marshall, A. R. & Rumbles, G. CHAPTER 1: Reliably Measuring the Performance of Emerging Photovoltaic Solar Cells. in *RSC Nanoscience and Nanotechnology* vols 2018-Janua 1–32 (Royal Society of Chemistry, 2018).
6. Ala-Laurila, P., Pahlberg, J., Koskelainen, A. & Donner, K. On the relation between the photoactivation energy and the absorbance spectrum of visual pigments. *Vision Res.* **44**, 2153–2158 (2004).
7. Becquerel, E. Mémoire sur les effets électriques produits sous l’influence des rayons solaires. *Comptes Rendus* **9**, 561–567 (1839).
8. Chapin, D. M., Fuller, C. S. & Pearson, G. L. A new silicon p-n junction photocell for converting solar radiation into electrical power [3]. *Journal of Applied Physics* vol. 25 676–677 (1954).
9. Heller, A. Conversion of Sunlight into Electrical Power and Photoassisted Electrolysis of

- Water in Photoelectrochemical Cells. *Acc. Chem. Res.* **14**, 154–162 (1981).
10. Guo, S. Y., Sahoo, L., Sosale, G. & Delahoy, A. E. Textured, doped, ZnO thin films produced by a new process for a-Si and CIGS solar cell application. in *Photovoltaic Cell and Module Technologies* vol. 6651 66510B (SPIE, 2007).
 11. Neukom, M., Züfle, S., Jenatsch, S. & Ruhstaller, B. Opto-electronic characterization of third-generation solar cells. *Science and Technology of Advanced Materials* vol. 19 291–316 (2018).
 12. Vigil-Galán, O. *et al.* Route towards low cost-high efficiency second generation solar cells: current status and perspectives. *J. Mater. Sci. Mater. Electron.* **26**, 5562–5573 (2015).
 13. Green, M. A. Third generation photovoltaics: Solar cells for 2020 and beyond. in *Physica E: Low-Dimensional Systems and Nanostructures* vol. 14 65–70 (North-Holland, 2002).
 14. Gangopadhyay, U., Jana, S. & Das, S. State of Art of Solar Photovoltaic Technology. *Conf. Pap. Energy* **2013**, 1–9 (2013).
 15. Ananthachar, V. Current and next generation solar cell market outlook. in *ISES Solar World Congress 2007, ISES 2007* vol. 4 2951–2955 (Springer, Berlin, Heidelberg, 2007).
 16. Edoff, M. Thin film solar cells: Research in an industrial perspective. in *Ambio* vol. 41 112–118 (2012).
 17. Brown, G. F. & Wu, J. Third generation photovoltaics. *Laser Photonics Rev.* **3**, 394–405 (2009).
 18. Weintraub, B., Wei, Y. & Wang, Z. Optical Fiber/Nanowire Hybrid Structures for Efficient Three-Dimensional Dye-Sensitized Solar Cells. *Angew. Chemie* **121**, 9143–9147 (2009).

19. Bett, A. W., Dimroth, F., Stollwerck, G. & Sulima, O. V. III-V compounds for solar cell applications. *Appl. Phys. A Mater. Sci. Process.* **69**, 119–129 (1999).
20. Shockley, W. & Queisser, H. J. Detailed balance limit of efficiency of p-n junction solar cells. *J. Appl. Phys.* **32**, 510–519 (1961).
21. Rühle, S. Tabulated values of the Shockley-Queisser limit for single junction solar cells. *Sol. Energy* **130**, 139–147 (2016).
22. Solanki, C. S. & Beaucarne, G. Advanced solar cell concepts. *Energy Sustain. Dev.* **11**, 17–23 (2007).
23. De Vos, A. & Pauwels, H. On the thermodynamic limit of photovoltaic energy conversion. *Appl. Phys.* **25**, 119–125 (1981).
24. Green, M. A. & Ho-Baillie, A. W. Y. Pushing to the Limit: Radiative Efficiencies of Recent Mainstream and Emerging Solar Cells. *ACS Energy Letters* vol. 4 1639–1644 (2019).
25. McMeekin, D. P. *et al.* Solution-Processed All-Perovskite Multi-junction Solar Cells. *Joule* **3**, 387–401 (2019).
26. Green, M. A. Third generation photovoltaics: Ultra-high conversion efficiency at low cost. *Prog. Photovoltaics Res. Appl.* **9**, 123–135 (2001).
27. Saga, T. Advances in crystalline silicon solar cell technology for industrial mass production. *NPG Asia Materials* vol. 2 96–102 (2010).
28. Raut, H. K., Ganesh, V. A., Nair, A. S. & Ramakrishna, S. Anti-reflective coatings: A critical, in-depth review. *Energy and Environmental Science* vol. 4 3779–3804 (2011).
29. Hummel, R. E. & Guenther, K. H. Handbook of Optical Properties: Thin Films for Optical

- Coatings, Volume 1. 77–81 (1995).
30. Dupuis, J. *et al.* SiO₂/SiNx double antireflection layer for multicrystalline silicon solar cells. *Proc. 24th Eur. PVSEC* 1636–1639 (2009).
 31. Von D. A. G. Bruggeman. Berechnung verschiedener physikalischer Konstanten von heterogenen Medien. 1. *Ann. Phys.* (1935).
 32. Turner, A. F. & Baumeister, P. W. Multilayer Mirrors with High Reflectance Over an Extended Spectral Region. *Appl. Opt.* **5**, 69 (1966).
 33. Macleod, H. A. *Thin-Film Optical Filters*. *Thin-Film Optical Filters* (1986). doi:10.1887/0750306882.
 34. Campbell, P. R. & Green, M. A. On “Intensity Enhancement in Textured Optical Sheets for Solar Cells”. *IEEE Trans. Electron Devices* **33**, 1834–1835 (1986).
 35. Klein-Wiele, J. H. & Simon, P. Fabrication of periodic nanostructures by phase-controlled multiple-beam interference. *Appl. Phys. Lett.* **83**, 4707–4709 (2003).
 36. Haghanifar, S. *et al.* Creating glasswing butterfly-inspired durable antifogging superomniphobic supertransmissive, superclear nanostructured glass through Bayesian learning and optimization. *Mater. Horizons* **6**, 1632–1642 (2019).
 37. Ramanathan, S., Gopinath, S. C. B., Md. Arshad, M. K. & Poopalan, P. Multidimensional (0D-3D) nanostructures for lung cancer biomarker analysis: Comprehensive assessment on current diagnostics. *Biosensors and Bioelectronics* vol. 141 111434 (2019).
 38. Sah, C. T., Noyce, R. N. & Shockley, W. Carrier Generation and Recombination in P-N Junctions and P-N Junction Characteristics. *Proc. IRE* **45**, 1228–1243 (1957).

39. Proctor, C. M., Kuik, M. & Nguyen, T. Q. Charge carrier recombination in organic solar cells. *Progress in Polymer Science* vol. 38 1941–1960 (2013).
40. Saad, M. & Kassis, A. Effect of interface recombination on solar cell parameters. *Sol. Energy Mater. Sol. Cells* **79**, 507–517 (2003).
41. Nwanya, A. C., Ezema, F. I. & Ejikeme, P. M. Dyed sensitized solar cells: A technically and economically alternative concept to p-n junction photovoltaic devices. *International Journal of Physical Sciences* vol. 6 5190–5201 (2011).
42. Kayes, B. M., Atwater, H. A. & Lewis, N. S. Comparison of the device physics principles of planar and radial p-n junction nanorod solar cells. *J. Appl. Phys.* **97**, 114302 (2005).
43. Martí, A., Balenzategui, J. L. & Reyna, R. F. Photon recycling and Shockley's diode equation. *J. Appl. Phys.* **82**, 4067–4075 (1997).
44. Chen, J. & Park, N. G. Causes and Solutions of Recombination in Perovskite Solar Cells. *Advanced Materials* vol. 31 (2019).
45. Kosyachenko, L. & Toyama, T. Current-voltage characteristics and quantum efficiency spectra of efficient thin-film CdS/CdTe solar cells. *Sol. Energy Mater. Sol. Cells* **120**, 512–520 (2014).
46. Qi, B. & Wang, J. Fill factor in organic solar cells. *Phys. Chem. Chem. Phys.* **15**, 8972–8982 (2013).
47. Law, M. *et al.* Determining the internal quantum efficiency of PbSe nanocrystal solar cells with the aid of an optical model. *Nano Lett.* **8**, 3904–3910 (2008).
48. Fresnel Equations. in *Encyclopedia of Optical and Photonic Engineering, Second Edition*

- 1–6 (CRC Press, 2019). doi:10.1081/e-eoe2-120047133.
49. Wolbarsht, M. L. Principles of Optics. Electromagnetic Theory of Propagation, Interference and Diffraction of Light. Max Born , Emil Wolf. *Q. Rev. Biol.* **41**, 440–440 (1966).
 50. Hummel, R. E. & Guenther, K. H. Handbook of Optical Properties: Thin Films for Optical Coatings, Volume 1. 77–81 (1995).
 51. Fink, Y. *et al.* A dielectric omnidirectional reflector. *Science (80-.)*. **282**, 1679–1682 (1998).
 52. Dobrowolski, J. A. & Piotrowski, S. H. C. Refractive index as a variable in the numerical design of optical thin film systems. *Appl. Opt.* **21**, 1502 (1982).
 53. Taflove, A. Review of the formulation and applications of the finite-difference time-domain method for numerical modeling of electromagnetic wave interactions with arbitrary structures. *Wave Motion* **10**, 547–582 (1988).
 54. Moczo, P., Robertsson, J. O. A. & Eisner, L. The Finite-Difference Time-Domain Method for Modeling of Seismic Wave Propagation. *Advances in Geophysics* vol. 48 421–516 (2007).
 55. Lax, M. & Nelson, D. Maxwell’s equations in matrix form. *Phys. Rev. B* **13**, 1777–1976 (1976).
 56. Yee, K. S. Numerical Solution of Initial Boundary Value Problems Involving Maxwell’s Equations in Isotropic Media. *IEEE Trans. Antennas Propag.* **14**, 302–307 (1966).
 57. Gauthier, R. C. Computation of the optical trapping force using an FDTD based technique. *Opt. Express* **13**, 3707 (2005).
 58. Yang, F., Chen, J., Qiang, R. & Elsherbeni, A. FDTD Analysis of Periodic Structures at

- Arbitrary Incidence Angles: A Simple and Efficient Implementation of the Periodic Boundary Conditions. *IEEE Antennas Propag. Soc. AP-S Int. Symp.* 2715–2718 (2006)
doi:10.1109/APS.2006.1711164.
59. Yuan, X. *et al.* Formulation and validation of berenger’s pml absorbing boundary for the fdtd simulation of acoustic scattering. *IEEE Trans. Ultrason. Ferroelectr. Freq. Control* **44**, 816–822 (1997).
60. Duveiller, V., Gevaux, L., Clerc, R., Salomon, J. P. & Hebert, M. Reflectance and transmittance of flowable dental resin composite predicted by the two-flux model: On the importance of analyzing the effective measurement geometry. in *Final Program and Proceedings - IS and T/SID Color Imaging Conference* vols 2020-Novem 313–320 (Society for Imaging Science and Technology, 2020).
61. Chopra, K. L., Paulson, P. D. & Dutta, V. Thin-film solar cells: An overview. *Prog. Photovoltaics Res. Appl.* **12**, 69–92 (2004).
62. Martins, E. R. *et al.* Deterministic quasi-random nanostructures for photon control. *Nat. Commun.* **4**, 1–7 (2013).
63. Wang, C. *et al.* Bio-inspired design strategy of quasi-random structures for optimal light control. *2016 Conf. Lasers Electro-Optics, CLEO 2016* 4–5 (2016)
doi:10.1364/cleo_at.2016.aw1k.5.
64. Hou, J., Hong, W., Li, X., Yang, C. & Chen, S. Biomimetic spiral grating for stable and highly efficient absorption in crystalline silicon thin-film solar cells. *Opt. Express* **25**, A922 (2017).

65. Liu, Y., Shen, H. & Deng, Y. A novel solar cell fabricated with spiral photo-electrode for capturing sunlight 3-dimensionally. *Sci. China, Ser. E Technol. Sci.* **49**, 663–673 (2006).
66. Zhao, Y., Zhu, M., Zhai, S. & Zhao, H. A bioinspired hybrid light-trapping structure and its fabrication for thin-film solar cells. in *2021 IEEE Photonics Conference, IPC 2021 - Proceedings* (Institute of Electrical and Electronics Engineers Inc., 2021). doi:10.1109/IPC48725.2021.9593061.
67. Tahersima, M. H. & Sorger, V. J. Enhanced photon absorption in spiral nanostructured solar cells using layered 2D materials. *Nanotechnology* **26**, (2015).
68. Smith, A. J., Wang, C., Guo, D., Sun, C. & Huang, J. Repurposing Blu-ray movie discs as quasi-random nanoimprinting templates for photon management. *Nat. Commun.* **5**, 5517 (2014).
69. Pala, R. A. *et al.* Optimization of non-periodic plasmonic light-trapping layers for thin-film solar cells. *Nat. Commun.* **4**, 1–7 (2013).
70. MacIá, E. Exploiting aperiodic designs in nanophotonic devices. *Reports Prog. Phys.* **75**, (2012).
71. Weng, S., Li, X., Li, Y. & Yu, H. Z. Optical disc technology-enabled analytical devices: From hardware modification to digitized molecular detection. *Analyst* vol. 141 6190–6201 (2016).
72. Guo, H. jing, Zhang, X. liang & Li, X. chun. Fabrication of ordered micro- and nano-scale patterns based on optical discs and nanoimprint. *Optoelectron. Lett.* **12**, 241–244 (2016).
73. Mamouei, M., Budidha, K., Baishya, N., Qassem, M. & Kyriacou, P. A. An empirical

- investigation of deviations from the Beer–Lambert law in optical estimation of lactate. *Sci. Rep.* **11**, 1–9 (2021).
74. Schuster, C. S. *et al.* Plasmonic and diffractive nanostructures for light trapping—an experimental comparison. *Optica* **2**, 194 (2015).
 75. Van Lare, M. C. & Polman, A. Optimized Scattering Power Spectral Density of Photovoltaic Light-Trapping Patterns. *ACS Photonics* **2**, 822–831 (2015).
 76. Shin, H. F., Hsieh, S. J. & Liao, W. Y. Improvement of the light-trapping effect using a subwavelength-structured optical disk. *Appl. Opt.* **48**, F49–F54 (2009).
 77. Golghasemi Sorkhabi, S. *et al.* Surface quasi periodic and random structures based on nanomotor lithography for light trapping. *J. Appl. Phys.* **122**, (2017).
 78. Li, X. H., Li, P. C., Hu, D. Z., Schaadt, D. M. & Yu, E. T. Light trapping in thin-film solar cells via scattering by nanostructured antireflection coatings. *J. Appl. Phys.* **114**, (2013).
 79. Koo, W. H. *et al.* Light extraction from organic light-emitting diodes enhanced by spontaneously formed buckles. *Nat. Photonics* **4**, 222–226 (2010).
 80. Yu, S. *et al.* Characterization and Design of Functional Quasi-Random Nanostructured Materials Using Spectral Density Function. *J. Mech. Des. Trans. ASME* **139**, (2017).
 81. Kurokawa, Y., Aonuma, O., Tayagaki, T., Takahashi, I. & Usami, N. Effects of surface morphology randomness on optical properties of Si-based photonic nanostructures. *Jpn. J. Appl. Phys.* **56**, 08MA02 (2017).
 82. Fahr, S., Rockstuhl, C. & Lederer, F. Engineering the randomness for enhanced absorption in solar cells. *Appl. Phys. Lett.* **92**, 171114 (2008).

83. Shi, Y., Wang, X. & Yang, F. Disorder Improves Light Absorption in Thin Film Silicon Solar Cells with Hybrid Light Trapping Structure. *Int. J. Opt.* **2016**, (2016).
84. Gómez-Urrea, H. A., Escorcía-García, J., Duque, C. A. & Mora-Ramos, M. E. Analysis of light propagation in quasiregular and hybrid Rudin–Shapiro one-dimensional photonic crystals with superconducting layers. *Photonics Nanostructures - Fundam. Appl.* **27**, 1–10 (2017).
85. Chan, L. & Grimm, U. Substitution-based sequences with absolutely continuous diffraction. in *Journal of Physics: Conference Series* vol. 809 (2017).
86. Matarazzo, V. *et al.* Spectral characterization of two-dimensional Thue-Morse quasicrystals realized with high resolution lithography. *J. Opt.* **13**, 1–8 (2011).
87. Goldstein, S., Kelly, K. A. & Speer, E. R. The fractal structure of rarefied sums of the Thue-Morse sequence. *J. Number Theory* **42**, 1–19 (1992).
88. Bhat, C. R. Simulation estimation of mixed discrete choice models using randomized and scrambled Halton sequences. *Transp. Res. Part B Methodol.* **37**, 837–855 (2003).
89. Estrada, E. Quasirandom geometric networks from low-discrepancy sequences. *Phys. Rev. E* **96**, 1–18 (2017).
90. Dalal, I. L., Stefan, D. & Harwayne-Gidansky, J. Low discrepancy sequences for monte carlo simulations on reconfigurable platforms. *Proc. Int. Conf. Appl. Syst. Archit. Process.* 108–113 (2008) doi:10.1109/ASAP.2008.4580163.
91. Yu, S. *et al.* Characterization and Design of Functional Quasi-Random Nanostructured Materials Using Spectral Density Function. *J. Mech. Des. Trans. ASME* **139**, (2017).

92. Yu, S. *et al.* Design of Non-Deterministic Quasi-random Nanophotonic Structures Using Fourier Space Representations. *Sci. Rep.* **7**, 1–10 (2017).
93. Yu, S., Wang, C., Sun, C. & Chen, W. Topology optimization for light-trapping structure in solar cells. *Struct. Multidiscip. Optim.* **50**, 367–382 (2014).
94. Morokoff, W. J. & Caflisch, R. E. Quasi-Random Sequences and Their Discrepancies. *SIAM J. Sci. Comput.* **15**, 1251–1279 (1994).
95. Iacò, M. R. Low discrepancy sequences: Theory and Applications. (2015).
96. Doerr, C., Gnewuch, M. & Wahlström, M. Calculation of discrepancy measures and applications. in *Lecture Notes in Mathematics* vol. 2107 621–678 (Springer Verlag, 2014).
97. Zhu, B., Xie, L., Yang, T., Wang, Q. & Zheng, Y. A novel radiometric projector compensation algorithm based on Lambertian reflection model. in *MIPPR 2011: Pattern Recognition and Computer Vision* vol. 8004 80040I (SPIE, 2011).
98. Cai, Y., Hua, K. A. & Vu, K. <title>Optimizing patching performance</title>. *Multimed. Comput. Netw.* 1999 **3654**, 204–215 (1998).
99. Andika, A. P., Kaikatui, R. N. & Letsoin, V. Design of power supply circuit used thin-film solar cell for drones. in *IOP Conference Series: Earth and Environmental Science* vol. 343 012224 (IOP Publishing, 2019).
100. Rajendran, P. & Smith, H. Review of Solar and Battery Power System Development for Solar-Powered Electric Unmanned Aerial Vehicles. *Adv. Mater. Res.* **1125**, 641–647 (2015).
101. Kaluthota, S. *et al.* Higher photosynthetic capacity from higher latitude: Foliar characteristics and gas exchange of southern, central and northern populations of *Populus*

- angustifolia. *Tree Physiol.* **35**, 936–948 (2015).
102. Isabel, N., Lamothe, M. & Thompson, S. L. A second-generation diagnostic single nucleotide polymorphism (SNP)-based assay, optimized to distinguish among eight poplar (*Populus L.*) species and their early hybrids. *Tree Genet. Genomes* **9**, 621–626 (2013).
 103. Gates, D. M., Keegan, H. J., Schleter, J. C. & Weidner, V. R. Spectral Properties of Plants. *Appl. Opt.* **4**, 11 (1965).
 104. Prashant, D. V., Agnihotri, S. K. & Samajdar, D. P. Geometric optimization and performance enhancement of PEDOT: PSS/GaAs NP array based heterojunction solar cells. *Opt. Mater. (Amst)*. **117**, 111080 (2021).
 105. Rajput, S. *et al.* Optical modulation via coupling of distributed semiconductor heterojunctions in a Si-ITO-Based Subwavelength Grating. *Phys. Rev. Appl.* **15**, 054029 (2021).
 106. Pandey, S. K. *et al.* Electrically Tunable Plasmonic Absorber Based on Cu-ITO Subwavelength Grating on SOI at Telecom Wavelength. *Plasmonics* **1**, 1–8 (2022).

9 CURRICULUM VITAE

Zhao, Yihong

Email: zyihongapply@gmail.com

Howard R. Hughes College of Engineering

University of Nevada, Las Vegas

4505 S Maryland Pkwy

Las Vegas, NV 89154

EDUCATION

01/2016-Present University of Nevada, Las Vegas Major: Mechanical Engineering

Degree: Doctor of Philosophy GPA: 3.95/4.0

09/2013-05/2015 Boston University, Boston, MA, USA Major: Material Engineering

Degree: Master GPA: 3.23/4.0

09/2009-05/2012 Zhengzhou University, Zhengzhou, Henan, China Major: Material science

Degree: Bachelor GPA: 3.14/ 4.0

Publications

Yihong Zhao, Ming Zhu, Shengjie Zhai, Hui Zhao, "A bioinspired hybrid light-trapping structure and its fabrication for thin-film solar cells." 2021 IEEE Photonics Conference (IPC). IEEE, 2021.

Shengjie Zhai, **Yihong Zhao**, Hui Zhao, "High-Efficiency Omnidirectional Broadband Light-Management Coating Using the Hierarchical Ordered–Disordered Nanostructures with Ultra-Mechanochemical Resistance." ACS applied materials & interfaces 11.13 (2019): 12978-12985.

Corey Malinowski, Fengjie He, **Yihong Zhao**, Ivan Chang, David W. Hatchett, Shengjie Zhai, Hui Zhao, Nanopatterned silk fibroin films with high transparency and high haze for optical applications." RSC advances 9.70 (2019): 40792-40799.

Yinxiao Li, Mohammad Amin Alibakhshi, **Yihong Zhao**, Chuanhua Duan, Exploring Ultimate Water Capillary Evaporation in Nanoscale Conduits." Nano letters 17 8 (2017): 4813-4819

Yihong Zhao, Huijing Lin, Jimin Pan, Failure Analysis on Disintegration of Cylinder Liner in Given Diesel, Hot Working Technology (core journal), 2012(41-21), ISSN 1001-3814, CN61-1133/TG

Yihong Zhao, Study on Spot Welding of Magnesium Alloy, Science Times, 2012(04), ISSN 1005-250X, CN46-1039/G3

Jieqiong Guo, **Yihong Zhao**, Erxing Li, Fire Spray Remanufacturing Method for Mine Equipment Wear-resistant Parts, Science Times, ISSN 1005-250X, CN46-1039/G32011(24)

Yaxian Du, **Yihong Zhao**, Shanshan Wu, Liangying Zhang, Effect of Salt Spray Corrosion on Microstructure and Properties of New Solders used in Copper-Aluminum Braze Welding, Science Times, 2012(01), CN46-1039/G3, ISSN 1005-250X

Conference

Yihong Zhao, et al. "Towards High-Efficient Broadband Omnidirectional Light Trapping: Deterministic Quasi-Random Nanostructures Design, Optimization, and Scalable Fabrication." Nanoengineering: Fabrication, Properties, Optics, Thin Films, and Devices XVIII. Vol. 11802. SPIE, 2021.

Yihong Zhao, et al. "A bioinspired hybrid light-trapping structure and its fabrication for thin-film solar cells." 2021 IEEE Photonics Conference (IPC). IEEE, 2021.

Yihong Zhao, et al. "Programmable quasi-random nanostructured coating with omnidirectional broadband improvement for photon management (Conference Presentation)." Photonic and Phononic Properties of Engineered Nanostructures X. Vol. 11289. SPIE, 2020.

Professional Memberships

01/2021 **Membership**, Society of Photo-Optical Instrumentation Engineers

01/2017-01/2019 **Mechanical Engineering Representative**, Graduate and Professional Student Association, UNLV

01/2018-12/2018 **Representative**, Differential committee of Engineering Department, UNLV

12/2016 **Membership**, Material Research Society Conference, Boston

Awards

01/2021 Renewable Energy Fellowship (concentration polarization)